INTERFACIAL ELECTROCHEMISTRY AND SURFACE CHARACTERIZATION: HYDROGEN TERMINATED SILICON, ELECTROLESSLY DEPOSITED PALLADIUM & PLATINUM ON PYROLYZED PHOTORESIST FILMS AND ELECTRODEPOSITED COPPER ON IRIDIUM

Raymond Chan, B.S., B.A.

Dissertation Prepared for the Degree of

DOCTOR OF PHILOSOPHY

UNIVERSITY OF NORTH TEXAS

December 2003

APPROVED:

Oliver M.R. Chyan, Major Professor
William E. Acree, Jr., Committee Member
Paul Marshall, Committee Member
Michael G. Richmond, Committee Member
Ruthanne Thomas, Chair of the Department of Chemistry
Sandra L. Terrell, Interim Dean of the Robert B. Toulouse School of Graduate Studies

Chan, Raymond. *Interfacial Electrochemistry and Surface Characterization: Hydrogen Terminated Silicon, Electrolessly Deposited Palladium & Platinum on Pyrolyzed Photoresist Films and Electrodeposited Copper on Iridium*. Doctor of Philosophy (Analytical Chemistry), December 2003, 160 pp., 6 tables, 70 figures, references, 100 titles.

Hydrogen terminated silicon surfaces play an important role in the integrated circuit (IC) industry. Ultra-pure water is extensively used for the cleaning and surface preparation of silicon surfaces. This work studies the effects of ultra-pure water on hydrogen passivated silicon surfaces in a short time frame of 120 minutes using fourier transform infrared spectroscopy – attenuated total reflection techniques. Varying conditions of ultra-pure water are used. This includes dissolved oxygen poor media after nitrogen bubbling and equilibration under nitrogen atmosphere, as well as metal contaminated solutions. Both microscopically rough and ideal monohydride terminated surfaces are examined.

Hydrogen terminated silicon is also used as the sensing electrode for a potentiometric sensor for ultra-trace amounts of metal contaminants. Previous studies show the use of this potentiometric electrode sensor in hydrofluoric acid solution. This work is able to shows sensor function in ultra-pure water media without the need for further addition of hydrofluoric acid. This is considered a boon for the sensor due to the hazardous nature of hydrofluoric acid.

Thin carbon films can be formed by spin coating photoresist onto silicon substrates and pyrolyzing at 1000 ^{o}C under reducing conditions. This work also shows that the electroless deposition of palladium and platinum may be accomplished in hydrofluoric acid solutions to attain palladium and platinum nanoparticles on a this film carbon surface for use as an electrode. Catalysis of these substrates is studied using hydrogen evolution in acidic media, cyclic voltammetry, and catalysis of formaldehyde. X-ray diffractometry (XRD) is used to ensure that there is little strain on palladium and platinum particles.

Iridium is thought to be a prime candidate for investigation as a new generation copper diffusion barrier for the IC industry. Copper electrodeposition on iridium is studied to address the potential of iridium as a copper diffusion barrier. Copper electrodeposition is studied using a current-transient technique to obtain insight into the nucleation and growth mechanism. Copper on iridum was annealed up to 600 ^{o}C. X-ray photoelectron spectroscopy and XRD confirm that electrodeposited copper exists in a metallic state. XRD shows that copper exists in the characteristic face-centered cubic (111) form. XRD also confirms the stability of the copper-iridium interface with no new peaks after annealing, which is indicative that no interaction occurs. Scanning electron microscopy, and Scotch ® Tape peel tests confirm the uniformity and strength of copper on iridium even after annealing to 600 ^{o}C.

ACKNOWLEDGEMENTS

I would like to acknowledge and articulate my appreciation to those who have encouraged and supported me to complete this endeavor.

I greatly appreciate the efforts of my research advisor, Dr. Oliver M.R. Chyan, whose sincerity, support, objective critiques, steady encouragement, intelligence and immeasurable patience are an example which I hope to emulate in my professional and personal life.

I am grateful for the comments and discussions from Dr. Michael G. Richmond, Dr. William E. Acree, and Dr. Paul Marshall, my PhD committee members, which have helped me keep on track at times. Thanks to Dr. Theresa Golden for discussions and insight as well as permission to use the Siemens D-500 X-Ray Diffractometer. Thanks to Dr. Robert Wallace and Dr. Bruce Gnade for their time and patience as well as unfettered access to the Laboratory for Electronic Materials and Devices. Thanks also to Dr. David Golden for XPS analyses. Funding and financial support from the Welch Foundation, UNT Faculty Research Fund, Kodak, Texas Instruments and the Texas Advanced Technology program is deeply appreciated.

Special thanks to the various undergraduate, graduate, post-doctoral scientists and support staff who have had the patience and willingness to help me in my various enterprises. Thanks to Dr. Qi Wang for teaching and helping me with XRD. Thanks to Dr. Edward Sosa for his help with XPS analysis as well as Dr. Swarnagowri Addepalli and Prasana Mani for their guidance and training on XPS. Many thanks to Dr. Thomas Ponnuswamy for his help and suggestions. Thanks to Vivian Liang for her help in

studying pyrolyzed photoresist films. Special thanks to my comrade in-arms, Dr. Tiruchirapalli Arunagiri who is always willing to lend a hand, idea or an ear! Thanks to the past and present group members John Sarik, Chris Cheng, Joe Chen, Yibin Zhang, Praveen Reddy, Huang Long, Sarah Flores and Oscar Ojeda who have made this research group a pleasure to work with.

I would like to express my gratitude to my family for their enthusiasm and confidence in my education. I would like to specially thank my wife and son, Janet and Ethan, for their unwavering support, encouragement and love.

Lastly I would like to remember the memory of my father-in-law Joseph Henry Nunn and my teacher Larry Dale Shelburne who both passed away during the final stage of this work. Thanks to Joseph Henry Nunn whose intelligence, quiet resiliency and quick wit will be sorely missed. Thanks to Larry Dale Shelburne whose friendship as well love and expertise in German language and literature has set me on a path of discovery which is continuing today.

TABLE OF CONTENTS

ACKNOWLEDGEMENTS...iii

TABLE OF CONTENTS v

LIST OF FIGURES viii

LIST OF TABLES xiii

CHAPTER 1 INTRODUCTION..1

1.1 The Integrated Circuit 2
  1.1.1 The MOSFET 2
1.2 Silicon.. 4
  1.2.1 Single Crystal Si 4
  1.2.2 Semiconductor properties 6
  1.2.3 Preparatory Cleaning of Si 11
1.3 Pyrolyzed Photoresist Films... 13
  1.3.1 Carbon Films by Pyrolysis 13
1.4 Interconnect Materials... 15
  1.4.1 Cu Interconnects 15
  1.4.2 Silver as Another Possibility 16
1.5 The Importance of Iridium and Ruthenium as Diffusion Barriers for Interconnects 17
1.5.1 Ir: Uses and Possibilities 17
  1.5.2 Ruthenium: Possibilities... 19
1.6 Electrochemical Techniques 19
  1.6.1 The Dynamic Heterogeneous Nature of Electrochemistry.............................. 20
  1.6.2 Current: Working vs. Counter Electrodes... 21
    1.6.3 Potential: Working vs. Reference Electrode.. 22
  1.6.4 Open Circuit Potential.. 23
  1.6.5 Cyclic Voltammetry 24
  1.6.6 Chronoamperometry 24
1.7 FTIR – ATR TECHNIQUE... 25
  1.7.1 Fourier Transform Infrared Spectroscopy 25
  1.7.2 Attenuated Total Reflection 28
1.8 X-Ray Diffraction.. 30
1.9 Scanning Electron Microscopy and Energy Dispersive X-ray Spectroscopy 34
  1.9.1 SEM/EDX Fundamental Workings 34
  1.9.2 Energy Dispersive X-ray Spectroscopy 35
1.10 X-ray Photoelectron Spectroscopy 36
  1.10.1 XPS fundamentals.. 36
1.11 References 39

CHAPTER 2 DYNAMIC CHANGES OF PASSIVATED SI (111) SURFACES IN ULTRA-PURE WATER UNDER DIFFERENT CONDITIONS STUDIED WITH ATR/FTIR........................ 44

2.1 Introduction 44
2.2 Experimental 45
2.2.1 Silicon ATR Preparation 45
2.2.2 Cleaning Preparation 46
2.2.3 Instrumentation 47
2.3 Results and Discussion: 48
2.3.1 FTIR Spectrum of Hydrogen Terminated Si(111) 48
2.3.2 Si(111) in O_2 Poor UPW 53
2.3.3 The Effects of N_2 Bubbling on Si(111) in UPW 57
2.3.4 Ideal Monohydride Terminated Si(111) in UPW 59
2.3.5 Trace Metal Contaminated UPW 64
2.3.6 Possible mechanism for the Oxidation of Si(111) 68
2.4 Conclusion 70
2.5 References 72

CHAPTER 3 INVESTIGATION OF SI BASED POTENTIOMETRIC SENSORS IN ULTRA-PURE WATER WITH TRACE METALLIC CONTAMINANTS 74

3.1 Introduction 74
3.2 Experimental 76
3.3 Results and Discussions.. 78
3.4 Conclusion 85
3.5 References 86

CHAPTER 4 ELECTROLESSLY DEPOSITED PLATINUM AND PALLADIUM NANOPARTICS ON PYROLYZED PHOTORESIST FILMS.. 87

4.1 Introduction 87
4.2 Experimental 91
4.3 Results and Discussions.. 95
4.4 References 116

CHAPTER 5 INVESTIGATION INTO THE VIABILITY OF Ir AS A COPPER DIFFUSION BARRIER FOR Cu INTERCONNECTS 120

5.1 Introduction 120
5.2 Experimental 121
5. 3 Results and Discussion 125
5.4 Conclusion 138
5.5 REFERENCES 140

CHAPTER 6 CONCLUSION 142

6.1 Conclusions from Chapters 142
6.1.1 Si(111) FTIR-ATR studies 142
6.1.2 Si Based Potentiometric Sensor in UPW 143
6.1.3 Electroless Pd and Pt on PPF..143
6.1.4 Ir as a Cu Diffusion Barrier 143
6.2 Continuing Endeavors 144
6.2.1 Ru/RuOx..144
6.2.2 Direct Cu electroplating on Ru 149
6.3 Conclusion 150
6.4 References..151

COMPLETE REFERENCE LIST..152

LIST OF FIGURES

Figure 1.1 n-channel MOSFET device……………………………………………………………3

Figure 1.2 (A) fcc lattice (B) interpenetrating fcc lattices……………………………………5

Figure 1.3 Miller indices for (A) the (100) plane and (B) the (111) plane…………………6

Figure 1.4 Energy bands for (A) Metals, (B) Semiconductors & (C) Insulators…………7

Figure 1.5 Charge conduction of a Semiconductor…………………………………………9

Figure 1.6 Doped Semiconductors (A) n-type (B) p-type……………………………………10

Figure 1.7 Cross sectional view of a 0.13 μm MOSFET and Cu interconnects……………16

Figure 1.8 Zones of an Electrochemical System………………………………………………20

Figure 1.9 Three Electrode System……………………………………………………………23

Figure 1.10 FITR & Michelson Interferometer…………………………………………………26

Figure 1.11 Propgation of IR radiation through an ATR element……………………………29

Figure 1.12 X-ray diffraction in a crystalline solid………………………………………………32

Figure 1.13 Schematic of SEM……………………………………………………………………35

Figure 1.14 XPS electron ejection…………………………………………………………………37

Figure 2.1 FTIR-ATR spectra of HF etched N-type Si (111)……………………………………49

Figure 2.2 FTIR-ATR spectra of HF etched N-type Si (111) with immersion time in UPW , Hydride Region……………………………………………………………………………50

Figure 2.3 Normalized Integrated Absorbances of hydride regions of H-terminated Si (111) immersed in UPW……………………………………………………………………51

Figure 2.4 FTIR-ATR spectra of HF etched N-type Si (111) with immersion time UPW, Oxide Region……………………………………………………………………………………52

Figure 2.5 Silicon Crystal Structure………………………………………………………………53

Figure 2.6 FTIR-ATR spectra of HF etched N-type Si (111) with immersion time in O_2 poor UPW, Hydride Region……………………………………………………………………………..55

Figure 2.7 Normalized Integrated Absorbances of hydride regions of H-terminated Si (111) immersed in O_2 poor UPW………………………………………………………………………55

Figure 2.8 FTIR-ATR spectra of HF etched N-type Si (111) with immersion time O_2 poor UPW, Oxide Region……………………………………………………………………………………56

Figure 2.9 FTIR-ATR spectra of HF etched N-type Si (111) with immersion time in N_2 bubbled UPW, Hydride Region…………………………………………………………………………57

Figure 2.10 Normalized Integrated Absorbances of hydride regions of H-terminated Si (111) immersed in N_2 bubbled UPW……………………………………………………………………58

Figure 2.11 FTIR-ATR spectra of HF etched N-type Si (111) with immersion time N_2 bubbled UPW, Oxide Region……………………………………………………………………………59

Figure 2.12 FTIR-ATR spectra of Monohydride Si(111) under various UPW conditions ……………………………………………………………………………60

Figure 2.13 NIA of Monohydride Terminated N-Si(111) surfaces in UPW………………..61

Figure 2.14 Rough vs. Smooth Si(111) hydrogen termination……………………………..62

FIGURE 2.15 S and P polarized FTIR-ATR spectra from Si(111) monohydride terminated ……………………………………………………………………………..63

Figure 2.16 FTIR-ATR spectra of Hydrogen Terminated N-type Silicon (111) trace metal in contaminated UPW……………………………………………………………………………..64

Figure 2.17 Normalized Integrated Absorbances of hydride regions of H-terminated Si (111) in trace metal contaminated…………………………………………………………………65

Figure 2.18 FTIR-ATR spectra of HF etched N-type Si (111) with immersion time in trace metal contaminated UPW, Oxide Region……………………………………………………66

Figure 2.19 FTIR-ATR spectra of HF etched N-type Si (111) with immersion time in trace metal contaminated UPW-DO POOR conditions……………………………………………67

Figure 2.20 NIA of FTIR-ATR hydride regions from HF etched N-type Si (111) with immersion time in trace metal contaminated UPW-DO POOR………………………………..68

Figure 2.21 Possible mechanism for the oxidation Si surfaces in H_2O………………………..69

Figure 3.1 Illustration of (A) Custom made PFA electrode body (B) Modified alligator clip assembly……………………………………………………………………………………………………77

Figure 3.2 Time dependent potentiometric response of (111) N-type Si based sensor in ultra-pure H_2O and Ag^+ (setup in inset)……………………………………………………………79

Figure 3.3 Linear Calibration Curve – Ag^+ contamination………………………………………80

Figure 3.4 Time dependent potentiometric response of (111) N-type Si based sensor in ultra-pure H_2O with Cu^{2+}……………………………………………………………………………82

Figure 3.5 Spontaneous deposition of metals on Si surface…………………………………83

Figure 3.6 Illustration of the metal deposition and induced oxidation………………………84

Figure 4.1 General Illustration of Photoresist use for (A) negative photoresist and (B) positive photoresist…………………………………………………………………………………89

Figure 4.2 (A) Experimental Apparatus needed for spontaneous metal deposition on HOPG and (B) SEM image……………………………………………………………………………96

Figure 4.3 SEM photograph of PPF breakdown in 4.9% HF for 30 minutes………………97

Figure 4.4 SEM photograph of (A) 100 ppm Pt^{2+} and (B) 500 ppm Pt^{2+} deposited on PPF/Si substrates in 0.049% HF after 1 and 3 hour deposition times………………………99

Figure 4.5 SEM photograph of (A) 100 ppm Pd^{2+} and
(B) 500 ppm Pd^{2+} deposited on PPF/Si substrates in 0.049% HF after 1 and 3 hour deposition times……………………………………………………………………………………100

Figure 4.6 CV of (A) 100 ppm Pt^{2+} and (B) 500 ppm Pt^{2+} in 0.1 M H_2SO_4………………101

Figure 4.7 CV of (A) 100 ppm Pd^{2+} and (B) 500 ppm Pd^{2+} in 0.1 M H_2SO_4………………102

Figure 4.8 SEM of 0.49% HF deposited (A) 1000 ppm Pt 30 minutes and (B) 1000 ppm Pd 10 minutes………………………………………………………………………………………104

Figure 4.9 XRD of Pd and Pt deposited on PPF substrates…………………………………105

Figure 4.10 Representative CV's of Normal, Pd, and Pt deposited PPF substrates in $Ru(NH_3)_6$ redox couple solutions…………………………………………………………108

Figure 4.11 Representative CV's of Normal, Pd, and Pt deposited PPF substrates in Dopamine redox couple solutions.……………………………………………………………………110

Figure 4.12 Cyclic Voltammograms of PPF substrates before and after HF exposure ……………………………………………………………………111

Figure 4.13 CV's of(A) Pd and (B) Pt disk in 0.1M HCHO and 1M $HClO_4$………………112

Figure 4.14 CV of (A) Pt/PPF substrate and (B) Pd/PPF substrate in 0.1M HCHO and 1M $HClO_4$ ……………………………………………………………………………………114

Figure 5.1 Preparation of Ir shot electrodes where (I)the plastic mold has hole drilled, (II) shot and wire are set in epoxy and covered, and (III) the whole electrode is polished so that Ir has a mirror finish……………………………………………………………122

Figure 5.2 CV of Ir shot in 50 mM $CuSO_4$ and 0.1 M H_2SO_4 ……………………………126

Figure 5.3 OCP vs. ML coverage……………………………………………………………127

Figure 5.4 XPS of Ir shot electrode with electrodeposited Cu (-400 mV for 10 seconds.) ……………………………………………………………………128

Figure 5.5 SEM photographs of 20 second Cu deposition on Ir shot (A) not annealed and (B) annealed at 600°C ……………………………………………………………129

Figure 5.6 SEM photographs of 22 second Cu deposition on Ir shot (A) not annealed and (B) annealed at 600°C ……………………………………………………………129

Figure 5.7 SEM photographs of 30 second Cu deposition on Ir shot (A) not annealed and (B) annealed at 600°C ……………………………………………………………130

Figure 5.8 XRD data of Electrodeposited Cu on Ir shots……………………………………132

Figure 5.9 Current vs time transients…………………………………………………………133

Figure 5.10 Cu nucleation on Ir shot compared to idealized Instaneous and Progressive modes……………………………………………………………………………………135

Figure 5.11 Comparison of Nucleation Number Density of Cu electrodeposition on Ir vs Ru……………………………………………………………………………………………137

Figure 6.1 XPS survey scan of a Ru sputtered Si substrate…………………………………145

Figure 6.2 XPS regional scans of Ru3d regions………………………………………………147

Figure 6.3 XPS regional scans of O1s regions…………………………………………………….148

Figure 6.4 Optical microscopy photograph of Cu on Ru/Si substrate scribed with diamond tipped scriber - before and after tape peel test for adhesion………………….150

LIST OF TABLES

Table 1.1 Common RCA surface preparation solutions……………………………………………11

Table 1.2 Common Internal Reflection Elements…………………………………………………28

Table 1.3 X-ray Wavelengths Target Elements……………………………………………………..31

Table 2.1 Summary of Results…………………………………………………………………………..71

Table 4.1 Calculated values for stress and strain of Pd and Pt particles on PPF……….107

Table 6.1 Binding Energy Peak Positions for Regional Scans…………………………………..146

CHAPTER 1

INTRODUCTION

This introductory chapter will serve the purpose to provide the reader with a broad foundation of understanding for experimental techniques and procedures while also providing a general look at the research undertaken. The dissertation may be broadly divided into four main interests covering: silicon (Si) interfacial surface chemistry in ultraclean media, Si interfacial chemistry in contaminated media, characterization of carbon thin films on Si, and some characterization of metal/metal oxide for use on Si. The fundamental substrate which binds these subjects together is the use of the Si substrate as the foundation from which research is conducted.

Integrated circuits (ICs) form the basis of all commercial electronics used today. Today's ICs are nearly all based on Si substrates. An IC is basically a combination of transistors, diodes, capacitors and resistors. These discrete devices are connected together to form a functional tool for electronic devices. Creation of the first IC by Jack Kilby in 1959 set into motion a series of events that lead us to the state of electronic miniaturization which we see today. Improvements to fabrication practices, increase device density and reliability are constantly being sought. Si has become the workhorse of the IC industry by virtue of predictable electronic properties and more importantly its ability to form a stable surface oxide. The formation of a stable surface oxide is a key structure to the development of microelectronic devices allowing for the surface termination of bare Si.

1.1 The Integrated Circuit

1.1.1 The MOSFET

The advent of the IC has produced unprecedented technological and economic growth which has never before been seen in other industries. The IC chip is the heart of the computer industry. For the consumer, every generation of software that is produced must have hardware which is capable of maintaining proper operating conditions (i.e. computing speed, reliability, ease of use) such that the end product fulfills its function. Excellent examples may be seen in the day to day use of such technologies as the microcomputer, cellular phone, and the Internet. For every new generation of such products and services, a new bar must be set and the demand for higher speed and computing power by the consumer has led to the exponential growth for new avenues and techniques by which stronger, faster and more efficient IC chips can be manufactured. The basic IC chip is based on the **m**etal **o**xide **s**emiconductor **f**ield **e**ffect transistor or MOSFET device[1,2].

The MOSFET is the prevailing device in today's microprocessors and memory circuits. There are two type of **c**omplementary **m**etal **o**xide **s**emiconductor (CMOS) devices. The type of substrate used to produce the CMOS determines what type of CMOS transistor is made: the n-type or p-type. Figure 1.1 illustrates a n-type MOS. The n-MOS has three regions of interest: the Drain (D), the Gate (G) and the Source (S). S and D regions are made either electron rich (n+) or hole rich (p+) through ion-implantation or diffusion. This n-MOS base substrate is p-type Si with electron rich regions at the source and drain. The MOSFET may be thought of as an on/off switch whereby electron flow between the source and drain occurs at the region called the n-channel. A thin gate dielectric covers the n-channel. This gate dielectric is then covered with a gate, which can consist of some heavily doped poly Si.

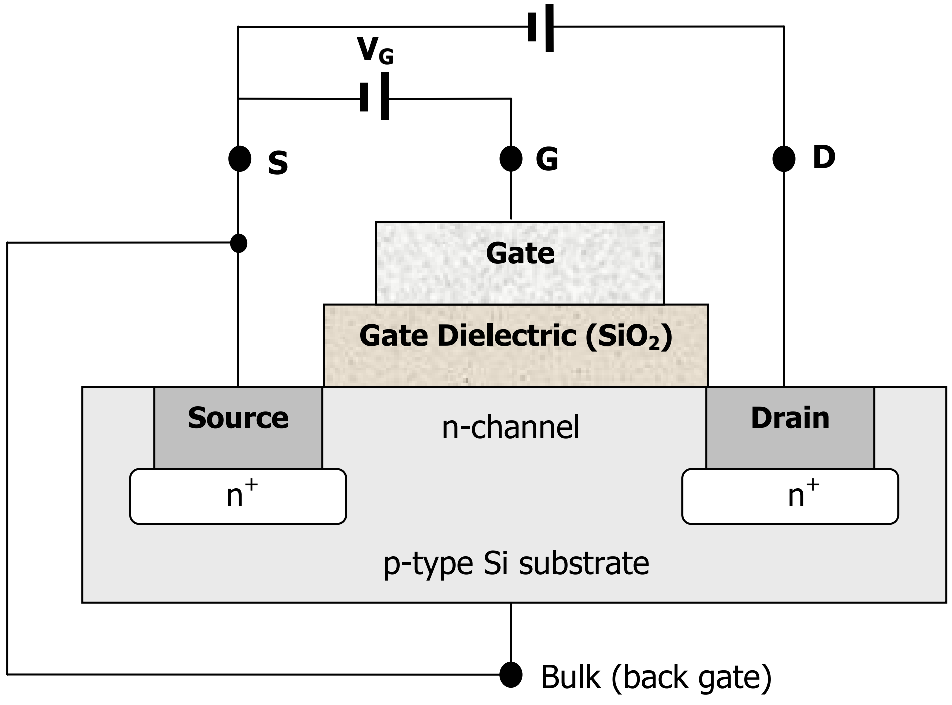

Figure 1.1 n-channel MOSFET device

A phenomenon called inversion occurs when voltages beyond a threshold voltage are applied to the gate. In inversion, there exists a negatively charged inversion layer at the oxide-semiconductor interface in addition to the depletion-layer. The inversion layer is due to minority carriers (in this case electrons,) which are attracted to the interface by the positive gate voltage. Therefore, as V_G is increased, an n-channel forms which connects the S and D points which are otherwise electrically isolated. This allows for current flow between S and D turning the switch 'on.' The amount of voltage (V_G) at G acts as the switch for current flow. Thus when there is not an appropriate V_G greater than the threshold voltage, there is no current flow and the switch is 'off.'

One of the major objectives in the IC industry is to be able to increase device density on the underlying Si substrate. This is because MOSFETs work in parallel and more MOSFETs working in parallel lead to a faster end device. For such an increase in device density to occur, the MOSFET device must necessarily shrink. The process of ever decreasing device size or *miniaturization* of the gate oxide has been accomplished from the 0.18 µm technology node to 0.13 µm technology node while research is already being conducted to push current technology into the 0.09 µm size and beyond.

1.2 Silicon

1.2.1 Single Crystal Si

Since the systems studied in this dissertation all have a foundation on Si (Si) as the main substrate, it is useful to discuss the basic characteristics of Si. Located on the fourth main group column of the periodic table, Si has four valence electrons which can covalently bond with neighboring Si atoms to form the stable Si tetrahedral structure. This diamond structure has an fcc Bravais lattice with each Si atom being sp^3 hybridized. The diamond like lattice can be described as two interpenetrating displaced ($a_0/4$, $a_0/4$, $a_0/4$; where a_0 is the lattice constant) lattices[3,4]. Figure 1.2 illustrates a face-centered cube (A) and two interpenetrating face-centered cubes (B.)[2] When viewed in certain directions, the atoms and bonds appear to lie in sheets. In order to describe the sheet positions and bond directions, the convention of Miller indices are used. Miller indices are the vector representation for the orientation of the atomic plane for a given crystal lattice. By definition, the Miller index of a given plane is given by the smallest set of integers for the reciprocal of the intercepts of the atomic plane to a three-dimensional *x*, *y* and *z* axes at corresponding distances of the unit vectors *a*, *b*, and *c*. Miller indices are commonly designated as (*hkl*). This notion of using the reciprocals of the atomic plane intercepts allows one to bypass the problem where any of the axes are not intersected. Figure 1.3 illustrates two common planes of Si.

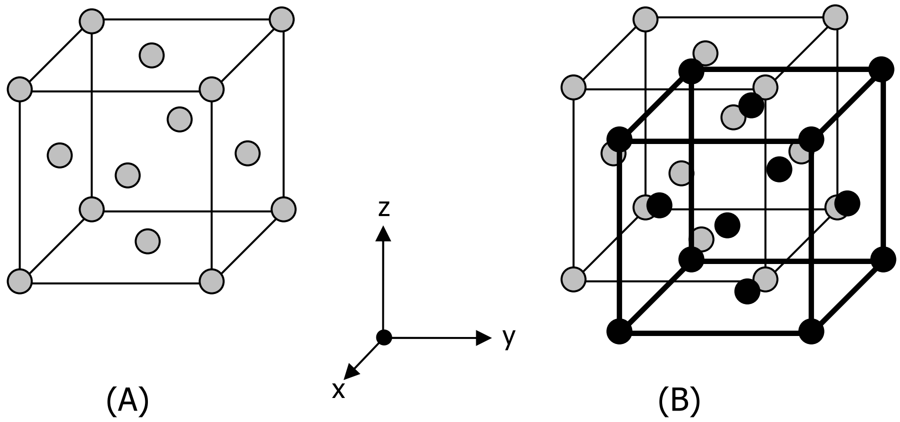

FIGURE 1.2 (A) fcc lattice (B) interpenetrating fcc lattices

Consider the (100) plane on Figure 1.3 (A). By starting at the origin following the X-axis to a certain distance *a* we see that the (100) plane has an X-intercept at that point, whereas the (100) plane has a Z and Y intercept of ∞. Therefore the Miller index for the (100) plane is derived from (hkl) where (1/1 1/∞ 1/∞) leads to the corresponding notation (100). The same treatment can be applied to when considering the (111) plane of Figure 1.3 (B) where the reciprocal of the intercepts at the vector unit distances of a,b and c of the atomic plane will lead to a Miller index of (111).

During the wafer production process, single crystal Si ingots may be sliced through a specific plane. This generates a single crystal Si wafer where the surface will have that specific plane exposed. This is important since different planes will exhibit different physical, chemical and electrical properties due to differing binding energies and atom stacking of Si. Si (100) is the most commonly used Si substrate in the IC industry[2].

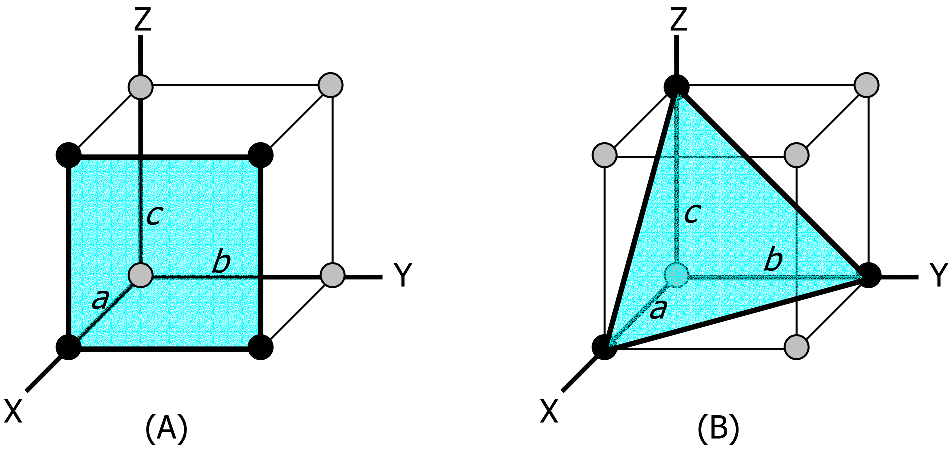

(A) (B)

Figure 1.3 Miller indices for (A) the (100) plane and (B) the (111) plane

1.2.2 Semiconductor properties

The materials studied in this dissertation fall into one of the categories of metals (conductors,) semiconductors and insulators. These classes of materials play a vital role in the IC industry[2]. The study and manipulation of their properties is paramount to the continued growth of the industry as a whole. Metals are good conductors and contain a high density of charge carriers. Insulators are the opposite containing nearly zero density of charge carriers. Semiconductors maintain a technologically important position containing charge carrier densities in the intermediate range between good conductors and good insulators[5]. Illustrated in Figure 1.4 are the simplified band structures for conductors, semiconductors and insulators.

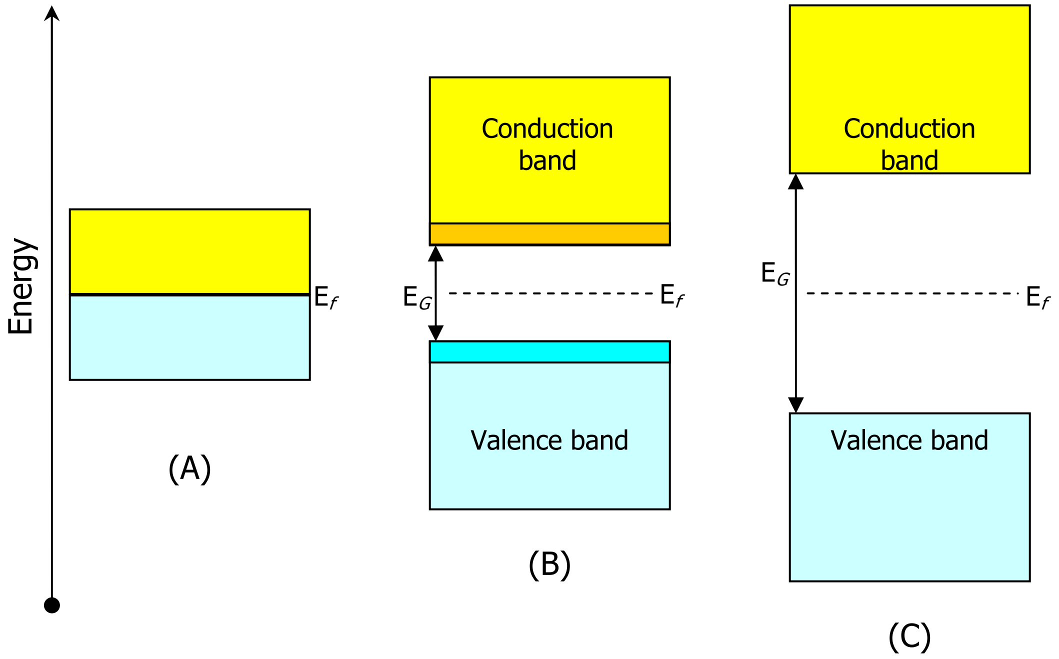

Figure 1.4 Energy bands for (A) Metals, (B) Semiconductors & (C) Insulators

When two of the same atoms are far apart, they do not interact and their electronic energy levels are considered two be separate non-interacting entities. As the atoms are brought together, the electronic wave functions begin to overlap, and if their interaction is strong, two electronic energy levels will form. Now if there is a multitude of levels brought closely together, as in a crystalline solid, the energy levels are so closely spaced that they may be regarded as one energy band. The Fermi level (E_F) is that level at which the probability to find an electron at that energy is approximately 50% based on the Fermi-Dirac distribution function. The Fermi-Dirac distribution function describes the probability of finding an electron in a particular energy state (E):

$$f(E) = \frac{1}{e^{(E-E_0)/kt} + 1}$$

where at $E=E_f$ the function $f(E)$ has a value of ½.

In considering metals or conductors, it is easiest to consider a simplified half filled metal band structure as shown in Figure 1.4 (A). If there is a transfer of energy into the metal, very little energy transfer is required for electrons to move from occupied to unoccupied energy states.

Looking at the two highest energy bands of insulators in Figure 1.4 (C), there is a separation between the most filled (valence) and empty (conduction) bands. This gap is called referred to as the energy gap or band gap (E_G). Insulators are considered to have large energy gaps (circa > 4-5 eV). The Fermi-Dirac distribution function therefore predicts that there will be very few electrons to be excited into the upper band at normal temperatures. Since few electrons will occupy the conduction band, the overall contribution to electrical conductivity will be very small, thus leading to high resistivity. A material with high resistivity is the most recognized characteristic of an insulator.

In between the two classes of materials are materials with a bandgap on the order of ~1.0 eV. Since E_G is relatively small, it is more feasible for an significant number of electrons to be excited from the valence band to the conduction band. A small applied potential can raise the electrons into the conduction band, easily resulting in a moderate current. A pure semiconductor with no added processing is termed an intrinsic semiconductor.

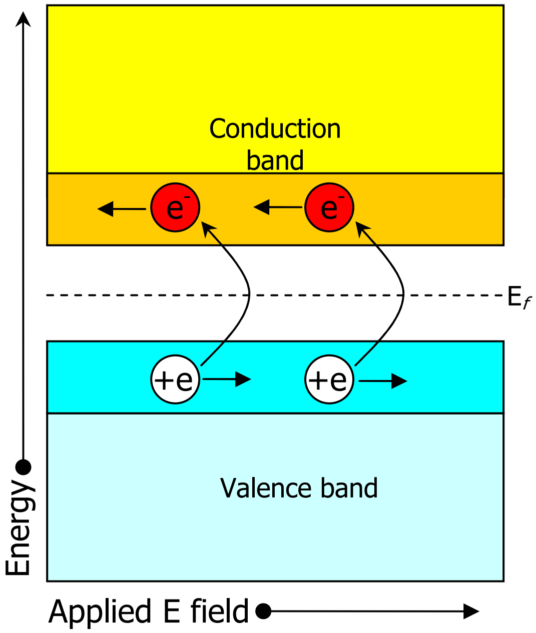

Figure 1.5 Charge conduction of a Semiconductor

Semiconductors contain both negative and positive charge carriers. When an electron moves from the valence band into the conduction band, a vacant crystal site or hole results from the movement. This hole is an electron deficient site and is analogous to a positive charge known with the designation of +e. The hole can migrate through the semiconductor by virtue that as a nearby valence electron transfers to the hole, another hole is left behind in the electron's place. This is illustrated in Figure 1.5. Semiconductors that are processed to contain added impurities are called extrinsic or doped semiconductors. If the semiconductor Si is doped with a pentavalent atom, such as arsenic, only four valence electrons from As participate in the covalent bonding leaving one electron left over. This extra electron introduces an energy level just below the conduction band known as the donor band. The gap between the donor band and the conduction band is minute (~0.05 eV), thermal activation at room temperature can provide sufficient energy to move the electron from the donor band to the conduction band. This is known as an n-type semiconductor and is illustrated in Figure 1.6 (A).

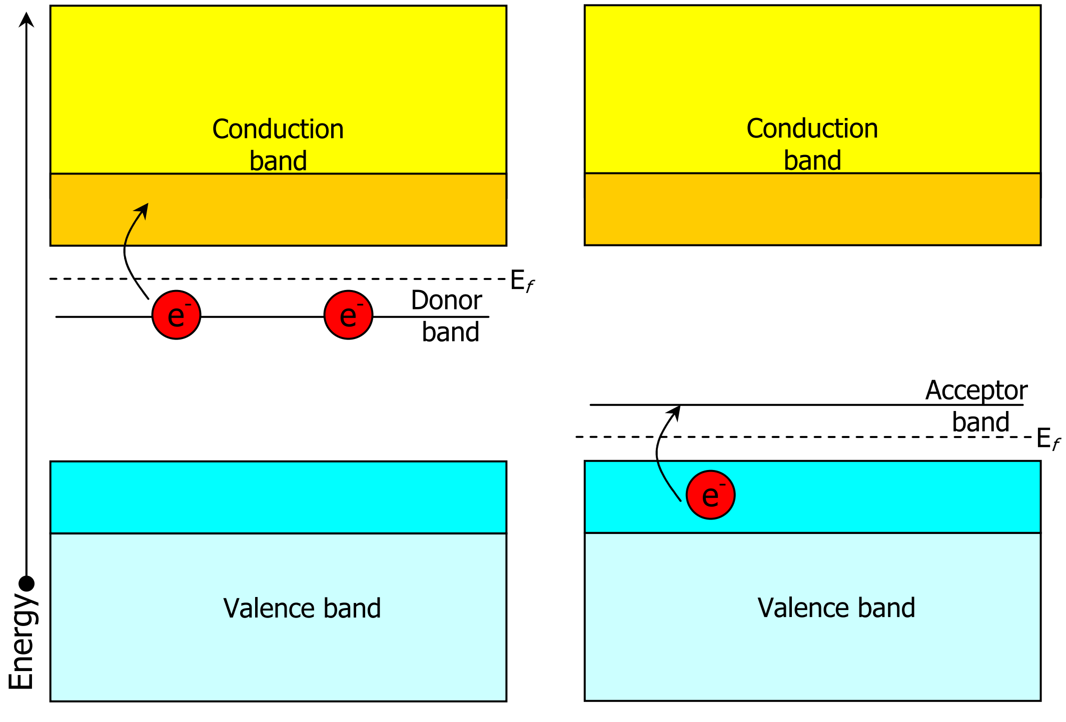

(A) (B)

Figure 1.6 Doped Semiconductors
(A) n-type (B) p-type

Doping Si with a trivalent impurity such as boron introduces an energy band just above the valence band. This is known as the acceptor band. Excited electrons from the valence band are introduced into the acceptor band and give rise to mobile hole charge carriers in the valence band. Since the charge carriers are positively charged holes, this type of semiconductor is known as a p-type semiconductor.

1.2.3 Preparatory Cleaning of Si

The treatment and preparation of the Si surface is a critical process in order for it to be used as the base for fabrication of IC devices. The normal function of a MOSFET can be adversely affected by trace amounts of contaminants. Particles, metallic ions, organic, chemical and biological contamination are common. As IC devices become smaller, leading to a smaller gate oxide and channel length, the threshold voltage needed to run the IC device decreases. This means that contaminant control is ever tightening. Contamination of the surface preparation of Si could lead to horrendous results in the fabrication of IC devices during later steps or during end user applications[2,6,7].

Common Designation	Composition	Purpose
Piranha	H_2SO_4:H_2O_2 (2:1 or 4:1 @ >100°C)	Removal of organic films.
DHF	HF + H_2O	Etching oxides
SC1	NH_4OH:H_2O_2:H_2O (1:1:5 @ 70°C)	Removal of organics, surface impurities/particulates
SC2	HCl:H_2O_2:H_2O (1:1:5 @ 70°C)	Removal of metallic impurities

TABLE 1.1 Common RCA surface preparation solutions

A common pretreatment of Si surfaces developed and implemented by the Radio Corporation of America in 1965 has become the industry standard for Si surface preparation and has withstood the test of time and scrutiny[6]. Known as the RCA clean, this method of Si sample preparation involves several chemical steps. Table 1.1 shows the various cleaning pretreatments. Ultrapure water (UPW) plays an extremely important role since all the chemical cleaning steps are aqueous. Chapter 2 and 3 studies the effects of ultrapure water (UPW) with and without contaminants on Si substrate surfaces.

A sulphuric acid – hydrogen peroxide mixture, commonly known as a Piranha Etch, is employed for removal of significant amounts of organic films such as that used in photolithography. Volume ratios of H_2SO_4:H_2O_2 range from 2:1 to 4:1, with exposure times for 10-15 minutes at temperatures above 100^oC.

A Standard Clean 1 solution (SC1) is composed of a mixture of ammonium hydroxide, hydrogen peroxide and ultrapure water (NH_4OH:H_2O_2:H_2O - 1:1:5). This treatment is typically used for removing organics, surface impurities and particulates. The treatment is applied for 10 minutes at a temperature of 70^oC. Oxidation by the peroxide and solvation by ammonium hydroxide remove organics. This process can be characterized by the continuous formation and dissolution of a hydrous oxide film on the surface. This also helps in the removal of particulates. Metal contaminants are also removed through their dissolution and complexation with NH_3. SC1 treatment leaves a Si surface with a chemically formed clean oxide which can be rinsed with ultrapure water (UPW) and etched with an HF etch solution.

For the removal of metallic impurities, a Standard Clean 2 (SC2) solution is employed. Composed of hydrochloric acid, hydrogen peroxide and UPW (1:1:5 – HCl:H_2O_2:H_2O) this solution is also applied for 10 minutes at 70^oC. This process mainly removes alkali ions and residual metals that survive the SC1 cleaning step.

Hydrofluoric acid (HF) etching of Si surfaces removes chemical, thermal and native oxides leaving a hydrogen terminated, or passivated, surface. Dilute hydrofluoric acid (DHF) is often employed. This is made by diluting HF (~49%) with ultrapure deionized (DI) water (~18.2 MΩ cm) usually to 4.9%-0.49% concentrations of HF.

It has also been found to be advantageous to control the pH of HF using ammonium fluoride (NH_4F). This buffered HF (BHF) can be employed to surfaces with applied photoresist so that the etching will not remove the photoresist polymer. It has also been found to be advantageous to use BHF when treating Si (111) single crystal substrates. BHF can be used to produce an ideally terminated mono-hydride surface. This is explored in Chapter 2 and 3.

1.3 Pyrolyzed Photoresist Films

Carbon materials have been extensively used as substrates and support substrates. Carbon materials exhibit good conductivity and thermal stability while providing good resistance to electrochemical and chemical attack. Carbon materials can be used for electroanalytical chemistry, electrosynthetic chemistry and energy conversion[8-15]. In particular carbon films formed by pyrolysis of photoresist films are studied in Chapter 4.

1.3.1 Carbon Films by Pyrolysis

Pyrolyzed carbon films can be made from organic gases, sublimed organic films, sputtered carbon, photoresist, and various organic films and resins. Pyrolysis of organic materials follow three general stages of structural change[16]. Pyrolysis is accomplished in an inert atmosphere under high temperatures.

The first stage is what is termed the precarbonization stage from room temperature up to 300 °C. Visually, the material turns black in color accompanied by a rapid weight loss due to evaporation of solvent. All 'loose' molecules of excess solvent are removed.

The carbonization regime follows in the temperature region between 300 and 500 °C. Oxygen, nitrogen, chlorine and other excess 'loose' atoms and molecules are thermally removed. This regime is punctuated by the increase in the size as the conjugated carbon system gets longer. The time needed for this process is greater than that of the first stage, due to the increasing difficulty in removing molecules while building up a polymeric network with increasing cross linked chains. A loose network of linear conjugated systems, which are still electronically isolated from one another is the end result of this stage. The material still contains at least one hydrogen atom for every two carbon atoms.

The next temperature regime between 500 and 1200 °C results in the gradual elimination of hydrogen atoms from the network of carbon polymeric chains. At this juncture the electrical conductivity increases rapidly as the polymeric chains become an interconnected conducting network. The density and hardness of the carbonaceous material also increases.

Heating above 1200 °C is not explored in this dissertation, but is characterized by crystallization of the carbon components as defects are progressively removed.

1.4 Interconnect Materials

1.4.1 Cu Interconnects

Copper (Cu) plays a singular role in the IC industry and has supplanted aluminum as the material of choice for interconnect fabrication. Cu has a resistivity of 1.67 μΩ·cm, making it more conductive than Al which has a resistance of 2.66 μΩ·cm. As an electric field is applied to a system, metal atoms can have a tendency for electromigration, or movement across the system with the applied field. Electromigration is a serious problem and can cause device failure. Aluminum has a greater tendency towards electromigration while copper exhibits a better resistance. Therefore the IC that is made with Cu interconnects can operate at higher electric fields and under greater stress than Al interconnects. Figure 1.7 illustrates a 0.13 μm MOSFET IC device and the connecting Cu interconnect lines.

Unlike Al, Cu can be easily adapted for electrochemical systems. This is advantageous, since Al can only be deposited onto substrates using ultra high vacuum (UHV) techniques. UHV routes are time consuming and expensive. Electrochemical means can be conducted on a bench top under atmospheric pressure and at room temperature with minimal cost and much less time. These reasons lend themselves to the replacement of Al with Cu as the new generation of interconnect material for ICs. With decreased resistance-capacitance (RC) coupling delay, IC devices with more conductive interconnects in conjunction with low-k interlayer dielectric materials will operate with considerably higher speeds and less power

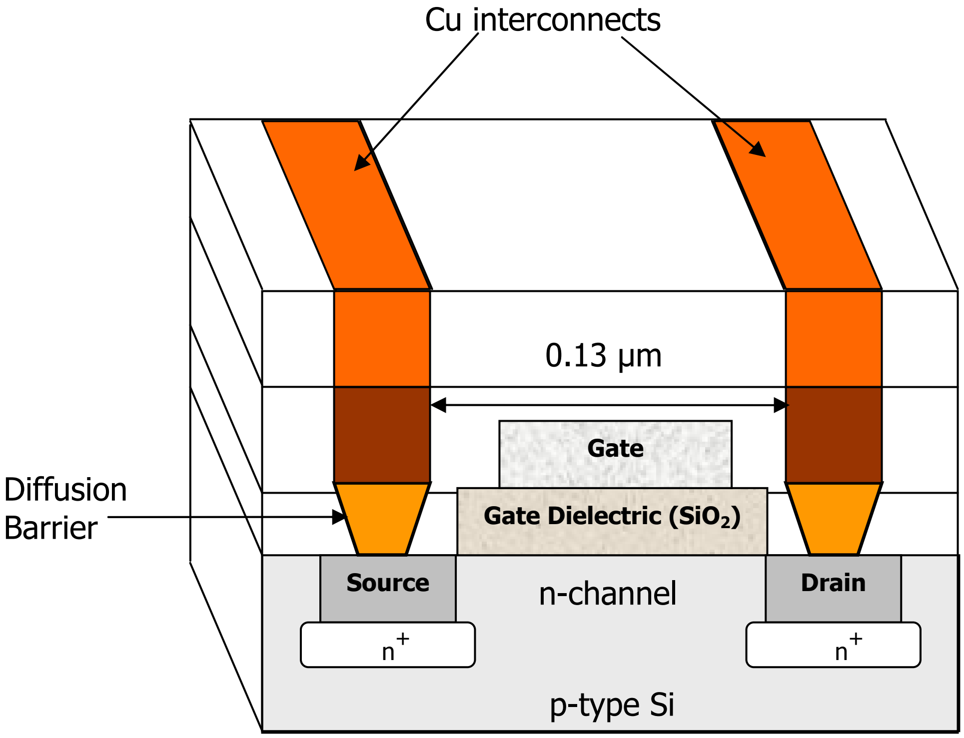

Figure 1.7 Cross sectional view of a 0.13 μm MOSFET and Cu interconnects

consumption. Chapter 5 and 6 will deal with issues for Cu interconnects using new possible diffusion barrier materials.

1.4.2 Silver as Another Possibility

Silver (Ag) is a potential candidate for the next generation of interconnect materials. Its higher conductivity (1.59 μΩ·cm) make it a boon to an IC industry that is constantly looking for better materials to increase operating speeds. Ag has shown poor adhesion to Ru and Ir metal. It would be advantageous to couple Ag/Cu multilayer on Ru or Ir in order to solve the problem of poor adhesion. These processes are seen to afford fine control via electrochemical techniques. Chapter 5 will also explore the creation and characterization of Ag/Cu multilayers as a potential material for interconnects.

1.5 The Importance of Iridium and Ruthenium as Diffusion Barriers for Interconnects

Although it has been stated previously that Cu is more resistive to electromigration than Al, that is not to say that intermixing of Cu species into the Si bulk does not occur. Thermally induced diffusion of Cu can still occur through a Si bulk and is held in check with a diffusion barrier between the Si substrate and the Cu interconnect lines. This barrier is dubbed the *diffusion barrier*, and provides a separating line between metallic interconnect material and the bulk Si semiconducting material.

Currently tantalum (Ta) and tantalum nitride (TaN) are used as a diffusion barrier to contain Cu interconnects from device contamination[17-22]. Current configurations of Cu-seed/Ta/TaN stacks require very fine control in order to avoid poor sidewall coverage and large overhangs surrounding the vias, leading to Cu electrofill close-off and the creation of unwanted void defects. There have been previous reports of direct Cu electroplating onto diffusion barrier films on Si substrates[23,24], but thin barriers of TaN are too resistive (>200 $\mu\Omega$ cm) for direct Cu electroplating[25]. It is clear that new diffusion barrier materials need to be explored.

1.5.1 Ir: Uses and Possibilities

Ir (Ir) is a hard, air stable transition metal element with a high melting point (2466 ^{o}C) and an unusually high corrosion-resistance, withstanding attack even by aqua regia. Presently, Ir is currently explored and used as electrode material for ferroelectric non-volatile random access memories (FRAMs) [26-29] and has been studied and used for field effect transistors. [30,31] FRAMS combine the benefits of small direct random access memory (DRAM) cell sizes, fast read and write behavior, low power needs, and nonvolatility to give small memory devices which are ideally suitable for mobile applications and ever popular personal digital assistants (PDAs.) A basic FRAM capacitor consists of some ferroelectric material, such as lead zirconium titanate ($Pb(Zr,Ti)O_3$ or PZT) sandwiched between two metal electrodes, which are in place on a Si substrate device. Ir has been seen as an ideal material for FRAMS because while being a good conductive electrode, it is thermally stable up to 700°C and adheres well to Si (Si) substrates as well as being a good oxygen diffusion layer [32,33].

As well as being used in ferroelectric devices, there is the possibility that Ir may be an ideal candidate for as a copper diffusion barrier in the sub-0.13 μm generation intergrated circuit. Ir has a face-centered cubic crystalline structure and a high electrical conductivity (4.7$\mu\Omega$ cm) and according to the Cu/Ir binary phase diagram[34], there is limited solid solubility of Ir with Cu at 700° C. This feature is of principal importance in investigating Ir as a contending diffusion barrier for Cu interconnects in next generation integrated circuit (IC) devices. Currently tantalum (Ta) and tantalum nitride (TaN) are used as diffusion barriers to contain Cu interconnects from device contamination[17-22]. Current configurations of Cu-seed/Ta/TaN stacks require very fine control in order to avoid poor sidewall coverage and large overhangs surrounding the vias, leading to Cu electrofill close-off and the creation of unwanted void defects. There have been previous reports of direct Cu electroplating onto diffusion barrier films on Si substrates[23,24], but thin barriers of TaN are too resistive (>200 μΩ cm) for direct Cu electroplating[25]. Cu nucleation studies on Ir are examined in Chapter 5.

1.5.2 Ruthenium: Possibilities

Ru is another candidate in the search for new diffusion barrier materials. Like Ir, Ru is also an air stable transition metal with high melting point (2310 °C) and is nearly twice as thermally and electrically conductive (7.6 μΩ.cm) as Ta. More importantly Ru, along with Ta and Ir, shows negligible solid solubility with Cu even at 900 °C based on the binary phase diagrams[34]. Arunagiri et al. have studied Cu nucleation on Ru using current transient techniques as well as observing wetting behavior under thermally annealed conditions. Initial studies conclude that Ru is indeed a very promising candidate for diffusion barrier material. Chapter 6 will discuss some preliminary studies into the exploration of Cu interactions with Ru and its oxide RuO_2.

1.6 ELECTROCHEMICAL TECHNIQUES

This section will give some basic understanding of the electrochemical techniques that are the basis for much of the studies conducted in this dissertation. Electrochemistry can be defined as the study of the interchange of chemistry in various media and electricity. The electrochemical studies in this dissertation mainly deal with the study of chemical reactions that occur under electrical control. That is to say that electrical energy is the driving force for chemical reactions. These chemical reactions are invariable either *cathodic* (reducing) or *anodic* (oxidizing). Understanding the heterogeneous nature of electrochemical systems and the electrochemical variables of potential land current are some of the fundamental concepts of electrochemistry.

1.6.1 The Dynamic Heterogeneous Nature of Electrochemistry

Electrochemical reactions take place at the interface of some electrode substrate and some conducting electrolyte solution. It is important to realize that only the part of the electrode in immediate contact with the electrolyte can be affected. As chemical reactions at the electrode/electrolyte interface occur, it is important to realize that the composition of the electrolyte varies with proximity to the electrode.

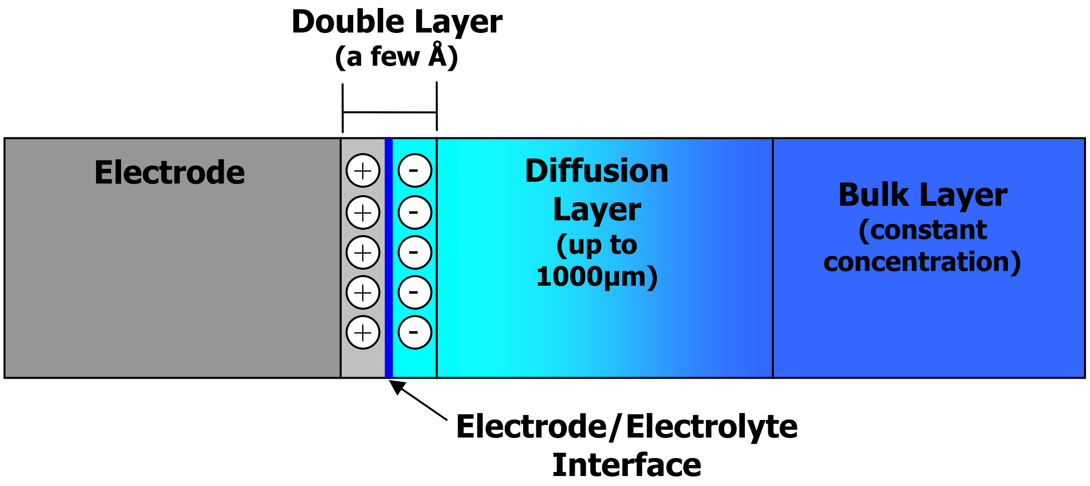

Figure 1.8 Zones of an Electrochemical System

At the electrode/electrolyte interface there is a very small area where the distribution of mobile electrons of the electrode are different than the rest of the electrode. It is at the interface, also, where the electrolyte interacts with the electrode. This region at the interface is called the double layer region. This interfacial zone on the two sides of the interace has dimensions only a few tens of angstroms thick since this is the scale at which intermolecular and interatomic forces operate. Further away from the electrode is the homogeneous bulk solution. Between the bulk region and the double layer region exists a diffusion layer zone where the concentrations of products and reactants are affected by the reactions taking place at the double layer region. This region is comparatively larger at a scale in the $10^4 - 10^7$ angstrom range. The bulk region is far from the electrode and is at a distance such that the concentration of species is constant. This is illustrated in Figure 1.8.

An overall electrochemical reaction is the chemical change accompanying charge transfer across at an electrode/electrolyte interface. Its rate is limited by the speed and amount of reactants that can be moved from the bulk solution to the double layer by *mass transport*. Mass transport can be accomplished by diffusion, convection or migration.

1.6.2 Current: Working vs. Counter Electrodes

The electrode where we study chemical reactions is our *working electrode*. Reactions at the working electrode involve a transfer of charge. Electroneutrality must be preserved as electrons are either extracted from or drawn into the working electrode for reactions to occur. To this effect a *counter electrode* is used to preserve electroneutrality by allowing electron flow and keeping charge buildup to a minimum.

It is also important to note that the flow of electrons at the electrodes are directly proportional to the reaction rate. Consider the equation for the total charge passed (Q):

$$Q = nFN$$

N is the number of moles of reactants involved, n is the number of electrons per molecule involved in a reaction, and F is Faraday's constant of 96,485 coulomb/mole of electrons. The rate of reaction, and therefore the rate of change in total charge is expressed:

$$dQ/dt = nF\, dN/dt = i$$

where it is seen that the rate change in total charge dQ/dt is the current i. Current (i) is expressed in terms of amperes.

1.6.3 Potential: Working vs. Reference Electrode

The energy required to move an electron from some arbitrary point A to point B is commonly referred to as *potential*. Specifically, potential is the amount of work required to move an electron from an infinite point in space to a point of interest, in our case, a working electrode surface. More negative potentials are reached by increasing negative excess charge on an electrode to give higher electron energies. Conversely, more positive or less negative potentials are reached by increasing positive excess charge or decreasing electron energies. When studying electrochemical systems, the potential is the voltage difference between the working electrode and a *reference electrode*. The reference electrode is independent of the chemical processes occurring at the working electrode and is established in such a way that it is in equilibrium and does not pass current usually by containing a high concentration of electroactive species that are not sensitive to current flow. Thus a reference point is provided which the working electrode can be measured against.

Figure 1.9 illustrates the standard three-electrode system by which most electrochemistry is conducted. It must be noted that current and potential can only be controlled separately, never simultaneously. Applying potential will cause current to flow while current control will proceed at a corresponding potential. A device with feedback control called a potentiostat is capable of applying current to the working – counter electrodes, while monitoring the potential of the working versus the reference electrode.

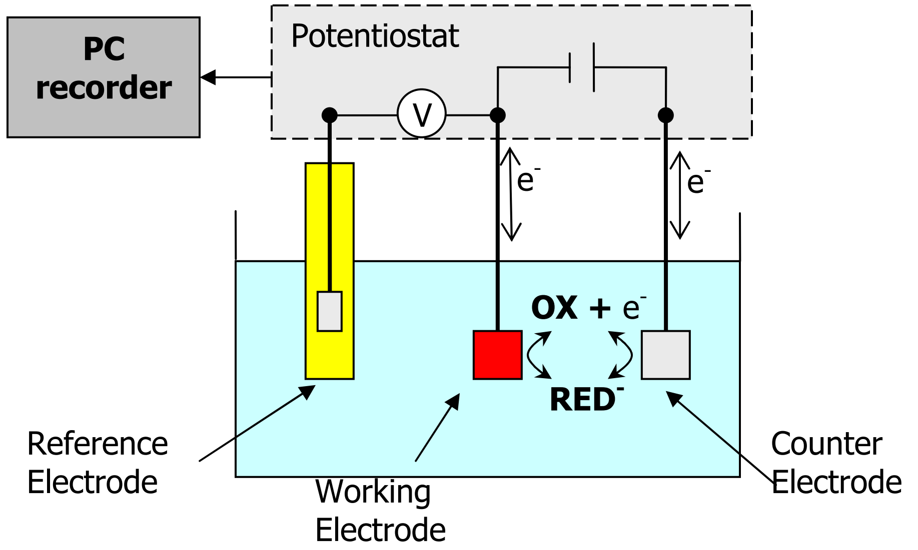

Figure 1.9 Three Electrode System

An Eg&G Princeton Applied Research model 273A Potentiostat/Galvanostat (PerkinElmer, Inc., Wellesly, MA, http:www.perkinelmer.com/) was used to obtain electrochemical data.

1.6.4 Open Circuit Potential

The OCP value is the potential of the working electrode versus the reference electrode when there is no current applied to the system. OCP is also a very electrode surface sensitive quantity and has been used extensively by this research group[35-37] for the detection of parts per trillion (ppt) level contaminants in HF solutions. Chapter 3 also uses OCP for the detection of ppt level contaminants in ultra pure water.

1.6.5 Cyclic Voltammetry

Cyclic voltammetry (CV) is an electrochemical technique where a working electrode is subjected to potential scan across a potential window. The values usually begin at the open circuit potential (OCP) and scan toward an anodic (or cathodic) vertex potential and then to an analogous cathodic (or anodic) vertex potential finishing back at the OCP. By sweeping the potential across the potential window at a preset scan rate (for example 100 mV/sec) a cyclic voltammogram (CV) plot is obtained where the y-axis is current change and the x-axis is potential (vs. the reference electrode). In this way cyclic voltammetry can simultaneously activate electron transfer and probe subsequent chemical reactions. The CV plot can give information about consequences of electron transfer and the electron transfer kinetics and thermodynamics of a given redox couple on an electrode surface. CV's are an integral part of Chapter 4, 5, and 6.

1.6.6 Chronoamperometry

The electrochemical technique of chronoamperometry (CA) involves the application of a potential step to the working electrode for a given amount of time. Essentially current is monitored with respect to time at a given potential. Depending on what type of potential is applied, oxidation (for example, stripping) or reduction (plating) of materials may be induced. A chronoamperogram of current versus time is obtained and the data may be disseminated for useful information. The CA technique is used for examining nucleation and growth mechanisms of materials on the working electrode surface.

Chronoamperometry was used in the investigation of initial nucleation of Cu on Ir electrodes in Chapter 5. Deposition of metal nuclei on foreign substrates is thought to initiate from surface defect sites such as steps and kinks, where nucleation is thought to be more energetically favorable. Nucleation is the starting process for greater metal deposition over a large surface area. Nucleation may be either instantaneous or progressive. Instantaneous nucleation is thought to occur quickly where a large number of nuclei form on active sites in a relatively short period of time. Conversely, the expansion of nuclei occurring faster than the creation of new nuclei is described as progressive nucleation. Over time, nuclei increase in number and size until coalescence of metal nuclei form a continuous thin film. By being attentive to the various parameters such as concentration, temperature, potential, etc, it is possible to tweak the quality and coating of a given film.

1.7 FTIR – ATR TECHNIQUE

Chapter 2 and 3 use fourier transform infrared spectroscopy (FTIR) and the attenuated total reflection (ATR) technique to observe the interfacial changes at the surface of Si after treatment in various aqueous conditions. Known collectively as FTIR-ATR, this is a very advantageous technique, since the Si element is not only the waveguide for spectroscopic sampling, but itself is the sampling surface.

1.7.1 Fourier Transform Infrared Spectroscopy

Infrared spectroscopy is the study of the infrared radiation with matter. Infrared radiation typically exists at the range of 4000 to 400 cm^{-1}. Different chemical functional groups tend to absorb infrared radiation at certain wavenumber ranges regardless of the structure of the whole molecule. The development of the Michelson interferometer in 1880 led to the advent of Fourier Transform technology (illustrated in Figure 1.10). Fourier Transform is essentially the interconversion of time domain to frequency domain signals. Although the calculations required to convert intereferograms to spectrum were time prohibitive and labor intensive then, the subsequent development of the Fast Fourier Transform computational algorithm at Bell labs in 1965 led to a method by which Fourier Transform could be used practically. By coupling the Fourier Transform algorithm to computer technology it was finally feasible to perform FTIR[38].

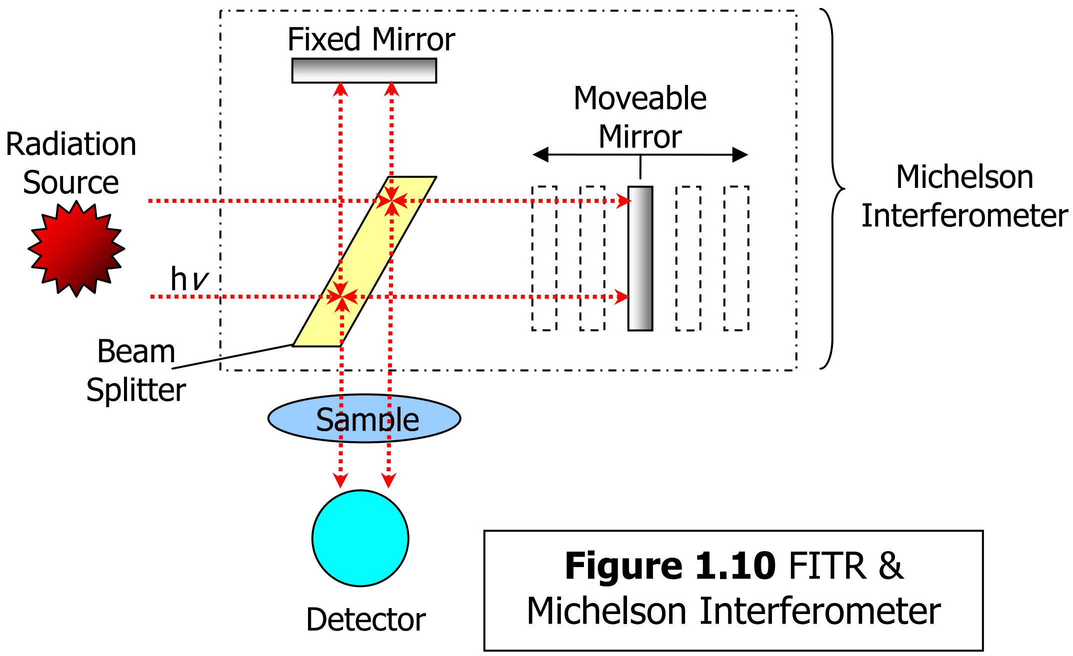

Figure 1.10 FITR & Michelson Interferometer

The Michelson interferometer produces interference spectra by splitting a beam of monochromatic light (infrared radiation) so that one beam strikes a fixed mirror and the other a movable mirror. As the movable mirror travels along its path, the light beams merge back together at both constructive and destructive interferences. Thus, as the reflected beams are brought back together, a plot of the variation of light intensity with optical path difference is measured by the detector to give an interferogram. This interferogram is Fourier transformed to produce the spectrum of intensity vs. wavenumbers.

The interferogram is the sum of sinusoidal signals added together. Fourier transformation to produce a spectrum can be generally thought of as the calculation of the mathematical integration for the interferogram.

The major advantages of using FTIR are seen in its throughput, resolving power and reproducibility, and the time needed to take an FTIR spectrum. FTIR spectrometers detect all wavenumbers of light at once. Since an FTIR spectrometer has no slits for radiation attenuation, there is a much greater signal-to-noise ratio (SNR) because the radiation passes directly through the sample to the detector with no extra steps. This is known as throughput or Jacquinot advantage. This not only cuts down on acquisition time, but also allows for the Felgett or multiplex advantage which comes from the fact that the SNR is proportional to the square of the number of scans (N):

$$\mathrm{SNR} = (N)^{1/2}$$

so that the increased number of scans capable on an FTIR spectrometer vs. a normal dispersive instrument turns into a real improvement. For example, a normal dispersive instrument may make one scan in 10 minutes, while the FTIR instrument may take 400 scans in 10 minutes. Thus an FTIR has a SNR advantage of roughly $(400)^{1/2}$ (this is a factor of 20).

1.7.2 Attenuated Total Reflection

FTIR can be coupled with *attenuated total reflection* (ATR) techniques to provide an extremely surface sensitive means of probing interfacial properties of Si substrates[39]. ATR technique can also be used to obtain spectra for other solids, liquids and thin films. The core of the ATR technique is a crystal that has a relatively high refractive index and is transparent to infrared radiation. Consider any of the materials commonly used for internal reflection elements (IREs – also called ATR elements) listed in Table 1.2.

Material	Transmission Range (cm^{-1})	Refractive Index
KRS-5 (thallium bromide/thallium iodide)	20,000-250	2.35
ZnSe	20,000-600	2.42
Si	8300-660	3.42
Ge	5500-600	4.0

TABLE 1.2 Common Internal Reflection Elements

As the infrared radiation passes through a face of a parallelogram shaped ATR element, it will reach the top surface. With the proper refractive index and angle of incidence, the radiation will reflect off the top surface and undergo total internal reflection until the radiation passes through the length of the ATR element.

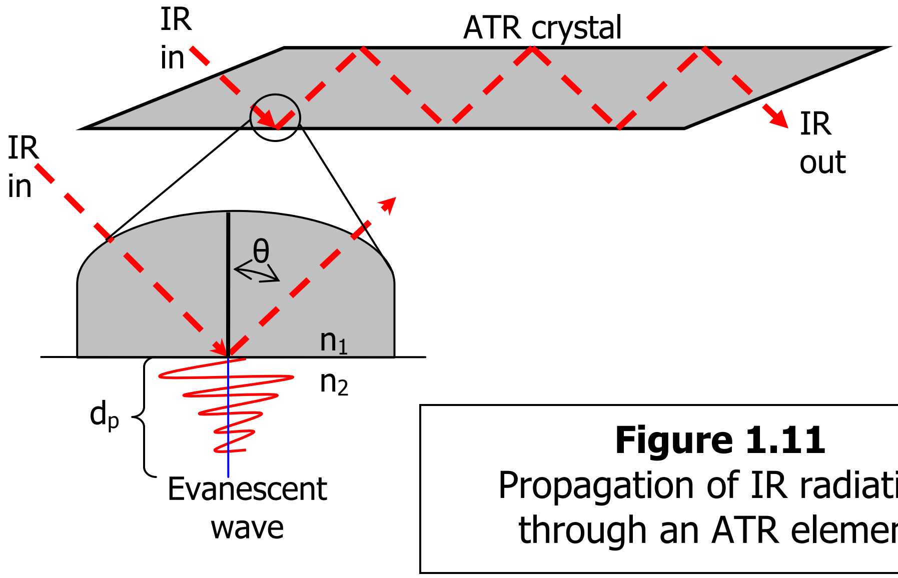

Figure 1.11
Propagation of IR radiation through an ATR element

If the angle θ at which the infrared light impinges upon the interface between the ATR crystal (the more dense medium) and the air (the less dense medium) is greater than the critical angle then the light will totally internally reflect within the IRE. Figure 1.11 illustrates the phenomenon of IR radiation passing and reflecting through an ATR element. The number of reflections (N) of a given length (L) and width (W) is given by :

$$N = \frac{L}{W}(\text{cot angent } \theta)$$

Each reflection generates an electrical evanescent electrical field (E) into the lighter medium which decays exponentially with a distance (z) into the lighter medium:

$$E = E_0 \, e^{-z/\mathbf{d}_p}$$

Where E_0 is the intensity of the incident radiation and d_p is the depth of penetration of the evanescent wave. The penetration depth (d_p) is defined as[39]:

$$d_p = \frac{\lambda}{2\pi n_1 \sqrt{\sin^2\theta - (\frac{n_2}{n_1})^2}}$$

where $\boldsymbol{\lambda}$ is the wavelength of radiation, n_1 is the index of refraction for the ATR element and n_2 is the index of refraction for the lighter medium. The evanescent wave penetration falls off exponentially with increasing distance to the surface even as the wave moves in all directions at the interface. Thus, interaction of the evanescent wave with the interface leads to infrared radiation absorption and signal enhancement for each internal reflection. The ATR technique is a very powerful tool allowing for discernment of very fine surface structure.

1.8 X-Ray Diffraction

Solid crystalline matter invariably is arranged in regular three-dimensional patterns such that a certain a smallest definable unit, or *unit cell*, repeats over and over again in space. Since each element has unique electron arrangements, it may be surmised that each different crystalline solid will be different from one another due to the differences in elements and electron arrangements. X-ray diffraction is used in this dissertation work to characterize materials and their aforesaid crystallinity.

1.8.1 XRD Fundamental Working

X-ray generation is accomplished in an x-ray tube where a focused electron beam is accelerated across high voltage field towards a target. As the accelerated electrons collide with the atoms on the target, x-rays with energy charactertics particular to the target are emitted towards a sample for study[40,41]. Common targets used in x-ray tubes are listed in Table 1.3.

Target Element	Kα radiation wavelengths (Å)
Cu	1.54
Ag	0.559
Ni	1.66
Co	1.79
Mo	0.71

Table 1.3 X-ray Wavelengths Target Elements

As an x-ray beam impinges on the sample to be studied, interactions with electrons occur resulting in scattering. Some x-rays are scattered into the sample, while other x-rays undergo destructive interference with each other. Detection of x-rays occurs from deflected x-rays that do not change wavelengths. Such x-rays are said to be diffracted x-rays. These diffracted x-rays undergo scattering in such a way that constructively interfere with other x-rays so they escape due to the ordered nature of the sample.

Figure 1.12 illustrates the diffraction of x-rays from a crystalline solid. Consider a series of atomic planes separated by an interplanar spacing d. Two incident x-rays (AB, and A′B′) with a wavelength λ impinge the surface and reflect off in the direction of CD. For x-ray A′B′ to reinforce reflection at C, the x-ray must arrive at point C in phase with x-ray AB.

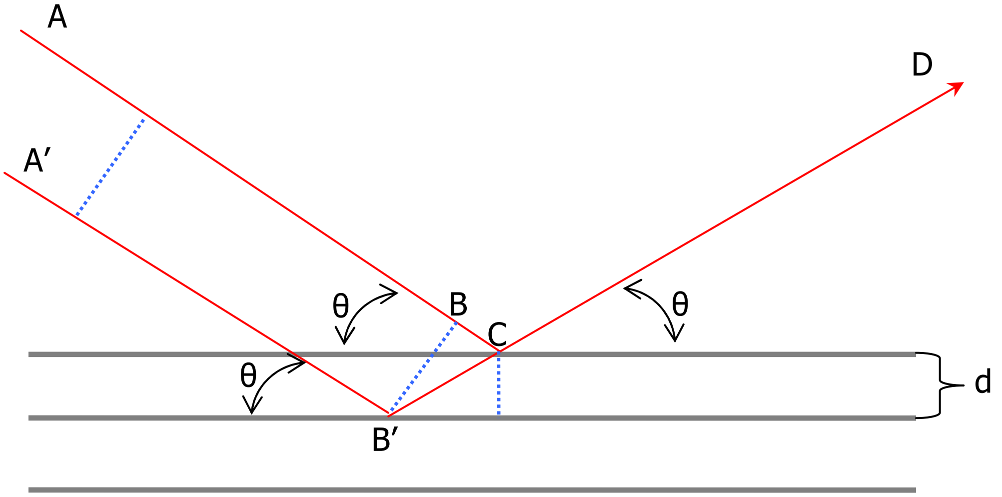

Figure 1.12 X-ray diffraction in a crystalline solid

This will be true if:

$$B'C - BC = n\boldsymbol{\lambda}$$

The integer n is seen to represent the order of diffraction as it relates to linear-lattice diffraction cones for constructive interference[40, page 127].

or by simple trigonometry:

$$B'C = \frac{d}{\sin\boldsymbol{\theta}}$$

and

$$BC = B'C\cos 2\boldsymbol{\theta} = \frac{d(\cos 2\boldsymbol{\theta})}{\sin\boldsymbol{\theta}}$$

by substitution:

$$\frac{d}{\sin\boldsymbol{\theta}}(1-\cos 2\boldsymbol{\theta}) = \frac{d}{\sin\boldsymbol{\theta}}2\sin^2\boldsymbol{\theta} = n\boldsymbol{\lambda}$$

so that

$$2d\sin\boldsymbol{\theta} = n\boldsymbol{\lambda}$$

This is Bragg's Law or Bragg's equation. It is the expression that states that for a crystal with an interplanar spacing (d) which is diffracted with x-rays of a certain wavelength (λ), the orders of reflection (n) will only occur at precise values of refraction angles (θ) which follow Bragg's Law.

Therefore, when the x-ray diffraction pattern is recorded, peaks corresponding to the various d spacings in the crystal lattice are recorded and the positions and the intensities of the peaks are used for identifying the underlying structure (or phase) of a given material. For example, the diffraction lines of Si (100) would be different from Si(111) even though they both are made of Si atoms. This phase identification is important because the material properties are highly dependent on structure (just think of the Si(111) and Si(100) planes).

XRD is capable of probing samples of single crystals or polycrystalline form as either films or powders. The technique has been found to provide such useful information for powder analysis, thin film analysis, texture measurements, residual stress measurements and crystallography and is used extensively in Chapters 5 and 6.

X-ray Diffraction studies were conducted using a Siemens D500 diffractometer (Siemens AG, Munich Germany, http://www.siemens.com/). The tube source was operated using CuK_α radiation which emit x-rays with wavelengths of 1.54 Å at 40kV and 30 mA. Scans of two theta (2θ) were run at 0.05^o steps and a 1 second dwell time.

1.9 Scanning Electron Microscopy and Energy Dispersive X-ray Spectroscopy

Scanning electron microscopy (SEM) technique coupled with energy dispersive x-ray spectroscopy (EDX) is a very powerful tool. While the SEM realizes the outward surface topography of a substance with a magnification in the range of 10x – 200,000x and with resolution of < 10 nm., a coupled EDX spectrometer may provide additional elemental analysis[42].

1.9.1 SEM/EDX Fundamental Workings

As electrons are accelerated through an anode, focused and channeled through an electromagnetic lens (simply an electromagnet) onto a sample as illustrated in Figure 1.13. An electron beam is created at a cathode filament made of materials such as tungsten. As electrons are accelerated toward an anode, they either hit the anode or are accelerated past the anode and down a column towards the sample of interest. The electrons next encounter an electromagnetic lens. The purpose of the electromagnetic lens is to focus and direct the beam down towards the sample. Once the beam hits the sample, secondary and backscattered electrons are ejected from the sample and collected at a detector which converts the signal for viewing on a screen image. The screen image can be photographed with Polaroid® instant photographic film (Polaroid Corporation, Waltham, MA, http://www.polaroid.com/) for permanent records. All SEM images were obtained with a JEOL JSM-T300 electron microscope (JEOL USA, Inc., Peabody, MA, http://www.jeol.com/) with an accelerating voltage of 15-25 kV and a working distance of 30-40 mm.

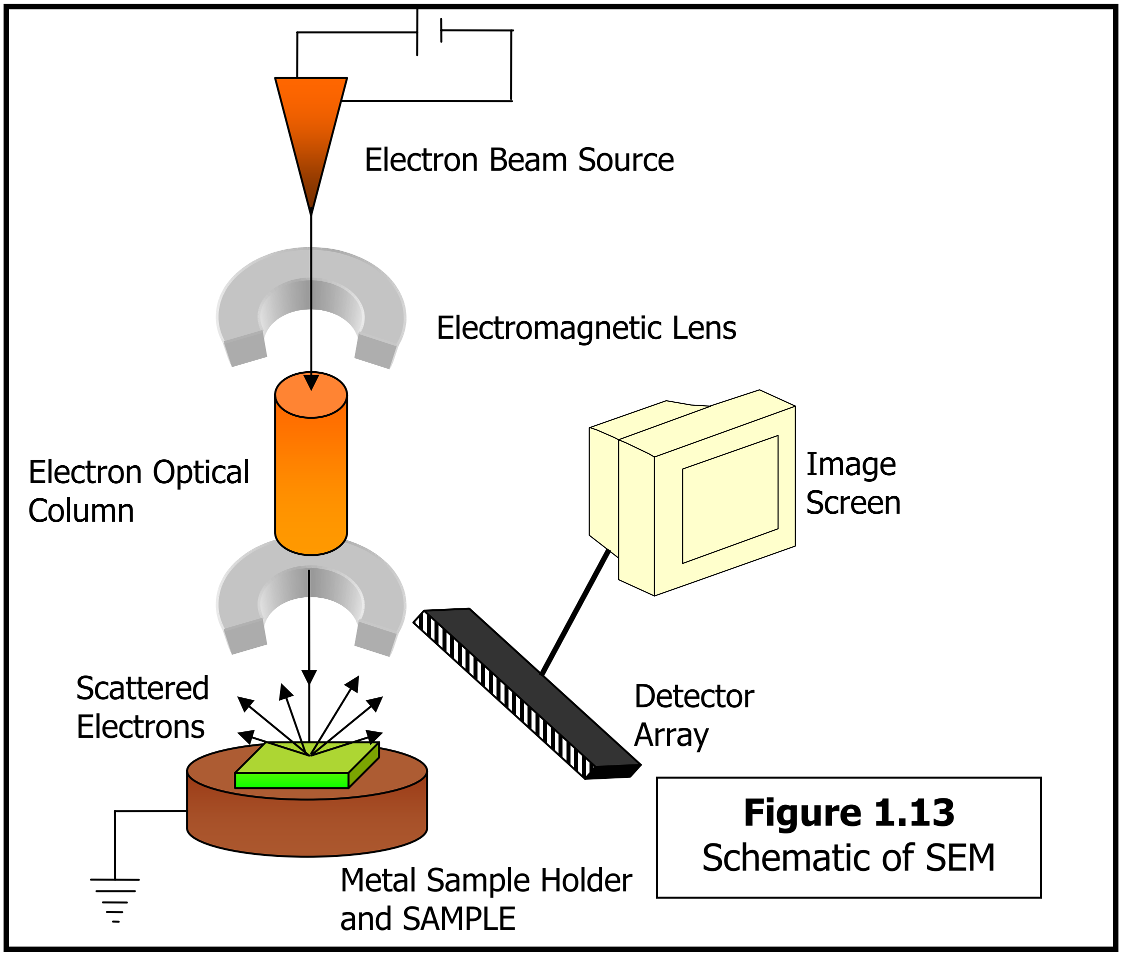

Figure 1.13
Schematic of SEM

1.9.2 Energy Dispersive X-ray Spectroscopy

Energy dispersive x-ray spectroscopy (EDX) can be coupled with SEM for a better picture of surface morphology and elemental analysis of surfaces [43]. As electrons are accelerated and strike a sample, x-rays of mainly K and L shells are generated. Electrons strike the sample and scatter sample electrons. Electrons from the outer atomic shell of the sample "drops" into the vacancy in the inner shell which has been vacated by the scattered electron. This results in a specific drop in energy which is given up in the form of x-rays. The energy levels and therefore the x-rays generated are specific to the sample element. The x-rays impinge on a semiconducting analyzing crystal converts the x-ray energy into an electron count. Detection is accomplished over a wide energy range of zero to ten keV. The resultant spectrum is distinctive to the sample area studied. A Tracor Northern TN5500 series EDX instrument (Thermo Noran, Middleton, WI, (http://www.noran.com/) for elemental analysis, was coupled to the SEM apparatus and EDX analyses were done within the energy range of 0 – 10 keV, with a proprietary automatic peak identification software included.

1.10 X-ray Photoelectron Spectroscopy

Electron spectroscopy for chemical analysis (ESCA), also known as x-ray photoelectron spectroscopy (XPS) is a widely used surface science technique. XPS is capable of providing qualitative and quantitative information on nearly all elements present on a sample (except H and He). The sample to be analyzed is irradiated with x-rays. Photoelectrons are emitted and separated by energy to be counted. The energy of the photoelectron is related to the atomic and molecular environment from which it was ejected.

1.10.1 XPS fundamentals

Photoelectrons must travel a relatively long distance to the detector. Therefore, XPS must be conducted in ultra high vaccum (UHV; $< 10^{-7}$ torr) so as to avoid losing the photoelectron on its way to the detector. For XPS analysis an x-ray impinges on an atom and interacts with an electron with a total transfer of energy leading to the ejection of the electron. This ejected photoelectron will have an energy based on the energy of the x-ray:

$$E = h\nu$$

Where the energy (E) is the product of Planck's constant ($h = 6.62 \times 10^{-34}$ Joules · Second) with the frequency of the x-ray radiation (ν). Thus as the x-ray strikes a core electron on an atom (as seen in Figure 1.14 A) there is emission if the core electron is able to overcome the binding energy (E_B).

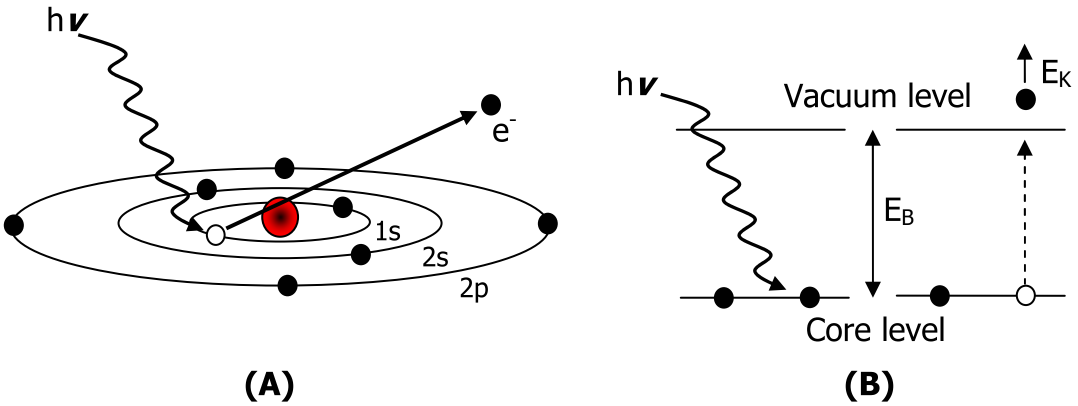

Figure 1.14
XPS electron ejection

Photoemission may be viewed such that:

$$E_B = h\nu - E_K$$

Where E_B is the binding energy of the electron needed to escape the vacuum energy level where the atom can still exert influence on the electron. E_K is the kinetic energy of the electron that is emitted. It is this E_K of the emitted photoelectrons which are channeled through an electrostatic hemispherical electron energy analyzer onto a large area detector that are measured. The hemispherical analyzer establishes an electrostatic field to allow only those electrons of a given pass energy to arrive onto the detector itself[44].

Since the x-ray photon energy ($h\nu$) and E_k are known, E_B can be elucidated. This is important because the binding energy of core level electrons is characteristic for each element. The binding energy also provides important information about the bonding characteristics of the atom from which the core electron photoemission is detected. This chemical shift in binding energy can be seen in particular for Si. Si 2p electron will give a binding energy of 99.15 eV[45], but when it is in Si oxide (SiO_2) the 2p electrons experience a shift towards higher binding energy of 103.4 eV because Si becomes more electrophilic due to the proximity of the electron withdrawing oxygen species. A chemical shift towards lower binding energy would be seen if Si were to be in an electron donating environment.

X-ray photoelectron spectroscopy was accomplished using a ESCALAB MKII spectrometer system (Thermo VG Scientific, West Sussex, England, http://www.noran.com/) using a standard Al-K_α X-ray source at 280 watts and electrostatic analysis in constant pass energy mode of 200 eV for survey scans and 20 eV for regional scans.

1.11 References

(1) Kasap, S. O. *Principles of electronic Materials and Devices*; McGraw Hill: New York, 2002.

(2) Runyan, W. R.; Bean, K. E. *Semiconductor Integrated Circuit Processing Technology*; Addison-Wesley Publishing Company: Reading, 1990.

(3) Sands, D. E. *Introduction to Crystallography* New York, 1969.

(4) Cotton, F. A.; Murillo, C. *Advanced Inorganic Chemistry*; John Wiley & Sons: New York, 1999.

(5) Serway, R. A. *Physics for Scientists & Engineers with Modern Physcs*; Third ed.; Saunders College Publishing: Philadelphia, 1990.

(6) Heyns, M. M.; Nemanich, R. J. In *Properties of Crystalline Silicon*; 1 ed.; Hull, R., Ed.; INSPE, The Institution of Electrical Engineers: London, 1998; Vol. 20, p 219.

(7) Verhaverbeke, S.; Messoussi, R.; Morinaga, H.; Ohmi, T. In *Materials Research Society: Symposium Proceedings*; Liehr, M., Ed.; Materials Research Society, 1995; Vol. 386, p 3.

(8) Kinoshita, K. *Carbon: electrochemical and physiochemical properties*; Wiley Interscience: New York, 1988.

(9) Chen, P.; McCreery, R. L. *Analytical Chemistry* 1996, *68*, 3958.

(10) Anjo, D. M.; Karh, M.; Khodabaksh, M. M.; Nowinski, S.; Wanger, M. *Analytical Chemistry* 1989, *61*, 2603.

(11) Cabanis, G. E.; Diamantis, A. A.; Murphy Jr., W. R.; Linton, R. W.; Meyer, T. J. *Journal of the American Chemical Society* 1985, *107*, 1845.

(12) Kim, J.; Song, X.; Kinoshita, K.; Madou, M.; White, R. *Journal of the Electrochemical Society* 1998, *145*, 2314.

(13) Ranganathan, S.; McCreery, R. L. *Analytical Chemistry* 2001, *73*, 893.

(14) Ray, K.; McCreery, R. L. *Analytical Chemistry* 1997, *69*, 4680.

(15) Xu, J.; Huang, W.; McCreery, R. L. *Journal of Electroanalytical Chemistry* 1996, *410*, 235.

(16) Jenkins, G. M.; Kawamura, K. *Polymeric carbons - carbon fibre, glass and char*; Cambridge University Press: Cambridge, 1976.

(17) Hall, R. N.; Racette, J. H. *Journal of Applied Physics* 1964, *35*, 379.

(18) Sparks, D. R.; Dayananda, M. A. *"The behavior of transition metals in silicon during annealing transients" Defect and Diffusion Forum* 1988, *39*, 77.

(19) Wu, P. K.; Yang, G. R.; Lu, T. M. *Appl. Phys. Lett.* 1994, *65*, 508.

(20) Pallean, J.; Oberline, J. C.; Braud, F.; Torres, J.; Mermet, J. L.; Mouche, M.; Ermolieff, A. *J. Mat. Res. Soc. Proc.* 1994, *337*, 225.

(21) Stavrevm, J. M.; Fischer, D. C. W.; Drescher, K. M., N. *Thin Solid Films* 1997, *307*, 79.

(22) Kaloyeros, A. E.; Chen, X.; Stark, T.; Kumar, K.; Seo, S. C.; Peterson, G. G.; Frisch, H. L.; Arkles, B.; Sullivan, J. *Journal of The Electrochemical Society* 1999, *146*, 170.

(23) Radisic, A.; Long, J. G.; Hoffmann, P. M.; Searson, P. C. *Journal of The Electrochemical Society* 2001, *148*, C41.

(24) Oskam, G.; Vereecken, P. M.; Searson, P. C. *Journal of The Electrochemical Society* 1999, *146*, 1436.

(25) Takahashi, K. M. *Journal of the Electrochemical Society* 2000, *147*, 1414.

(26) Takasa, H. *Microelectronic Engineering* 2001, *59*, 237.

(27) Mikolajick, T.; Dehm, C.; Hartner, W.; Kasko, I.; Kastner, M. J.; Nagel, N.; Moert, M.; Mazure, C. *Microelectronics Reliability* 2001, *41*, 947.

(28) Minamikawa, T.; Yonezawa, Y.; Heya, A.; Fujimori, Y.; Nakamura, T.; Masuda, A.; Matsumura, H. *Thin Solid Films* 2001, *395*, 284.

(29) Lee, K. B.; Desu, S. B. *Current Applied Physics* 2001, *1*, 379.

(30) Lundstrom, I.; Spetz, A.; Winquist, F.; Ackelid, U.; Sundgren, H. *Sensors and Actuators* 1990, *B1*, 15.

(31) Lalinsky, T.; Breza, J.; Vogrincic, P.; Osvald, J.; Mozolova, Z.; Sisolak, J. *Solid State Electronics* 1998, *42*, 205.

(32) Nakamura, T.; Nakao, Y.; Kamisawa, A.; Takasu, H. *Japanese Journal of Applied Physics* 1994, *33*, 5207.

(33) Jeon, Y.; Seon, J.; Joo, J.; Oh, K.; Roh, J.; Kim, D. *Applied Physics Letters* 1997, *71*, 469.

(34) *Binary Alloy Phase Diagrams*; Second ed.; Materials Information Society:, 1990; Vol. 2.

(35) Chyan, O. M. R.; Chen, J.-J.; Chen, L.; Xu, F. *Journal of The Electrochemical Society* 1997, *144*, L17.

(36) Chyan; Chen, J.-J.; Xu, F.; Sees, J. A.; Hall, L. H. *The Analyst* 2000, *125*, 175.

(37) Chyan, O. M. R.; Chen, J.-J.; Chien, H.-Y.; Wu, J. J.; Lie, M. *Journal of The Electrochemical Society* 1996, *143*, L235.

(38) Smith, B. C. *Fundamentals of Fourier transform infrared spectroscopy*; CRC Press: New York, 1996.

(39) Harrick, N. J. *Internal Reflection Spectroscopy*; John Wiley & Sons, Inc.: New York, 1967.

(40) Klug, H. P.; Alexander, L. E. *X-RAY DIFFRACTION PROCEDURES: For Polycrystalline and Amorphous Materials*; Second ed.; Wiler-Interscience: New York, 1974.

(41) James, R. W. *X-RAY CRYSTALLOGRAPHY*; Fifth ed.; Butler and Tanner LTD.: London, 1962.

(42) Venables, J. A.; Smith, D. J.; Cowley, J. M. *Surface Science* 1987, *181*, 235.

(43) Goldstein, J. I.; Newbury, D. E.; Echlin, P.; Joy, D. C.; Romig, A. D.; Lyman, C. E.; Fiori, C.; Lifshin, E. *Scanning Electron Microscopy and x-ray microanalysis: a text for biologists, materials scientists, and geologists*; Second Edition ed.; Plenum Press: New York, 1992.

(44) Vickerman, J. C., Ed. *Surface Analysis - The Principal Techniques*; John Wiley & Sons: New York, 1997.

(45) Wagner, C. D.; Riggs, W. M.; Davis, L. E.; Moulder, J. F. *Handbook of X-ray Photoelectron Spectroscopy*; Physical Electronics: Eden Prarie, MN, 1995.

CHAPTER 2

DYNAMIC CHANGES OF PASSIVATED SI (111) SURFACES IN ULTRA-PURE WATER UNDER DIFFERENT CONDITIONS STUDIED WITH ATR/FTIR

2.1 Introduction

Hydrogen passivated Si surfaces are highly desirable for the semiconductor industry. A passivated Si substrate is stable for long periods, allowing further processing of the substrate at convenient times. The ability to remove and grow stable surface oxides is central to the fabrication of Si based microelectronics[1]. Wet chemical treatment to remove native and deposited SiO_2 on a Si surface is accomplished using hydrofluoric acid (HF) etching to attain passivation. Ultra-pure water (UPW) is used for rinsing and dilution during wet chemical treatment to Si surfaces. These chemical environments must be precisely controlled in order to insure a high quality yield of product in the manufacture of IC devices. Passivated Si surfaces have been studied using multiple internal reflection infrared spectroscopy (MIRIS). Studies were done using a clean attenuated total reflection (ATR) Si element to obtain surface vibration spectra and observe changes on the Si surface. Si interaction in UPW[2-9] and with metallic contamination [10-12]has been previously studied. This study pays attention to the decrease in passivation through the vibrational spectra of the hydride regions in the initial stages of etching and oxidation of the Si (111) surface.

In this Chapter, passivated Si (111) surfaces are studied in UPW by multiple internal reflection infrared spectroscopy. A microscopically rough and monohydride terminated Si(111) surfaces are studied in UPW with and without N_2 purging. Si(111) surfaces are also studied in UPW with metal ion contamination. It is found that the dihydride site of the Si(111) surface are the most susceptible to chemical attack, with monohydride and trihydride showing reasonable stability over 120 minutes.

2.2 Experimental

2.2.1 Silicon ATR Preparation

Si N-type (111) double polished wafers (Polishing Corporation of America, 430 Martin Ave. Santa Clara, CA 95050. http://www.pcaSi.com/ - PCA#7493) with a resistivity of 1 to 10 Ωcm were used to create attenuated total reflection (ATR) elements. The crystal dimensions of 1cm x 6cm x 0.7cm with a 45° bevel face allow up to 86 internal reflections on each face to be achieved. The bevel face was ground and polished in the lab with successive Si-Carbide pad grit sizes, various micron and submicron size polycrystalline diamond suspensions, and finishing with a submicron alumina polish (all polishing pads, suspensions, finishing pads and alumina polish were from Allied High Tech Products, Inc., Rancho Dominguez, CA, http://www.alliedhightech.com/.) The roughest grit, 600, is used for shaping the bevel face. The initial polishing direction is parallel to the length of the Si substrate. The next polish at 800 grit is accomplished using a perpendicular polishing direction. This step is necessary to remove scratches from the previous steps. The next three polishing steps use a 1200 grit disk, a 1 micron diamond suspension on a Kempad finishing cloth, and a 0.5 micron diamond suspension on a Kempad finishing cloth. The polishing direction on all steps are alternated. Distilled water rinsing and observation under an optical microscope is used to ensure the quality of the polishing steps.

Sonication and rinsing after the last two steps ensure that there are no loose particles to damage the surface.

2.2.2 Cleaning Preparation

Polyfluoroalkoxy (PFA) labware used for all experiments were cleaned by multiple boilings and sonications in 10% HNO_3 and rinsed with ultrapure water. Ultrapure water (UPW) was supplied in-house via a Millipore Milli-Q® Elix 5® ultrapure water (Millipore Corp., Bedford, MA, http://www.millipore.com/) purification system (R>18.2 MΩ/cm) and used in rinsing and immersion of Si ATR substates as well as any dilution of chemicals. The Millipore UPW system affords the experiments a high degree of purity by utilizing an in series pre-treatment pack, reverse osmosis unit, final polishing module. The reverse osmosis unit removes 90-99% of contaminants (these include dissolved inorganics, colloidal material, micro-organisms, pyrogens and particulates.) The final polishing module combines ultra-violet irradiation (254 nm) and a further reverse osmosis of the previously treated water to remove trace levels of contaminants. High purity electronic grade HF (Hashimoto, Osaka, Japan), H_2O_2, NH_4OH and HCl (the previous three chemicals are from Air Liquide, Dallas Chemical Center, 13456 N. Central Expwy., Dallas, Texas, 75243, http://airliquide.com/) were employed in the preparation of the Si substrate in this study.

Si ATR elements were cleaned in hot solutions of SC1 (standard clean - 1; 1:1:5; $H_2O_2:NH_4OH:H_2O$) and SC2 (standard clean - 2; 1:1:5; $H_2O_2:HCl:H_2O$). Each hot cleaning step is followed by an etching step in 4.9% hydrofluoric acid (HF) and are rinsed with UPW. 'Ideal' monohydride terminated Si ATR elements were prepared by thermally oxidizing the Si at 1000°C under O_2, followed by a 4.9% HF etch and UPW rinse to remove the oxide. Thermal oxidation is accomplished in a quartz-tube placed in a Lindberg/Blue M Mini-Mite™ Model TF55035A tube furnace (Lindberg/Blue M, Asheville, NC, http://www.lindbergbluem.com/), fitted with a 16 set-point programmable temperature controller and an upper temperature limit of 1100°C. The final step was a 10 second immersion in 40% NH_4F (Air Liquide.)

2.2.3 Instrumentation

The ATR crystal was held in the FTIR chamber with a Pike technologies variable angle ATR accesory (PIKE Technologies Inc., 2901 Commerce Park Drive, Madison, WI 53719, http://www.piketech.com/) at an incidence angle of 45°. The IR beam is normal to the bevel face of the ATR crystal. A Bruker Equinox 55 FTIR system (Bruker Optics Inc, 19 Fortune Drive, Manning Park Billerica, MA 01821 – 3991, http://www.brukeroptics.com/) with a MCT detector (high D*, narrow band, EG&G Inc. 200 Orchard Ridge Drive, Suite 100, Gaithersburg, MD 20878, http://www.egginc.com/) was used for obtaining MIRIS spectra of the Si ATR elements. Spectra resolution is 2.0 cm^{-1}. Proprietary Bruker OPUS™ (Bruker Optics Inc, 19 Fortune Drive, Manning Park Billerica, MA 01821 – 3991, http://www.brukeroptics.com/) software was used for obtaining and manipulating data.

In order to control the amount of oxygen dissolved in solution, a glove box, model 855-AC (Plas Labs Inc. 401 E. North Street, Lansing, MI 48906, http://www.plas-labs.com/) was used in conjunction with a Model 1630 oxygen meter (KerncoInstruments Co., Inc., 420 Kenazo, El Paso, TX 79927, http://www.kerncoinstr.com/) and dissolved oxygen (DO) analyzer DO-166 (Lazar Research Laboratories, Inc., 731 N. LaBrea Ave., Suite 5, Los Angeles, CA, 90038, http://www.lazarlab.com/) Successively purging the glove box with N_2 can cause the oxygen levels to be reduced from ~21% O_2 to levels of <1% O_2 by virtue of Henry's Law[13]. Henry's Law states that the solubility of a gas in a liquid solution is proportional to the partial pressure of the gas of interest in the near vicinity over the liquid or:

$$C \alpha P$$

where C is the concentration of gas in solution and P is the pressure of gas in the atmosphere. Thus, by reducing the O_2 levels in the atmosphere of the glove box, it is possible to reduce the levels of O_2 levels in solution.

2.3 Results and Discussion:

2.3.1 FTIR Spectrum of Hydrogen Terminated Si(111)

A hydrofluoric acid passivated Si surface, shown in Figure 2.1., exhibits a complex vibrational spectrum. The microscopically rough Si(111) surface exhibits various modes which are observed in the Si-hydrogen region (2050-2150 cm^{-1}.) The monohydrides show modes at 2086 and 2071 cm^{-1} corresponding to the coupled monohydride (H-Si-Si-H) [14,15]symmetric (M_s) and assymetric (M_{as}) vibrational stretching frequencies. An uncoupled monohydride (M') exists at 2083 cm^{-1} for the uncoupled H-Si-Si[14,15]. Symmetric and asymmetric vibrational modes for dihydrides exist at 2106 (D_{ss})

and 2117 (D_{as}) cm^{-1}. A trihydride (T) peak is shown at 2130 cm^{-1}.

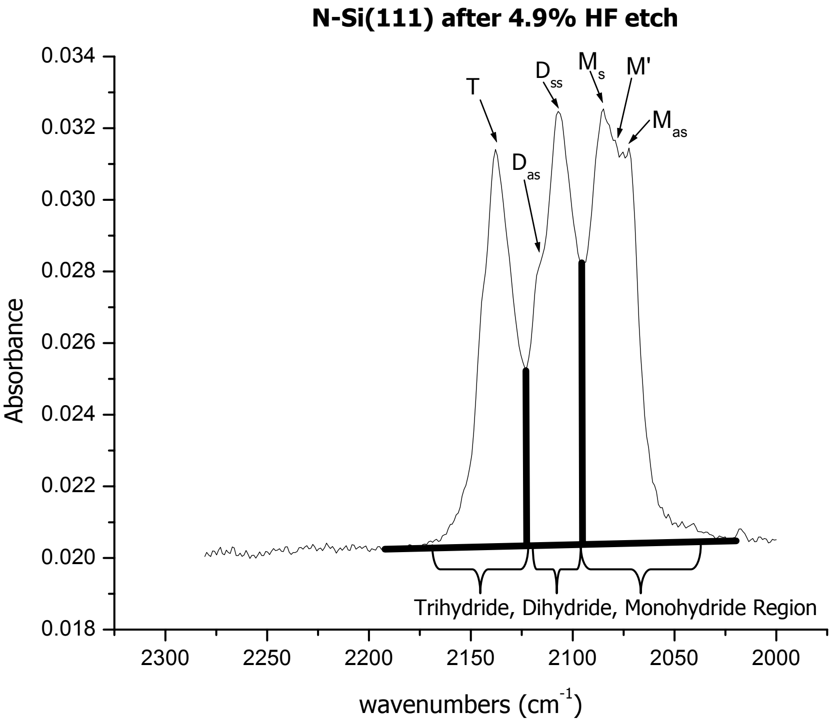

Figure 2.1 FTIR-ATR spectra of HF etched N-type Si (111).

The IR spectrum of a Si(111) ATR element immersed in UPW, shown in Figure 2.2, exhibits dynamic change in the various hydride modes over time. Baselines are offset to be able to show the differences over time. Observations of the hydride regions show that the monohydride region is more stable over time in UPW, with a sharpening of the M_s while the M_{as} mode is relegated to a shoulder and the M' mode gradually disappears. The trihydride region also shows a slight sharpening. While not as stable over time in UPW the trihydride is still present at the end of 120 minutes, while the dihydride is nearly depleted by the end of ten minutes immersion time.

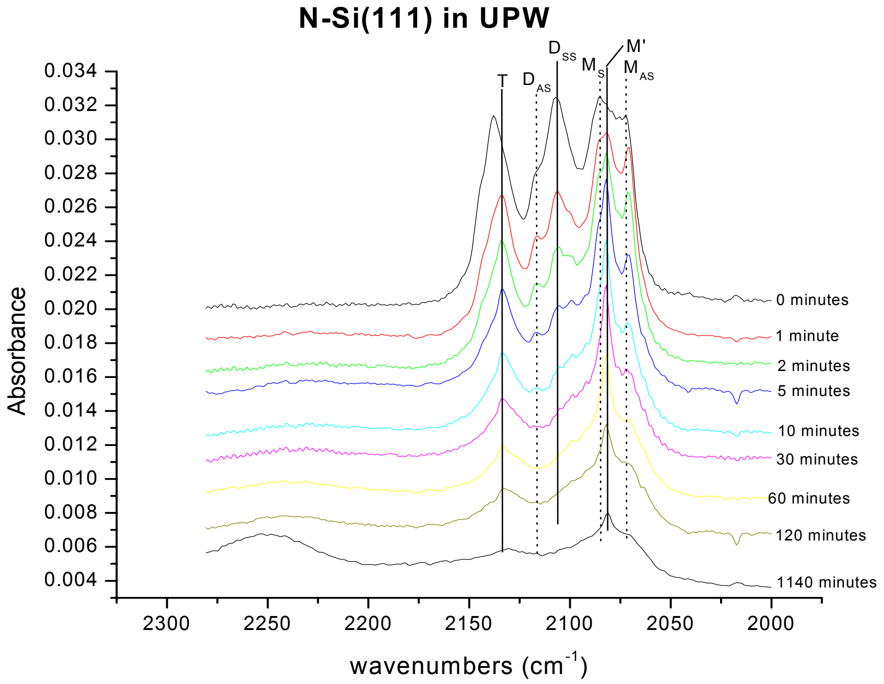

Figure 2.2 FTIR-ATR spectra of HF etched N-type Si (111) with immersion time in UPW , Hydride Region.

Semiquantitative trends and observations may be inferred by integrating the various hydride regions and normalizing the integrated values against the very first IR spectrum. Attempts to integrate specific regions encountered a prohibitive element by which it was not possible due to software and time restrictions to peak fit and integrate specific regions. The integration of the hydride regions were defined by the peak regions as seen in Figure 2.1 and delineated by the thick lines. Although some truncation and loss of integrated area is expected, trends in a semiquantitative nature may be seen.

Normalized integrated absorbances for the hydride region (Figure 2.3) corroborate these observations, showing that the monohydride region still maintains a 0.57 normalized integrated absorbance (NIA). The trihydride region retains at a 0.27

NIA, while the dihydride region drops to 0.13 NIA. The total hydride region still retains a 0.34 NIA. In the backbonded Si oxide region at 2250 - 2125 cm^{-1} we observe the emergence of a broad yet relatively small peak formation, which is much more distinct after 1140 minutes of exposure.

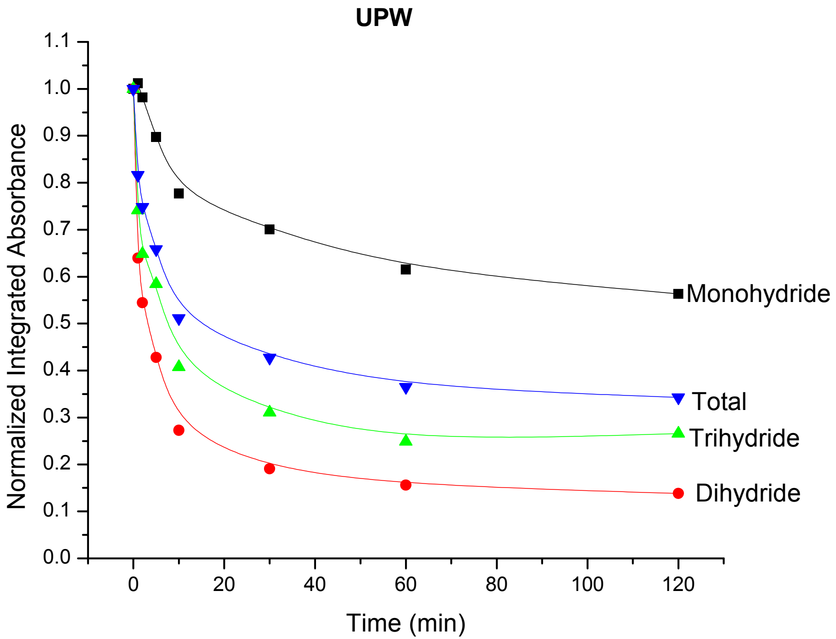

Figure 2.3 Normalized Integrated Absorbances of hydride regions of H-terminated Si (111) immersed in UPW.

Observation of the SiO_2 region (Figure 2.4) of the spectra reveal the emergence of two characteristic peaks at ~1200 cm^{-1} (longitudinal optical - LO mode) and ~1050 cm^{-1} (transverse optical - TO mode.) Noisy spectra in this region are attributed to the formation of a very thin and amorphous oxide, as well as Si lattice vibration absorptions, that exist in this region.

The sharpening of the uncoupled monohydride peak is indicative of the increase in 'ideal' monohydride sites or domain size. There have been previous reports showing that the coverage increase of similar hydride surface structures results in the peak sharpening[16,17]. A normal Si (111) surface etched with 4.9% HF has a surface that is

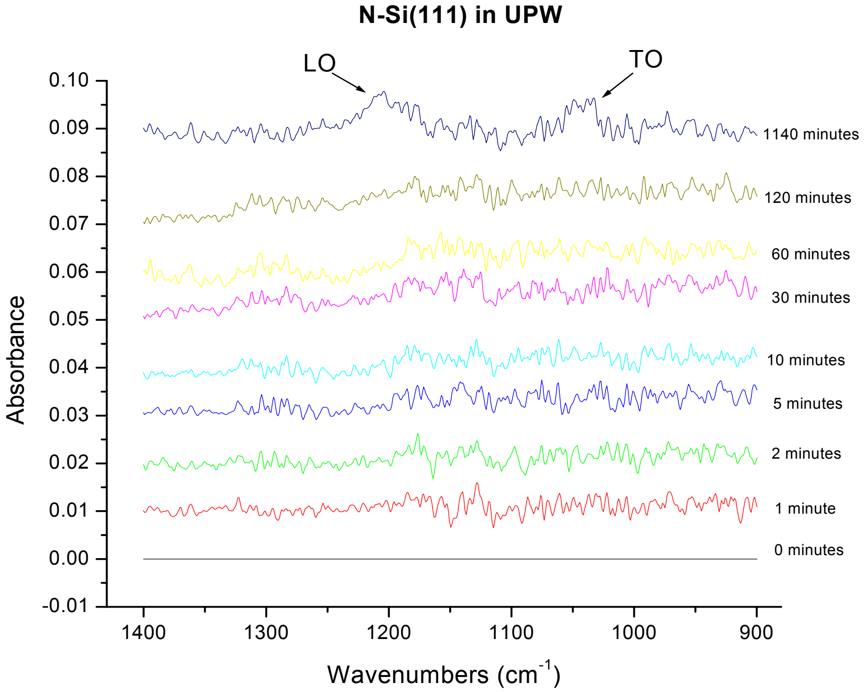

Figure 2.4 FTIR-ATR spectra of HF etched N-type Si (111) with immersion time UPW, Oxide Region.

microscopically rough containing all manner of hydride species on the surface. Figure 2.5 shows a representative model of a Si crystal structure. As one can see, the dihydride structure and coupled monohydride structure would be present at step edges and terraces, while trihydride structures would be present as islands or corners of Si steps. The uncoupled monohydride structure on the Si would be a major constituent across the Si (111) plane, but in a microscopically rough surface, all components of hydride species would be present across the Si surface. The sharpening of the M' peak could be due to the etching of (100) facets by the OH^- present in UPW, leading to the greater domain size of ideal (M') monohydride structures. The sharpening of the trihydride could also be due to the etching of dihydride species giving way to islands of

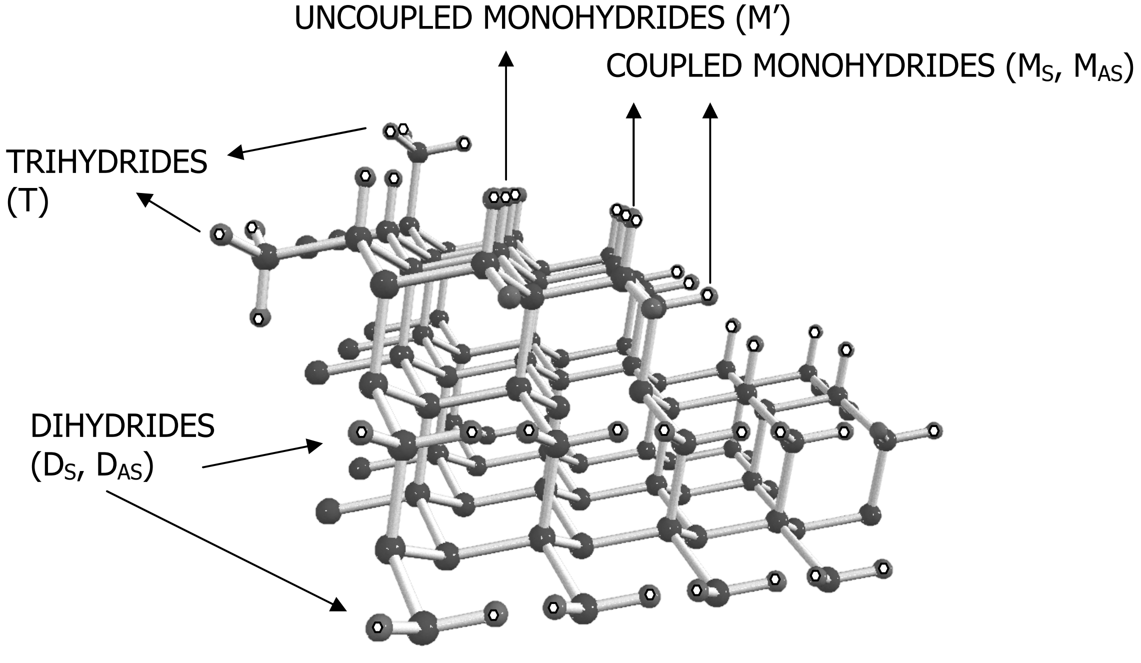

Figure 2.5 Silicon Crystal Structure

trihydride species. The rapid decrease of dihydride and disappearance of coupled monohydride peaks may be explained by their presence at the more unstable step edges where preferential etching is prone to occur. Hydroxide ion present in water is thought to insert into the Si backbond,[2,3,16]. The surface Si then dissolves in solution while the new surface is terminated by the proton from the OH^-.

2.3.2 Si(111) in O_2 Poor UPW

The effects of dissolved oxygen (DO) in UPW on hydrogen terminated Si(111) surfaces were also observed. The concentration of DO in UPW at normal ambient conditions was found to be ~8 parts per million (ppm). Immersion into a UPW solution with only ~2.5 ppm DO under a N_2 atmosphere show (Figure 2.6) that the hydrides present on the Si(111) surface are more stable and less prone to etching over time. As in the case of Si(111) immersed in normal UPW, the FTIR spectrum shown in Figure 2.6 shows a rapid decrease in the dihydride region, followed by a steady decrease of the trihydride and monohydride regions. The NIA (Figure 2.7) for dihydride region after two hours is 0.21, while the trihydride region has 0.37 NIA. The monohydride region is found to be more robust retaining a 0.73 NIA. The coupled M_{AS} and uncoupled monohydride(M_S & M') peaks resolve during exposure to the O_2 poor water. The M_s peak is eventually overshadowed by the M' peak and is seen only as a slight shoulder after two hours of immersion while the M_{AS} peak is far enough away from the coupled monohydride region where it may be seen . Total NIA is observed to decrease to 0.48 after 120 minutes of immersion in a O_2 poor UPW media. Figure 2.8 shows that after two hours of immersion, there is only slight oxide formation on the Si surface. There is also a sharpening of the monohydride and trihydride peaks, leading to the conclusion that the surface undergoes a similar, albeit arrested, development as seen in normal UPW media.

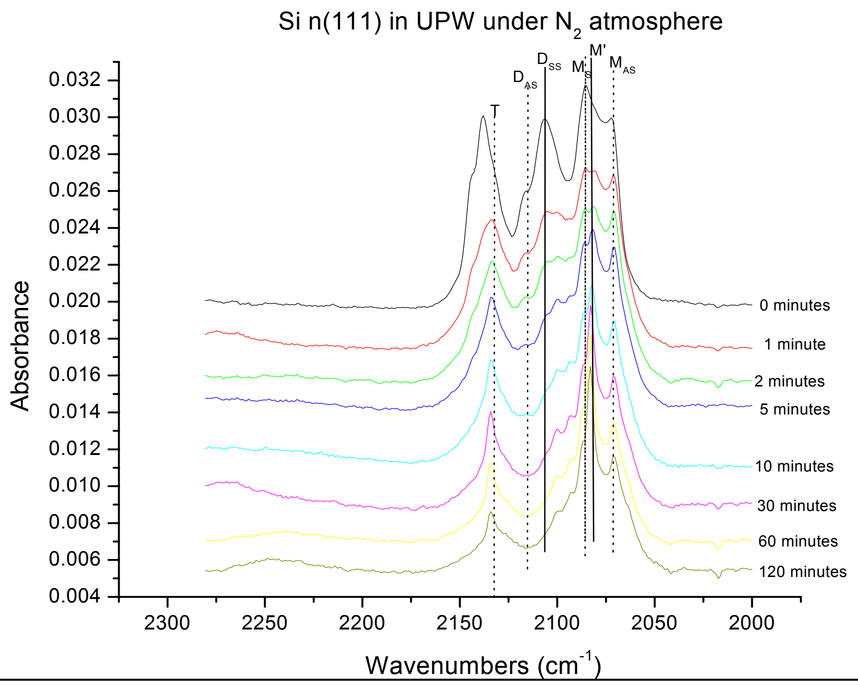

Figure 2.6 FTIR-ATR spectra of HF etched N-type Si (111) with immersion time in O_2 poor UPW, Hydride Region.

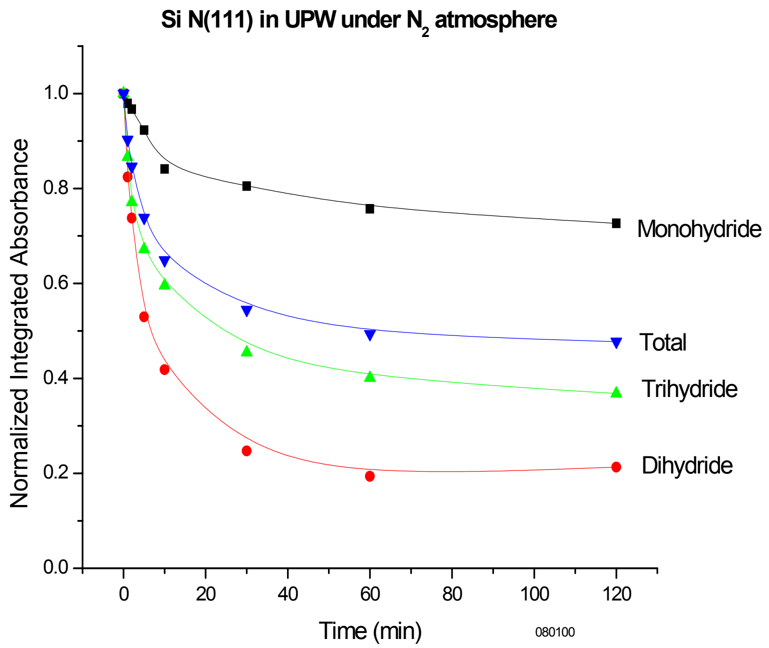

Figure 2.7 Normalized Integrated Absorbances of hydride regions of H-terminated Si (111) immersed in O_2 poor UPW.

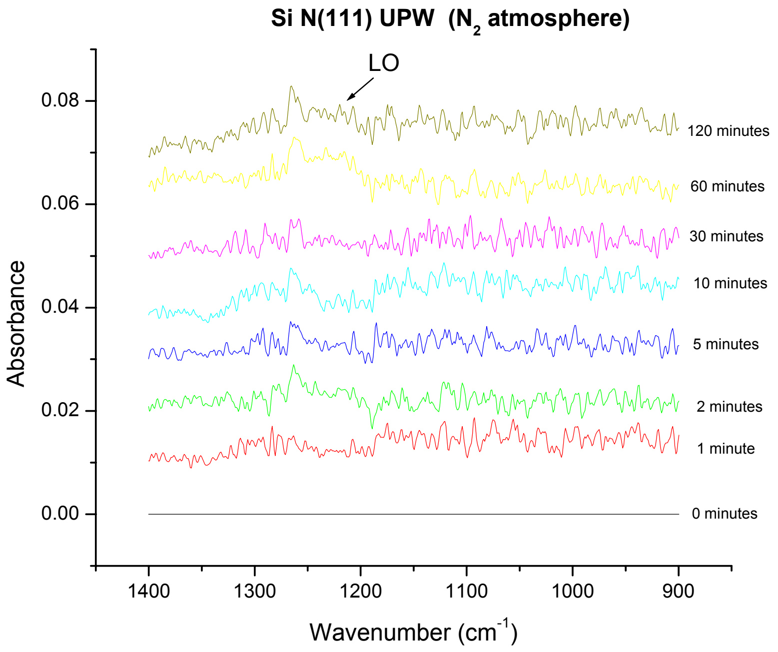

Figure 2.8 FTIR-ATR spectra of HF etched N-type Si (111) with immersion time O_2 poor UPW, Oxide Region.

Water pH indicated that there was no change in pH in the solution during experimentation for all conditions observed. There have been indications in the literature that molecular oxygen is involved by creating a Si oxide backbond [3,19,20]and that removal of DO decreases the amount of Si oxidation. There is no definitive mechanism reported to account for a decrease in DO to correspond to a decrease in the etching of Si hydrides. Molecular oxygen could interact with the Si hydride surfaces to form a backbonded Si oxide species[16]. Another possible hypothesis could lie in the solvation of DO in UPW. Dissolved oxygen should exist in such a way as to align all water and hydroxide species to align themselves with the electronegative oxygen atom facing out thus allowing for more efficient access to the Si surface.

2.3.3 The Effects of N_2 Bubbling on Si(111) in UPW

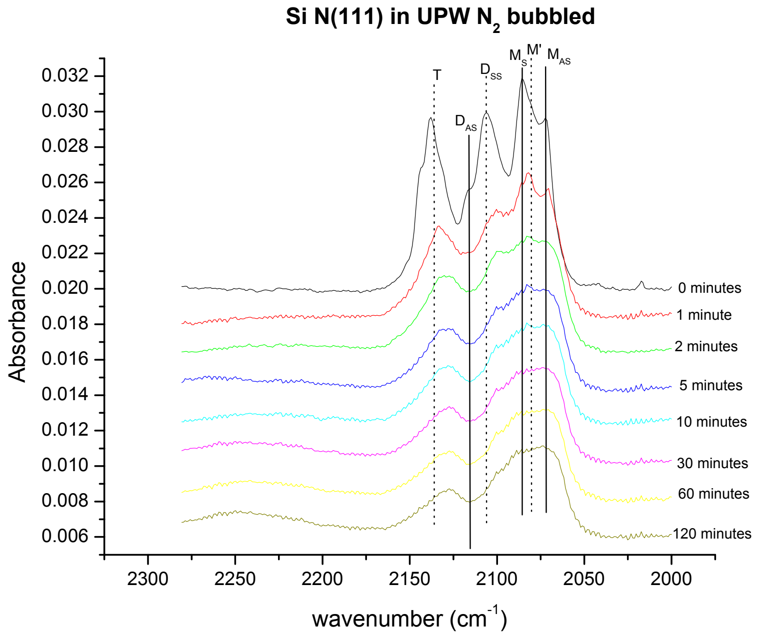

Figure 2.9 FTIR-ATR spectra of HF etched N-type Si (111) with immersion time in N_2 bubbled UPW, Hydride Region.

Nitrogen effects are also observed in a system where the DO content has been with nitrogen bubbling while Si immersion was conducted. Si immersion in N_2 bubbled media exhibits interesting behavior compared to water in which the DO concentration is controlled purely by an N_2 atmosphere, as seen in the previous section. This study of N_2 bubbling in UPW occurred through a chance encounter where control of DO concentration using N_2 was bubbled **during** the Si(111) ATR exposure. N_2 bubbling was then carried out using a Teflon™ tube which was connected to a N_2 source and bubbled directly into the UPW. A representative FTIR spectrum of a Si(111) ATR element immersed in N_2 bubbled UPW over time (Figure 2.9) shows the decrease in Hydride termination. As seen in all UPW immersions, Si hydride peaks decrease over time in N_2 bubbled UPW, but unlike previous instances, there is no sharpening for any hydride peaks. Backbonded oxide is detected but is very negligible. More telling, the monohydride exhibits a NIA of 0.63 after two hours, while the dihydride falls to 0.31 NIA. The trihydride retains 0.47 NIA while the total NIA for Si hydride species after two hours is 0.49 (Figure 2.10). A broadening of the hydride region with featurless hydride peaks occurs. No pH change is observed in this case, such that the concentration of OH^- in solution to etch the Si surface is unchanged from a normal UPW media. Since pH does not change with N_2 bubbling, it is plausible that the observed broadening is due to a physical phenomenon of interaction of the Si surface with N_2 bubbles whereby the preferential interaction with dihydride species is inhibited. This would lead to the random etching of the Si surface. Such an etching would cause the formation of

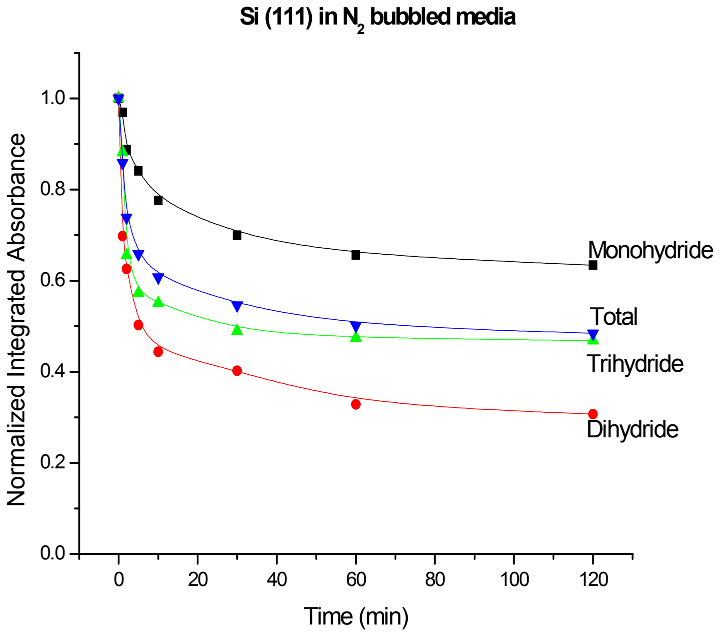

Figure 2.10 Normalized Integrated Absorbances of hydride regions of H-terminated Si (111) immersed in N_2 bubbled UPW.

multifacted Si-H structures, which in turn would give rise to broad, featureless hydride peaks. In comparison to normal UPW with appreciable DO content, Figure 2.11 shows minimal oxide formation over two hours of immersion time.

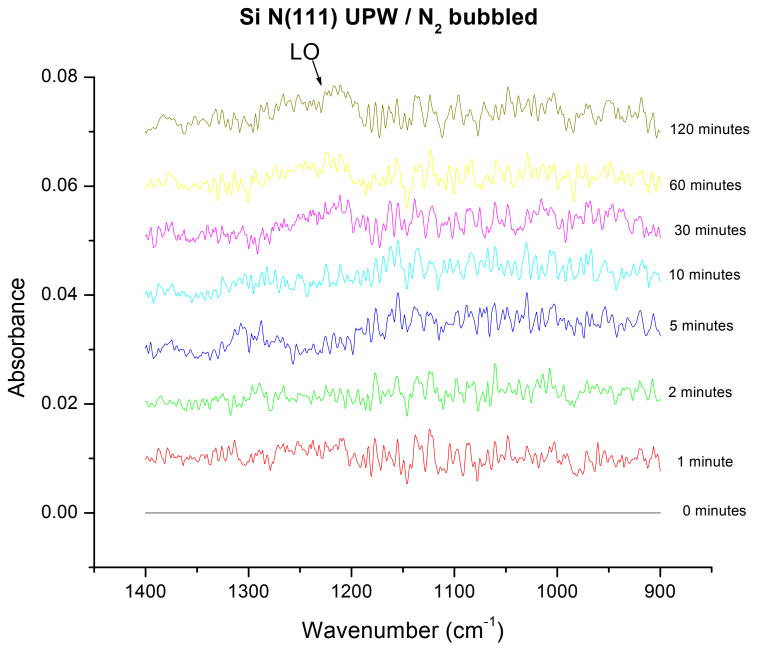

Figure 2.11 FTIR-ATR spectra of HF etched N-type Si (111) with immersion time N_2 bubbled UPW, Oxide Region.

2.3.4 Ideal Monohydride Terminated Si(111) in UPW

Ideal monohydride terminated surfaces, M', have been observed in previous literature[9,14-16,21]. Prepared ideally hydrogen terminated elements were also studied with immersion time in UPW in this work. These UPW experiments were run under different conditions with and without N_2. Immersion of monohydride terminated Si into various UPW water types for two hours shows an expected decrease in M' signal over time. Additionally, the shape and sharpness of the peak decreases significantly over two hours such that there is a great loss in peak intensity and a large amount of

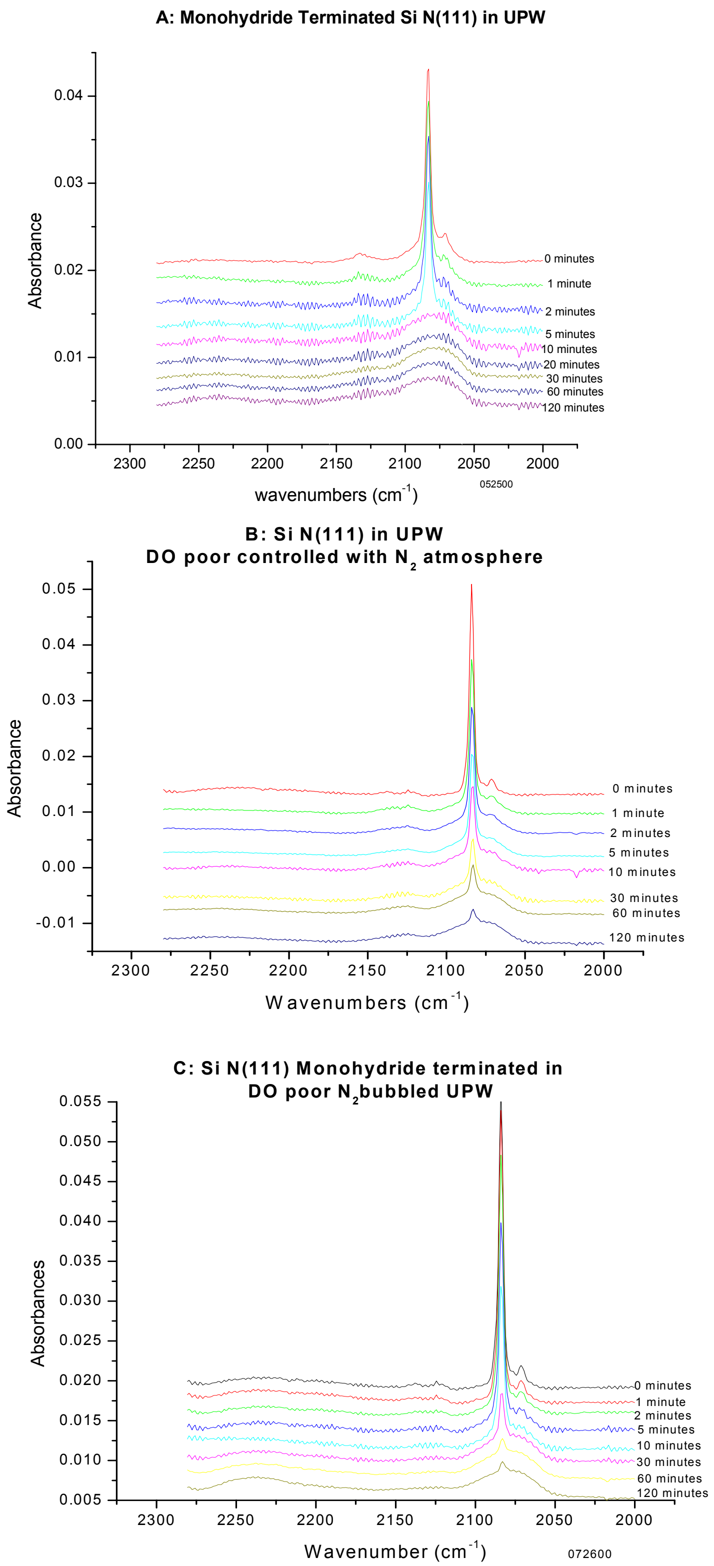

Figure 2.12 FTIR-ATR spectra of Monohydride Si(111) under various UPW conditions.

broadening over the whole hydride region as observed in Figure 2.12. For normal UPW media in an ambient environment the monohydride region still retains 0.71 NIA over two hours of immersion. The Si sample immersed in DO poor water controlled by N_2 atmosphere still retained 0.84 NIA, while the N_2 bubbled media retains a 0.72 NIA. Under N_2 bubbling and N_2 atmosphere controlled conditions, there is also a decrease in monohydride signal, but in the case of the N_2 ambient condition we see a very slight increase of trihydride signal (at ~2130 cm^{-1}) over two hours. This could be due to the lack of physical perturbation of N_2 gas and lack of DO allowing for etch sites on the Si surface to be reached. Figure 2.13 graphs the NIA for the loss of monohydride. There is negligible trihydride species still observed. This may be explained in Figure 2.14. Although the decrease in kinks

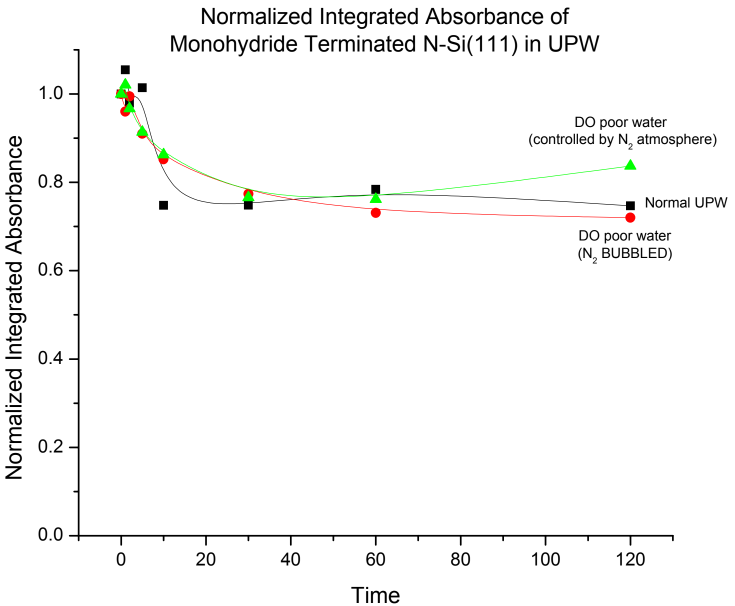

Figure 2.13 NIA of Monohydride Terminated N-Si(111) surfaces in UPW

and steps at which the trihydride species may exist, there are still those silicon species protruding from the Si(111) surface which may still have three hydrogens attached. The calculated contribution of trihydride species to the overall NIA is negligible (~1-2%) for the monohydride experiments. It is of interest to note, that although peak height decreases by a large margin (as seen in Figure 2.12.), the integrated area for the monohydride region remains substantially large yet across a broader range. This can be explained as the decrease in domain size through roughening of the surface. Although mostly monohydride in nature, the N-type Si(111) surface can be thought of as microscopically rougher surface, yet it is still hydrogen terminated. The N_2 bubbled UPW media shows that any negligible trihydride disappears quickly. It may be inferred in N_2 ambient UPW that monohydrides are etched and oxidized while a dynamic condition exists whereby the formation of some

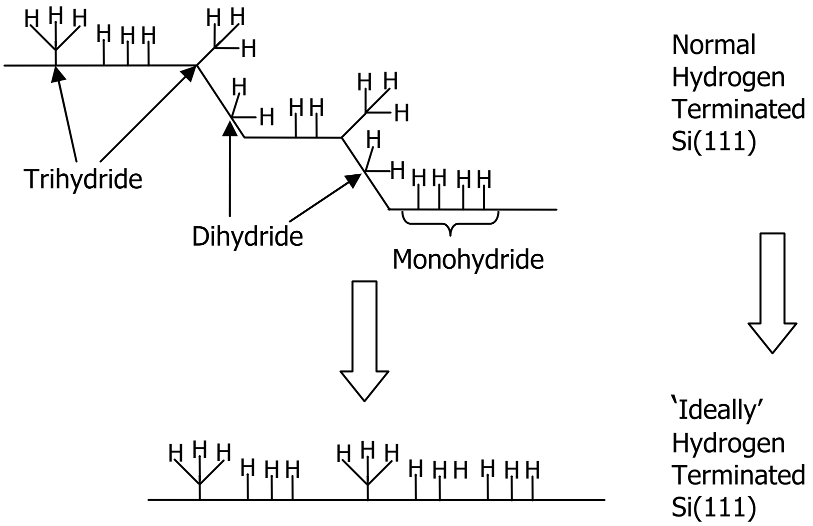

Figure 2.14 Rough vs. Smooth Si(111) hydrogen termination

trihydride species are formed leading to increased vibrational signal. In these cases, dihydride species may be formed, but as seen on microscopically rough Si (111) surfaces in UPW, it is the least stable of the hydride species and would be etched away almost immediately after formation. A monohydride terminated Si (111) surface seems to be the most stable under UPW conditions. There is only slight oxide formation observed after 120 minutes in the FTIR spectra for all cases of monohydride terminated Si (111) surfaces.

Polarization of the incoming radiation for the ideal monohydride FTIR experiments confirm the nature of the terminated surfaces. Figure 2.15 exhibits the spectra of the monohydride terminated Si surface when exposed to normal UPW.

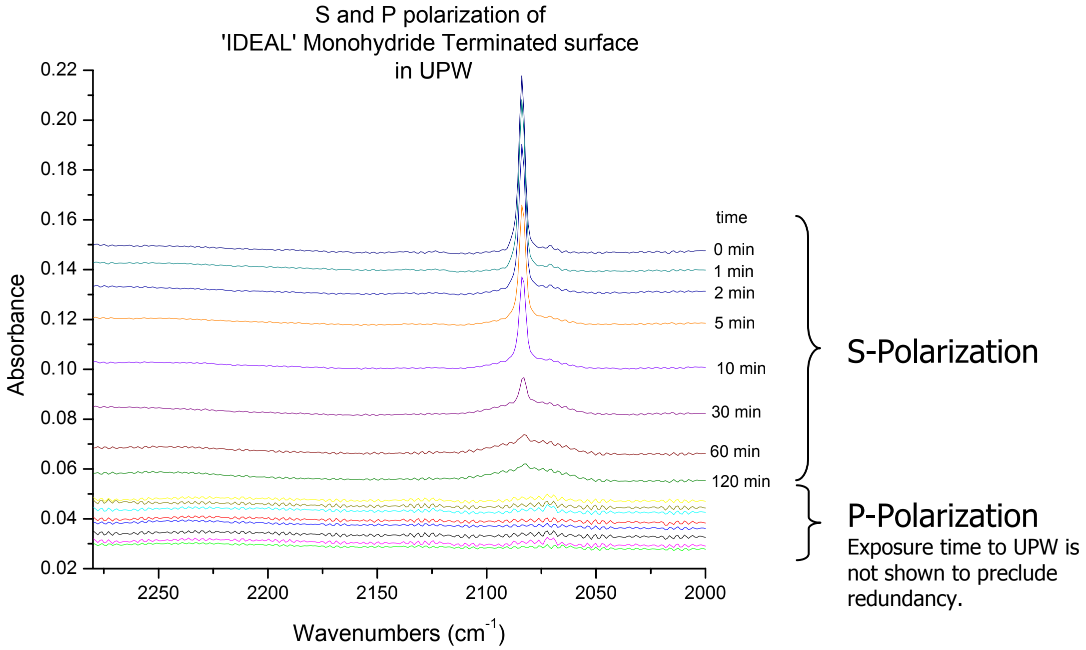

Exposure time to UPW is not shown to preclude redundancy.

FIGURE 2.15 S and P polarized FTIR-ATR spectra from Si(111) monohydride terminated

S polarized radiation is surface normal to the FTIR-ATR element, thereby enhancing the Si-H bonds that would be near to surface normal. Conversely P polarized radiation is parallel to the plane of the FTIR ATR element and would detect only those that Si-H bonds that are near-parallel to the surface. This invariably leads to the conclusion that the chemically modified surface to the is a near ideal mono hydride surface.

2.3.5 Trace Metal Contaminated UPW

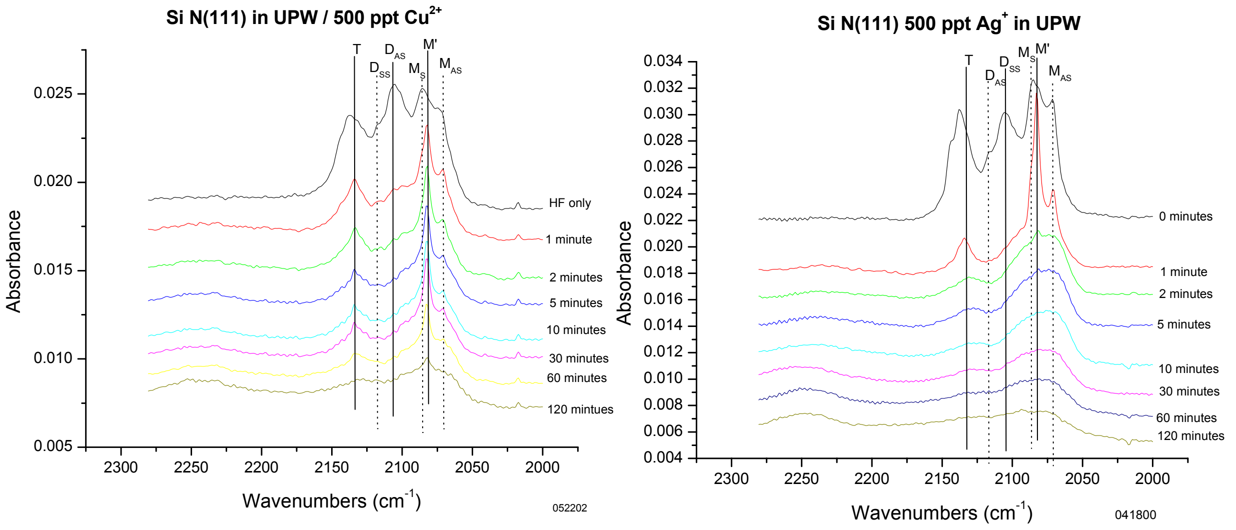

In comparison, the effect of metal contamination was also observed on microscopically rough surfaces. Silver and copper contamination was observed. The disappearance of hydride peaks proceeds similarly as seen in UPW media. A sharpening of the monohydride and trihydride with a swift disappearance of the dihydride peaks are observed in Figure 2.16. Figure 2.17 shows the NIA for 500 ppt Ag(I) and Cu(II) ions in UPW. The values for immersion in 500 ppt Cu^{2+} in UPW for the Si (111) substrates are: 0.40 NIA for monohydrides; 0.24 NIA for dihydrides; 0.30 NIA for trihydrides; and 0.32 NIA for the total decrease over two hours. The values for immersion in 500 ppt Ag^+ UPW are: 0.23 NIA for monohydride; 0.16 NIA for dihydride; 0.23 NIA for trihydride; 0.21 NIA for the total decrease over two hours. It is evident that the increase in metal contamination accelerates the disappearance of hydride species.

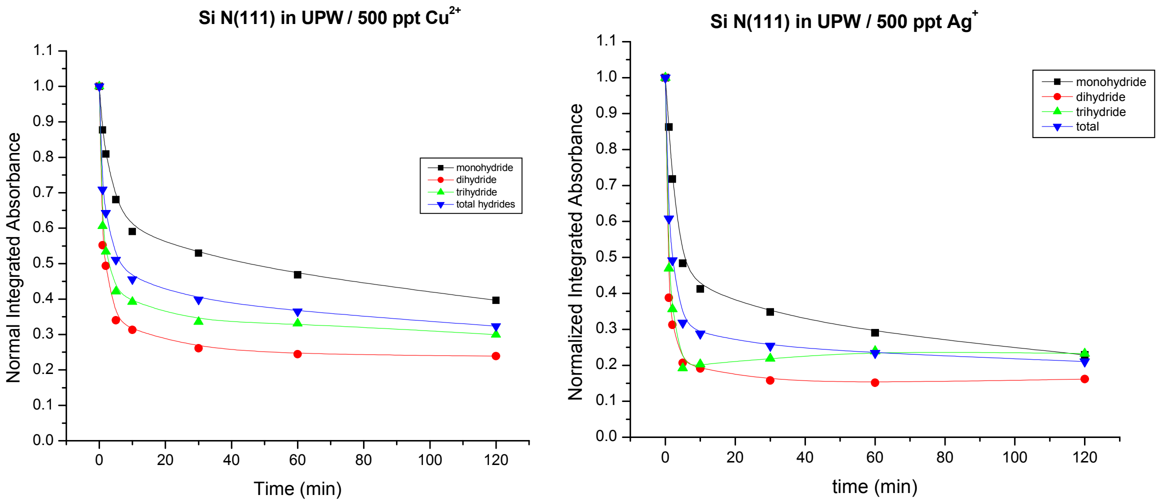

regions of H-terminated Si (111) in trace metal contaminated

This is thought to be due by metal induced oxidation of the passivated Si surface not to etching of the hydride surface. This behavior has been observed in this group's previous work[13,22]. Previous work[11,12] indicates that the stepped edges where dihydrides exist are sites where metal contamination is likely to occur at an accelerated rate. The deposition of noble metals on a hydride terminated Si substrate will result in the extraction of electrons from the Si substrate leading to subsequent oxidation. Oxide formation is substantially increased in the 120 minute time period with an increase in metal contamination as seen in Figure 2.18.

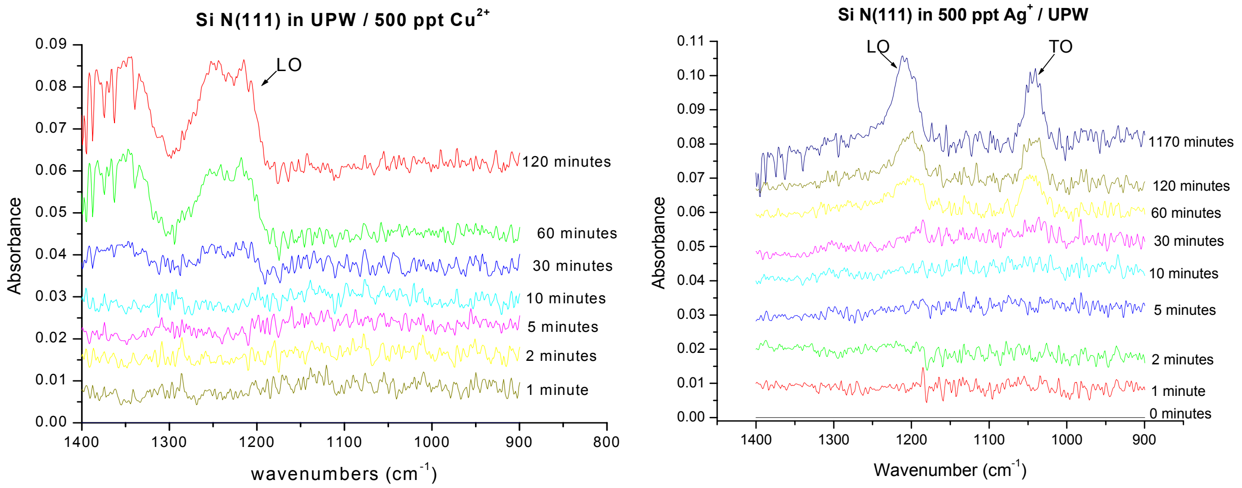

Figure 2.18 FTIR-ATR spectra of HF etched N-type Si (111) with egion.

The manner of disappearance of the hydrides is similar to those seen on a microscopically rough surface in UPW and corroborates the assertion that dihydride regions on UPW are the most unstable and prone to chemical interactions.

Preliminary studies with 500 ppt Cu^{2+} contamination in UPW with nitrogen bubbling and atmospheric control of dissolved oxygen show that there is little or no change in the normalized integrated absorbances for the amount hydride species lost when compared to normally contaminated UPW. Figure 2.19 show the spectra for two cases of Cu contaminated DO poor UPW.

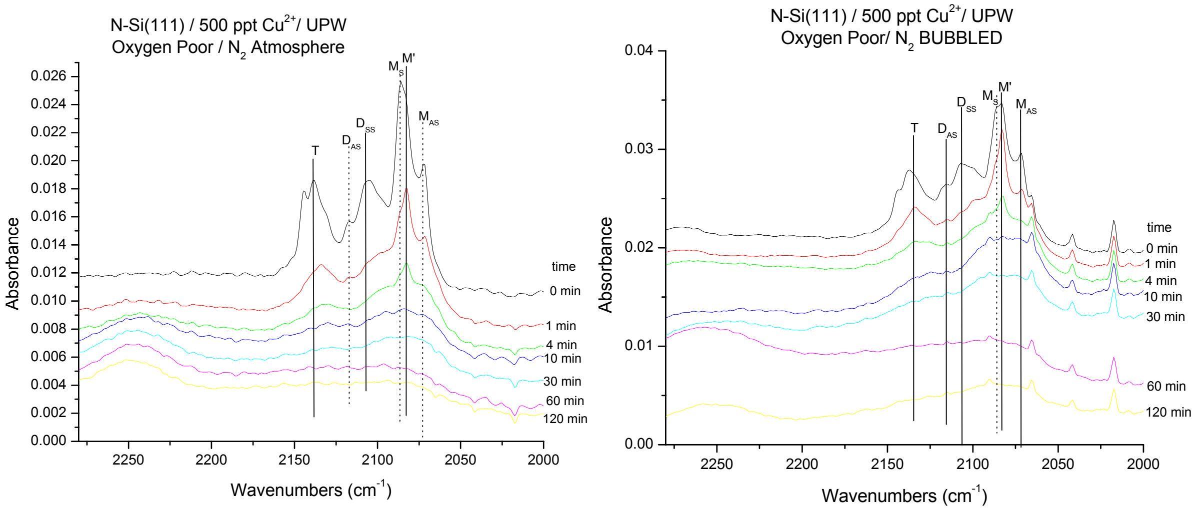

Figure 2.19 FTIR-ATR spectra of HF etched N-type Si (111) with immersion time in trace metal contaminated UPW-DO POOR conditions

It is of interest to note that due to the individual nature of the Si(111) wafers which are used, slight miscuts or variations in the chemical mechanical planarization of the surface during manufacturing preparation may induce certain regions to be more pronounced. This may be a plausible explanation to for the larger absorbances of the monohdyrdide region. Figure 2.20 records the change in NIA over time in immersion in DO poor UPW. Regardless of hydride absorbances, the NIA values indicate that there is little or no change versus normal UPW conditions. This is summarized in Table 2.1. It could be surmised that the oxidation of the Si(111) surface in metal contaminated UPW does not proceed through the same means that normal UPW oxidation of Si(111) occurs. This metal induced deposition and oxidation is discussed more thoroughly in Chapter 3.

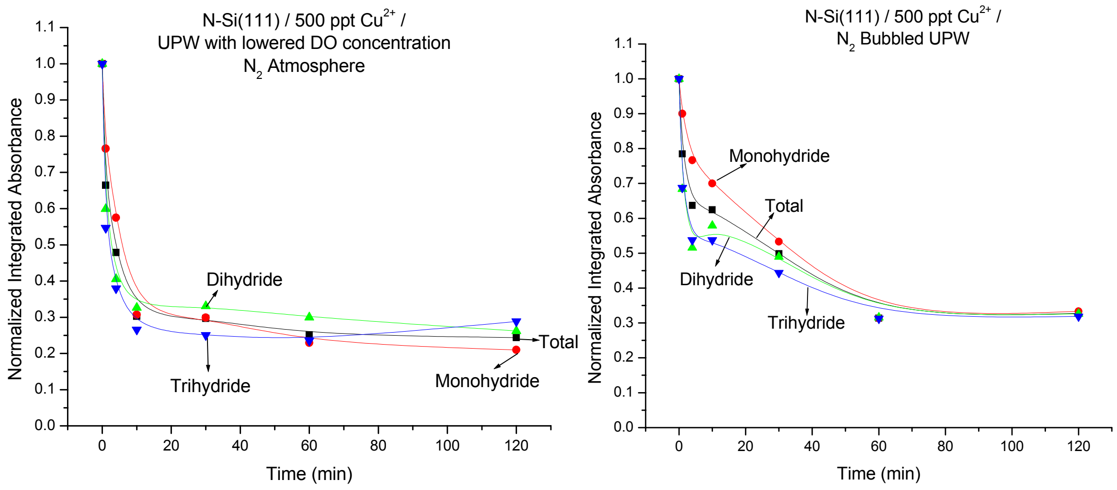

Figure 2.20 NIA of FTIR-ATR hydride regions from HF etched N-type Si (111) with immersion time in trace metal contaminated UPW-DO POOR

2.3.6 Possible mechanism for the Oxidation of Si(111)

Possible mechanisms for the observed oxidation behavior may be seen in Figure 2.21 where the hydroxylation of the hydrogen terminated Si leads to the formation of a silicon oxide backbond. Previously reported studies[2,3,5,17] of Si oxidation in H_2O show that OH groups polarize and destabilize Si-Si back bonds making chemical attack by polar H_2O molecules a reality (steps A,B & C.) This corresponds to the rise in backbonded oxide signal, which eventually leads to attack of the surface hydride from the destabilized Si-H. The final product gives rise to the Si oxide region and IR signals for the transverse optical (~1050 cm^{-1}) and longitudinal optical (~1200 cm^{-1}) modes of stretching.

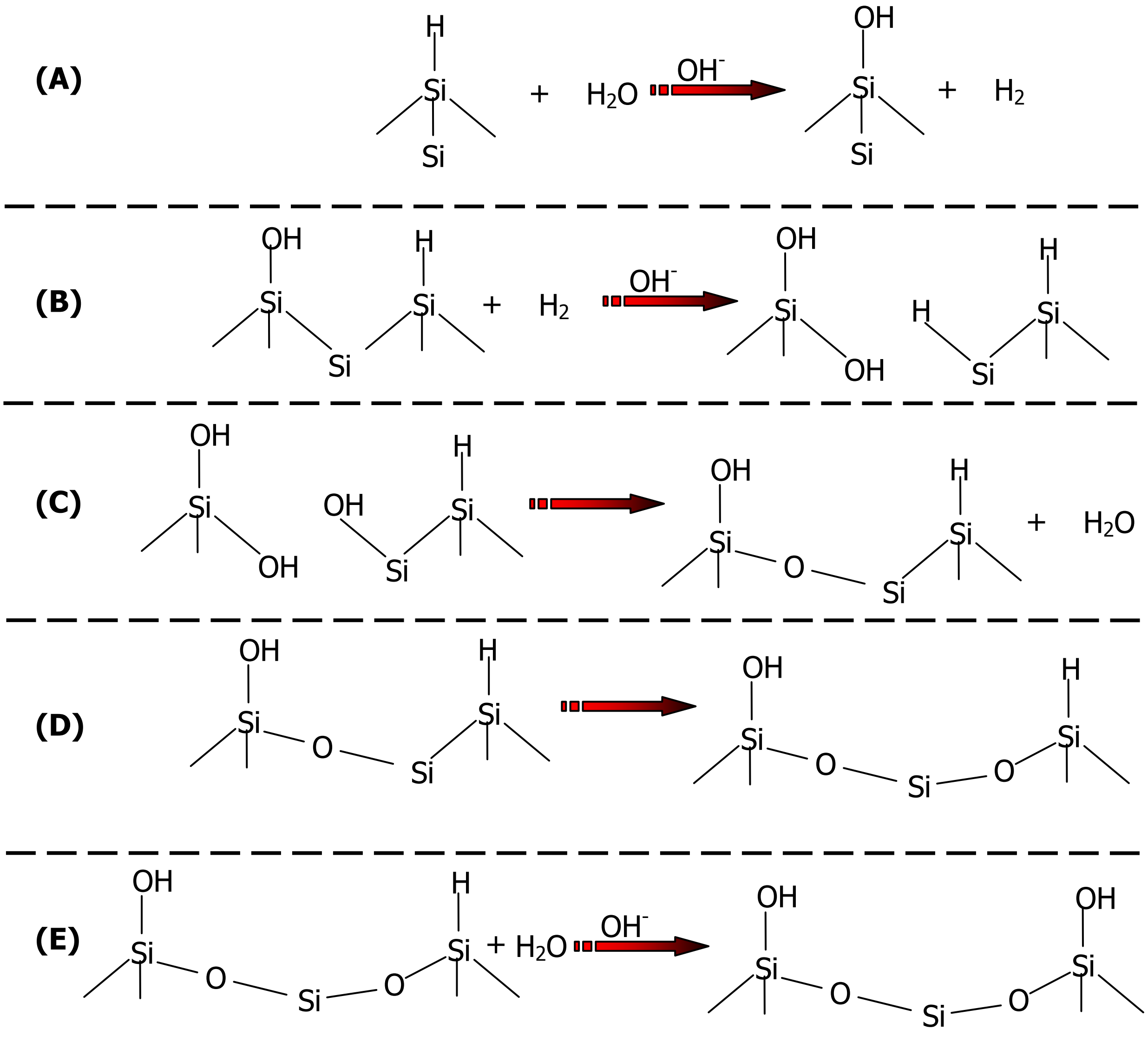

Figure 2.21 Possible mechanism for the oxidation Si surfaces in H_2O

2.4 Conclusion

Condition	**Region**	**NIA**
UPW	Monohydride	0.57
	Dihydride	0.13
	Trihydride	0.27
	TOTAL	**0.34**
UPW DO poor in Nitrogen Atmosphere	Monohydride	0.72
	Dihydride	0.21
	Trihydride	0.37
	TOTAL	**0.47**
UPW DO poor with Nitrogen Bubbling	Monohydride	0.63
	Dihydride	0.31
	Trihydride	0.47
	TOTAL	**0.49**
Monohydride in UPW	**Monohydride**	**0.71**
Monohydride in DO poor UPW In Nitrogen Atmosphere	**Monohydride**	**0.84**
Monohydride in DO poor UPW with Nitrogen Bubbling	**Monohydride**	**0.72**
500 ppt Cu Contaminated UPW	Monohydride	0.24
	Dihydride	0.24
	Trihydride	0.3
	TOTAL	**0.32**
500 ppt Cu Contaminated UPW in Nitrogen Atmosphere	Monohydride	0.21
	Dihydride	0.29
	Trihydride	0.26
	TOTAL	**0.24**
500 ppt Cu Contaminated UPW with Nitrogen Bubbling	Monohydride	0.33
	Dihydride	0.33
	Trihydride	0.32
	TOTAL	**0.33**
500 ppt Ag Contaminated UPW	Monohydride	0.23
	Dihydride	0.16
	Trihydride	0.23
	TOTAL	**0.21**

TABLE 2.1 Summary of Results

In conclusion, it has been demonstrated that different aspects of UPW rinsing of Si (111) surfaces have different effects on a hydrogen passivated surface. Metal contamination is seen to increase the rate of loss for hydrogen passivation on a Si surface, by allowing a more effective rate of electron transfer from the bulk Si to the surface, eventually leading to oxidation of the Si substrate. Dissolved oxygen in ultra-pure water plays a role on the etching and subsequent oxidation of microscopically rough and monohydride terminated Si surfaces by: i) allowing for a more amenable arrangement for the etching of the hydride surface by water, and ii) being present in the insertion of backbonded surface oxides. It is also seen that bubbled nitrogen seems to play a physical role by perturbation of the water molecules such that preferential etching of dihydride sites is prevented. Table 2.1 summarizes the results as seen in this study.

2.5 References

(1) Sze, S. M., Ed. *VLSI Technology*; McGraw Hill: New York, 1988.

(2) Boonekamp, E. P.; Kelly, J. J. *Journal of Applied Physics* **1994**, *75*, 8121.

(3) Gräf, D.; Grundner, M.; Schulz, R. *Journal of Vacuum Science and Technology A* **1989**, *7*, 808.

(4) Morita, M.; Ohmi, T.; Hasegawa, E.; Kawakami, M.; Suma, K. *Applied Physics Letters* **1989**, *56*, 562.

(5) Niwano, M.; Terashi, M.; Shinohara, M.; Shoji, D.; Miayamoto, N. *Surface Science* **1998**, *401*, 364.

(6) Peitch, G. J.; Köhler, U.; Henzler, M. *Chemical Physics Letters* **1992**, *197*, 346.

(7) Sasaki, Y. C.; Mitsuya, M. *Langmuir* **1995**, *11*, 3446.

(8) Watanabe, S.; Shigeno, M.; Noriaki, N.; Ito, T. *Japanese Journal of Applied Physics* **1991**, *30*, 3575.

(9) Usuda, K.; Yamada, K. *Applied Surface Science* **1999**, *143*, 16.

(10) Lim, S. W.; Mo, R. T.; Pianetta, P. A.; Chidsey, C. E. D. *Journal of The Electrochemical Society* **2001**, *148*, C16.

(11) Homma, T.; Wade, C. P.; Chidsey, C. E. D. *The Journal of Physical Chemistry B* **1998**, *102*, 7919.

(12) Chyan, O. M. R.; Chen, J.-J.; Chien, H.-Y.; Wu, J. J.; Lie, M. *Journal of The Electrochemical Society* **1996**, *143*, L235.

(13) Chang, R. *Chemistry*; Fourth ed.; McGraw-Hill: New York, 1991.

(14) Higashi, G. S.; Chabal, Y. J.; Trucks, G. W.; Raghavachari, K. *Applied Physics Letters* **1990**, *56*, 656.

(15) Yang, S.-K.; Peter, S.; Takoudis, C. G. *Journal of Applied Physics* **1994**, *76*, 4107.

(16) Watanabe, S.; Sugita, Y. *Surface Science* **1995**, *327*, 1.

CHAPTER 3

INVESTIGATION OF SI BASED POTENTIOMETRIC SENSORS IN ULTRA-PURE WATER WITH TRACE METALLIC CONTAMINANTS

3.1 Introduction

High purity water is an essential chemical used by many high tech industries such as the pharmaceutical and microelectronics. In the latter, various high purity water, acids and bases are seen used to achieve ultra-clean Si wafer surfaces[1,2] for the fabrication of Very Large Scale Integrated (VLSI) Si devices, such as the digital signal processor (DSP) chips found in today's cellular phones. Ultra-pure water (UPW) must be used in the manufacture of present day pharmaceuticals to ensure proper dosage and effectiveness of medications which millions of people ingest daily[3]. The use of UPW for various manufacturing activities (for example: silver chemicals in photography processing,) also ensures that today's chemical wastes do not become a concern for future generations. With the aforesaid concerns, it is evident to see the importance for the use of UPW.

Si surfaces have the natural tendency to grow stable oxide which can be hydrogen passivated by chemical treatment of HF. Studies have been conducted observing Silicon (Si) wafer interaction with metallic impurities in water. Chyan et al. have also formulated a potentiometric sensor for the detection of metallic impurities in HF[Chyan, 1996 #4; Chyan, 1997 #3; Chyan, 1997 #6; Chyan, 2000 #5]. HF etching and alkaline cleaning solutions (RCA cleaning steps) are most commonly used to prepare ultra-clean Si wafer surfaces for later fabrication into IC devices.

Developed as a practical sensor for the on-line monitoring of ultratrace (parts per-billion –ppb/ parts per-trillion –ppt) level metallic ion contaminants, Chyan's sensor is able to respond selectively only to those contaminants which react to Si wafer surfaces. This is possible due to the fact that the sensing element is a Si-based sensing electrode which is used to directly monitor the HF etch. Metal ion impurities such as Au^{3+}, Ag^{+}, Cu^{2+}, Pd^{2+} and Pt^{2+} are known to readily reduce and deposit as zero-valence nanoparticles on oxide-free Si surfaces[4,5]. Ultra trace concentrations of nanoparticle deposition can cause a positive shift in the open-circuit potential (OCP) value of the Si based electrode leading to the premise of Si potentiometric sensing. Direct OCP measurements of the Si based potentiometric sensor in HF solutions as well as alkaline hydrogen peroxide solutions have been used to obtain direct relationships between the OCP measurements and amount of metallic contaminants in solution.

This chapter deals with the use of the Si potentiometric sensor for detection of trace metal contaminants in ultra-pure water. While the detection of trace metal contaminants in UPW has been previously studied, it must be noted that those studies were accomplished in with the use of dilute HF acid solutions while the study presented in this chapter deals with direct sensing of ppt/ppb level contaminants directly in UPW solutions. The deletion of HF acid solutions to the sensing protocol is a considerable advantage since the use of HF acid carries serious safety issues. Without the use of HF it is possible to realize the use of the Si based potentiometric sensor for direct on-line sensing of metallic impurities in flow streams where stringent quality control of water supplies must be maintained.

Fourier transform infrared spectroscopy (FTIR) coupled with attenuated total reflection (ATR) techniques were also used to observe the decrease in passivation of Si through the vibrational spectra of the hydride regions in the initial stages of metal induced etching and oxidation of the Si (111) surface.

3.2 Experimental

N-type (111) Si single crystal substrates (Polishing Corporation of America, 430 Martin Ave. Santa Clara, CA 95050. http://www.pcaSi.com/ - PCA#7493,) were used as sensing elements for the potentiometric experiments. Previous studies of Si based potentiometric sensors were accomplished using an all polyfluoroalkoxy (PFA) body sensor holder with double Teflon® coated Viton® O-rings as seen in Figure 3.1(A). This configuration allowed solution contact with only the front polished surface of the Si substrate. Ohmic contact was made to the backside of the Si substrate with Ga/In eutectic (99.99%, Alfa Aesar, a Johnson Matthey company, Alfa Aesar, 30 Bond Street, Ward Hill, MA 01835, http://www.alfa.com/). While this configuration is well suited to single side polished Si substrates, it is unwieldy, labor intensive and time consuming to prepare. It was found that for double sided polished wafers, a modified alligator clip, illustrated in Figure 3.1 (B), assembly allowed for clean, simple use of the Si substrate for a sensing electrode. It must be noted, that extreme care must be taken when handling the double polished Si so that the region which comes in contact with solution maintains its ultra-clean surface.

All Si substrates for this study were cleaned in hot solutions of SC1 (standard clean - 1; 1:1:5; H_2O_2:NH_4OH:H_2O) and SC2 (standard clean - 2;

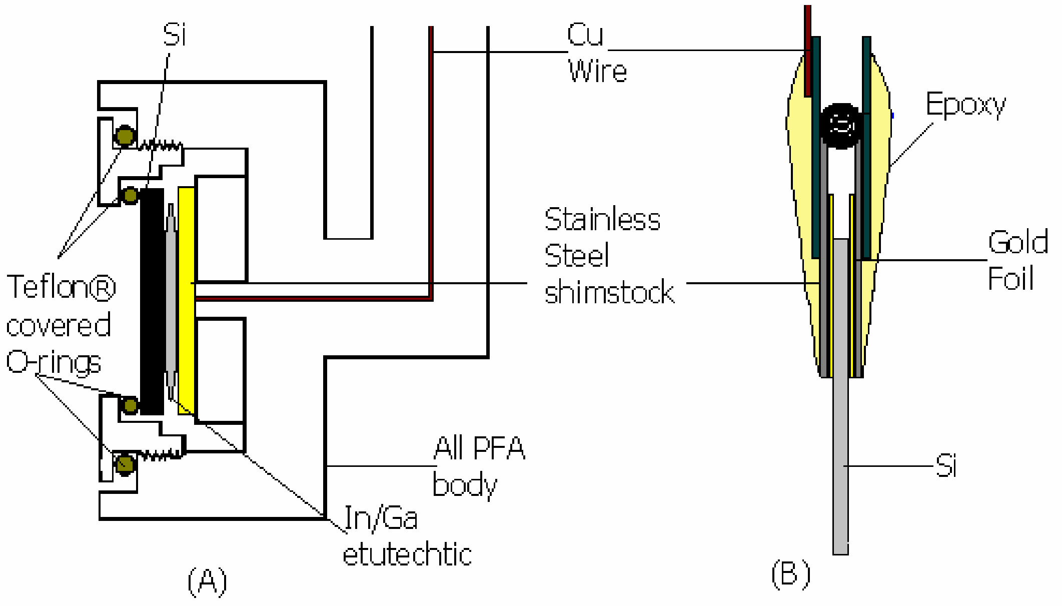

Figure 3.1 Illustration of (A) Custom made PFA electrode body (B) Modified alligator clip assembly

1:1:5; H_2O_2:HCl:H_2O) for 10 minutes. Each hot cleaning step is followed by an etching step in 4.9% hydrofluoric acid (HF) and rinsed with UPW. Si FTIR-ATR elements were prepared using the procedure outlined in Chapter 2 of grinding and polishing the beveled face of the Si crystals. Si FTIR-ATR measurements were obtained using the same equipment and parameters as described in Chapter 2.

Open-circuit potential measurements of Si substrates were measured against a standard Model 90-02 Double Junction Ag/AgCl reference electrode (Orion Research Inc. Cummings Cente, Beverly, MA 01915, http://www.orionres.com/). Before each experiment, the reference electrode was rinsed and the outer junction solution (10% KNO_3) was replenished. Measurements were read with a computer interfaced high impedance Accumet® 50 potentiometer (Fisher Scientific, Atlanta, 3970 Johns Creek Court, Suite 500, Suwanee, GA 30024. http://www.fishersci.com/.) Sensing experiments were run in normal room lighting conditions. It must be mentioned that standard double junction Ag/AgCl reference electrodes will leak their inner/outer solutions over time. Dr. Thomas Ponnuswamy et al. have studied new possibilities for new quasi-reference electrodes using Si based and chemical vapor deposition (CVD) diamond films[6] and may provide answers for long time duration chemical sensing.

Clean UPW solutions were spiked with known quantities of metallic contaminants. Ag contaminate solutions were prepared from serial dilutions in UPW of high purity Silver ICP/DCP standard solution stock (Aldrich Chemical Company, Sigma-Aldrich Corporation, St. Louis, MO http://www.sigmaaldrich.com/). Cu contaminate solutions were prepared from serial dilution in UPW of high purity Copper Spectrometric Solution (National Institute of Standards and Technology, Gaithersburg, MD http://www.nist.gov/).

Experiments were accomplished using PFA labware which were cleaned by multiple boilings and sonications in 10% HNO_3 and rinsed with ultrapure water. Ultrapure water (UPW) was supplied in-house via a Millipore Milli-Q® Elix 5® ultrapure water (Millipore Corporation, Bedford, MA, http://www.millipore.com/) purification system (R>18.2 MΩ/cm) and used in rinsing and immersion of Si substates as well as any dilution of chemicals.

3.3 Results and Discussions

Investigation of the potentiometric responses of the Si based sensing electrode show a positive shift of the OCP as the concentration of metallic contaminants were increased. All Si electrodes were pre-etched in 0.49% HF for 10 minutes to remove any native surface oxides followed by an UPW water rinse. A stable baseline potential in non-contaminated UPW was first established for 20 minutes before being subjected to metallic ion contaminated UPW solutions.

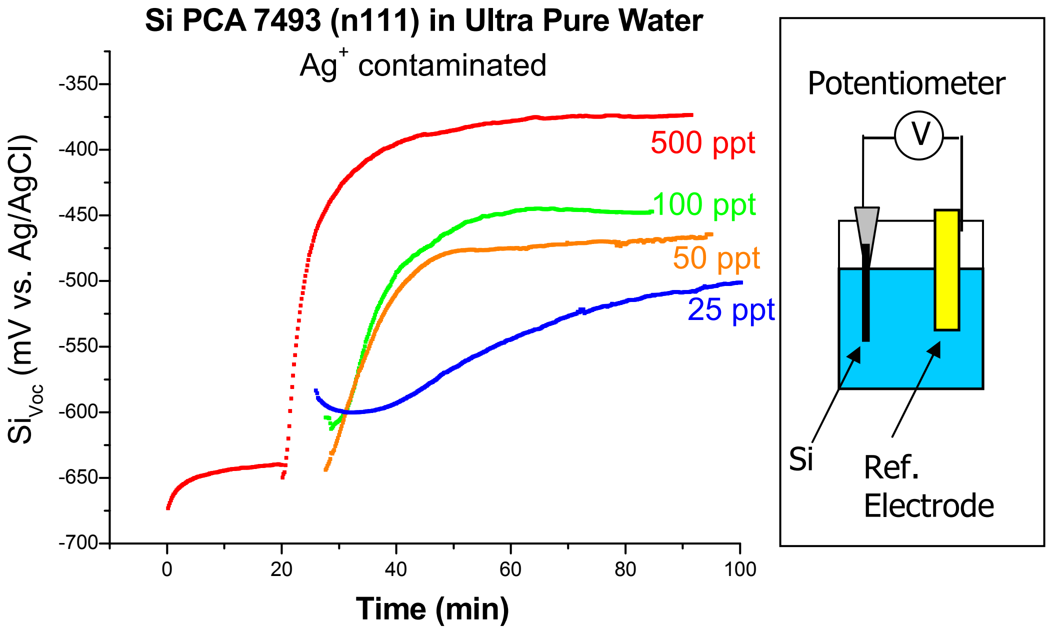

Figure 3.2 Time dependent potentiometric response of (111) N-type Si based sensor in ultra-pure H_2O and Ag$^+$ (setup in inset)

Figure 3.2 illustrates the positive shift in OCP as the concentration of Ag$^+$ contaminants increases. It is interesting to note that even in the lower parts-per-trillion range of contaminants (25 ppt [Ag$^+$]) there is as much as a +140 mV shift in the OCP. A schematic depicting the OCP setup is inset on Figure 3.2.

The most noteworthy feature of this experiment is the fact that parts-per trillion level metallic contaminants may be directly detected with the simple measurement of open-circuit potential. This ultra-trace level detection sensitivity range is required by the microelectronic fabrication applications, especially as features become smaller and smaller.

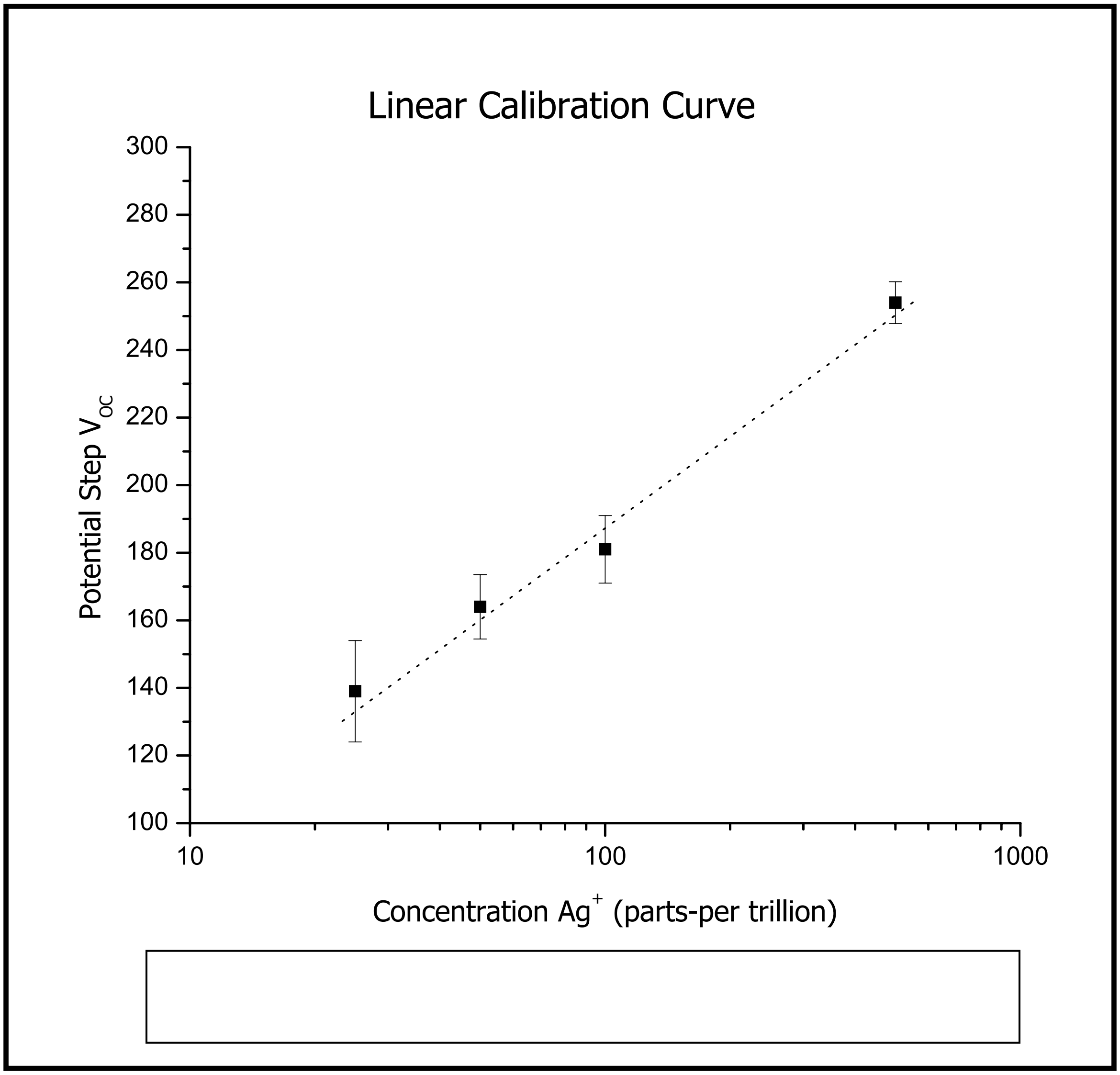

A linear calibration curve of the log of Ag^+ concentration versus the shift in Si open-circuit potential (V_{OC}) is shown in Figure 3.3. The sensitivity of this method is much more than that of a common electrochemical sensor which relies solely on Nernstian equilibrium at the analyte/sensor interface. The Nernst equation dictates that there should be a 59 mV change per decade of concentration change at room temperature as seen by:

$$E = E^{o} - \frac{0.0591}{n} \log \frac{[M_{red}]}{[M_{ox}]}$$

for the general system:

$$M_{ox}^{n+} + ne^{-} \rightarrow M_{red}$$

where E is the changed potential of a system, E^{o} is the standard reduction potential, n is the number of electrons involved in electron transfer and the number 0.0591 is the constant of (2.303RT/F) with ‘R’ being the gas constant, ‘T’ being temperature, and ‘F’ as Faraday’s constant (96500 coulombs/mole).

Initial studies done with Cu in UPW show a similar trend and confirm the behavior of the Si based potentiometric electrode with other metallic ions as seen in Figure 3.4. Cu is important because of its application as interconnect materials in the microelectronics industry. With Cu interconnect materials being an integral part of today’s new generation of IC devices, any Cu contamination during the rinsing process in the preparation of Si could lead to catastrophic device breakdown.

Previous studies done of Si based potentiometric sensing by Chyan et al. in HF solutions also show a detection sensitivity greater than the 59 mV per decade change of $[Ag^{+}]$. One possibility could be due to the fact that metal

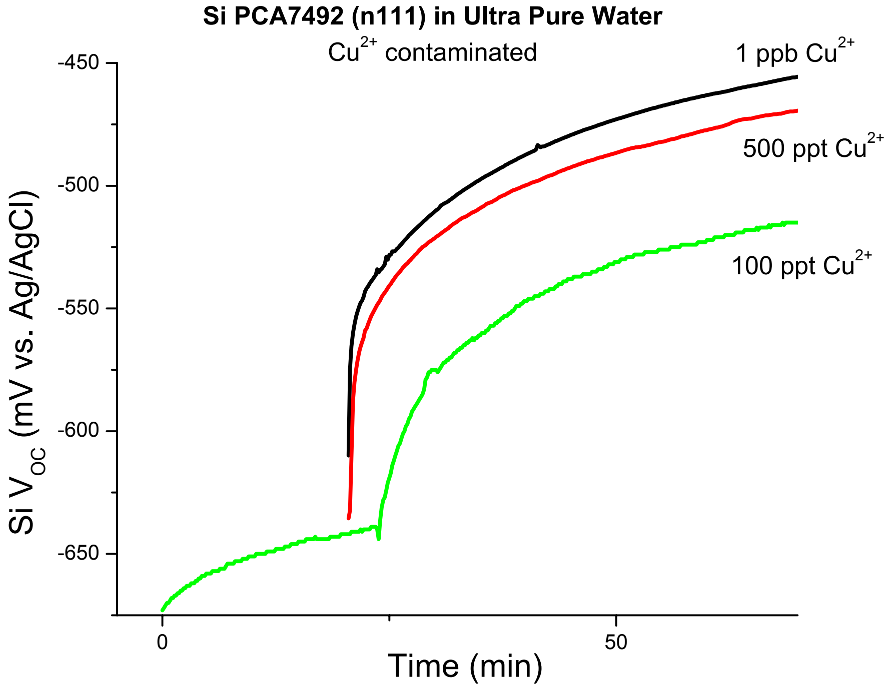

Figure 3.4 Time dependent potentiometric response of (111) N-type Si based sensor in ultra-pure H_2O with Cu^{2+}

deposition is seen as hole injection[7] of the strongly oxidizing Ag^+ ions into the valence band of Si which to drain electrons near the surface of Si. Illustrated in Figure 3.5, hole injection of metallic ions (M^{n+}) into the surface space charge region of Si causes the Si to to undergo oxidation. This drain of electrons at the surface space-charge region shifts the OCP more positive and allows for detection of metallic contaminants.

This oxidative etching scheme of Si is governed by the Gibb's equation which states:

$$\Delta G=-nFE^{o}$$

where n is the number of electrons transferred during metal deposition. As a result, a more negative ΔG leads to an increase in spontaneity – meaning that the deposition is more thermodynamically favorable. Thus the redox potentials listed in Figure 3.5 show

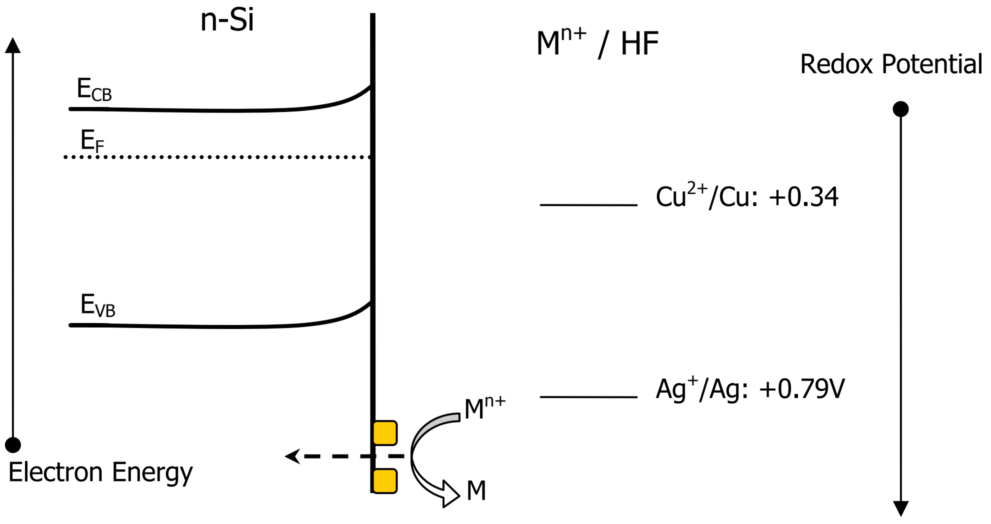

Figure 3.5 Spontaneous deposition of metals on Si surface

that Ag deposition is more favorable to occur. Since potential is the amount of work required to move an electron from an infinite point in space to a point of interest, in this case, a working Si electrode surface. More positive or less negative potentials are reached by increasing positive excess charge or decreasing electron energies. In the case in HF, it may be surmised that hole injection of metallic contaminants lead to the electroless deposition of metal nanoparticles on the Si surface, but before any oxidation can take place, HF etching of any Si oxide ensures a hydrogen terminated passivated surface for more hole injection by metal contaminants as illustrated in Figure 3.6 (A). As metal particles form on the surface, a metal-semiconductor interface is formed. This interface allows for Schottky function which decreases the energy required for an electron to escape the surface of the interface. This is also a reason for the supernernstian behavior which is seen. As the Si oxide is etched during the spontaneous deposition of metals, pits and other roughening features are formed. This has been previously observed with atomic force microscopy (AFM) [7].

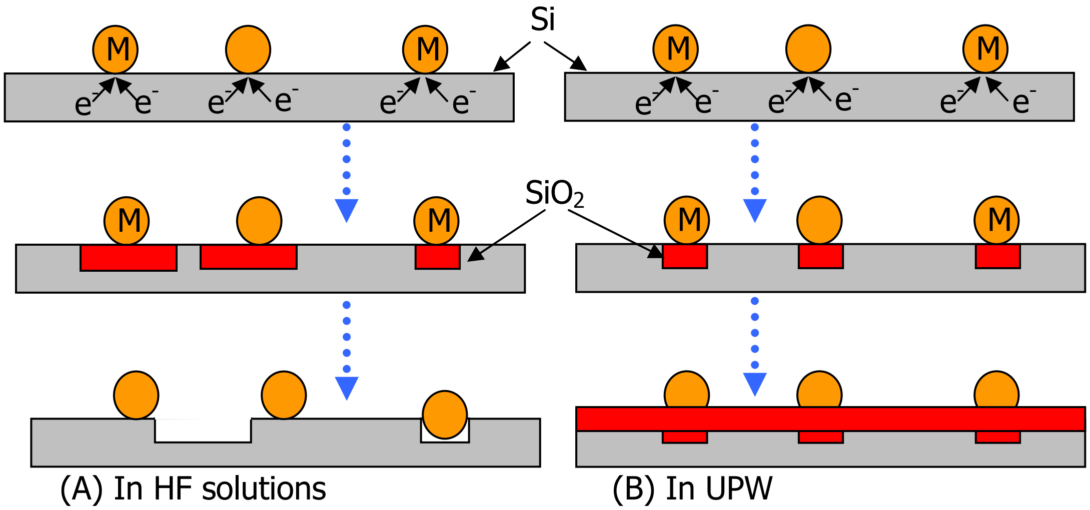

(A) In HF solutions

(B) In UPW

Figure 3.6 Illustration of the metal deposition and induced oxidation

Under UPW conditions, the extraction of surface electrons from the Si surface results in the metal induced oxidation of the surface since there is no HF to etch the formed oxide. This leads to an increase in Si oxide thickness which is translated into a further change in the OCP. Such a reaction illustrated in Figure 3.6 (B) may be:

$$Si\text{-}H_x + M^{n+} + H_2O \rightarrow SiO_2 + M + xH^+$$

Hole injection and other processes taking place at the solution/surface junction such as metal deposition by valence electron extraction, metal-induced Si surface corrosion, or other electron transfers may cause a drain of electrons from the Si surface.

Measurements with Fourier transform infrared spectroscopy (FTIR) coupled with attenuated total reflection (ATR) technique as reported in Chapter 2, show that metal ions show an affinity to the dihydride step edges of a microscopically rough Si n-type (111) surface for the transfer of electrons for the oxidation of metallic ions to solid metal nanoparticles. This is followed by a decrease in trihydride intensity over time, with a robust existence of monohydride termination. Thus a qualitative observation can be made into the favorability or stability of active sites on a microscopically rough n-type Si (111) surface as:

Monohydride>Trihydride>Dihydride.

3.4 Conclusion

Ultra-pure water plays an important role in many of today's industries. The sensing of trace level contaminants leads to better quality assurance and quality control of end-user products – and in the case of pharmaceuticals, a better quality of life. This chapter has illustrated a further use of the novel Si based potentiometric sensor without the need for HF acid media. The reason for this phenomenon may be postulated in the uptake of CO_2 by water from the atmosphere. It is known[3] that even after a few minutes, CO_2 uptake may change the pH of a solution by several pH points. This change in pH from an ideal pH of 7 may provide the appropriate change in the UPW for reduction/oxidation processes to take place. This makes the sensor much safer for use. It also provides an in-stream alternative for detecting trace metal impurities of UPW supplies before inclusion into industrial processes. Although the Si based potentiometric sensor cannot detect individual elements, it may be argued that this sensor is to be used as a tool to monitor overall quality of UPW.

3.5 References

(1) Verhaverbeke, S.; Messoussi, R.; Morinaga, H.; Ohmi, T. In *Ultraclean Semiconductor Processing Technology and Surface Chemical Cleaning and Passivation*; Liehr, M., Heyns, M., Hirose, M., Parks, H., Eds.; Materials Research Society: Pittsburgh, 1995; Vol. 386, p 3.

(2) Kniffin, M. L.; Beerling, T. E.; Helms, C. R. *Journal of The Electrochemical Society* **1992**, *139*, 1195.

(3) In *Filtration Industry Analyst*, 2003; Vol. 2003, p 14.

(4) Ohmi, T.; Imaoka, T.; Sugiyama, I.; Kesuka, T. *Journal of The Electrochemical Society* **1992**, *139*, 3317.

(5) Rotondaro, A. L. P.; Hurd, T. W.; Schmidt, H. F.; Teerlinck, I.; Heyns, M. M.; Claeys, C. In *Ultraclean Semiconductor Processing Technology and Surface Chemical Cleaning and Passivation*; Lieh, M., Heyns, M., Hirose, M., Parks, H., Eds.; Materials Research Society: Pittsburgh, 1995; Vol. 386, p 183.

(6) Ponnuswamy, T.; Chen, J.-J.; Fei, X.; Chyan, O. *Analyst* **2001**, *126*, 877.

(7) Morrison, S. R. *Journal of Applied Physics* **1982**, *53*, 1233.

CHAPTER 4

ELECTROLESSLY DEPOSITED PLATINUM AND PALLADIUM NANOPARTICS ON PYROLYZED PHOTORESIST FILMS

4.1 Introduction

Carbon is used extensively in various forms as an electrode surface providing a plausible intermediary for studying a wide range of electrochemical systems[1-6]. Thermal stability, resistance to electrochemical and chemical attack and good conductivity make carbon a material of choice. Carbon materials have been examined from the pyrolysis of gases[5], sublimed and sputtered carbon[2,4] as well as pyrolyzed photoresists and organic films. Recent studies have illustrated the properties of pyrolyzed photoresist films (PPFs) for use in microelectromechanical systems (MEMS) and carbon electrode materials[3,6-9].

Pyrolysis of organic materials follow three general stages of structural change[8]. Pyrolysis is accomplished in an inert atmosphere under high temperatures. During the precarbonization stage from room temperature up to 300 ^{o}C, the photoresist material turns black in color accompanied by a rapid weight loss due to evaporation of solvent. All 'loose' molecules of excess solvent are removed at this stage. The carbonization regime follows in the temperature region between 300 and 500 ^{o}C where oxygen, nitrogen, chlorine and other excess 'loose' atoms and molecules are thermally removed. The size of conjugated carbon systems gets longer. The time needed for this process is greater than that of the first stage, due to the increasing difficulty in removing molecules while building up a polymeric network with increasing cross linked chains. Containing about one hydrogen for every two carbons, a loose network of linear conjugated systems, which are still electronically isolated from one another, is the end result of this stage. The next temperature regime between 500 and 1200 ^{o}C results in the gradual elimination of hydrogen atoms from the network of carbon polymeric chains. At this juncture the electrical conductivity increases rapidly as the polymeric chains become an interconnected conducting network. Density and hardness of the carbonaceous material also increases.

Uniformly coated photoresists provide a reliable source of carbon as well as having the advantage of being patterned by modern photolithography techniques. Previous research demonstrates the structural roles of PPF surfaces yet the present knowledge base on the effects of metal nanoparticle depositions on PPF is limited.

Photoresist is used by the microelectronics industry for the photolithography of a circuit design concept to an actual imprinted pattern on a Si wafer. Photolithography is the process of transferring a circuit design (essentially a geometric pattern) on a mask to the surface of a Si wafer[10]. The general steps in the photolithography include wafer cleaning, barrier layer formation, photoresist application, soft baking, mask alignment, exposure and development, and hard-baking. After cleaning, a barrier layer (usually Si oxide) is grown on the Si surface. Using high speed centrifugal forces, or

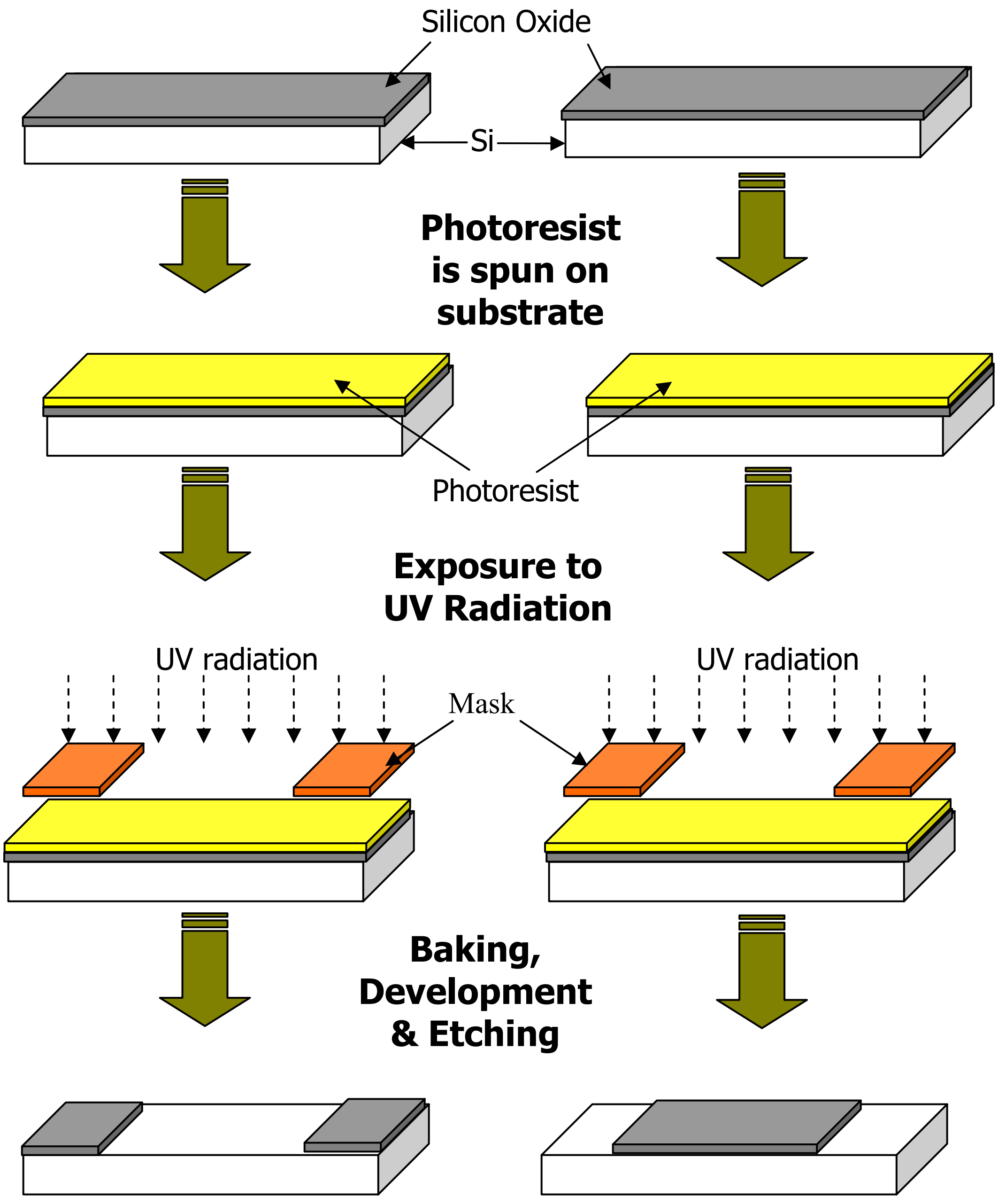

(A) Negative resist **(B) Positive resist**

Figure 4.1 General Illustration of Photoresist use for (A) negative photoresist and (B) positive photoresist spinning, a layer of photoresist is placed on the Si surface. Photoresist has three key components. A resin which has the property to withstand an etch solution makes up the majority of the photoresist composition. A sensitizer is used so that the resin will be light sensitive. Lastly, an adhesion promoter is added so that the organic photoresist will have the proper adhesion to the Si substrate surface. A mask with the proper pattern is placed over the spun-photoresist and exposed to UV radiation. After proper development (ie soft baking, etching and hard baking,) what is left is a patterned Si substrate ready for further processing. Figure 4.1 shows an illustration of the photolithography process for a negative and a positive photoresist. Negative photoresists become polymerized under UV radiation and are therefore difficult to dissolve. While positive photoresists are prone to chemical changes under UV radiation that make the resist becomes more soluble for further development.

Deposition of platinum and palladium metals on various carbon surfaces have been explored as a means for active catalysis in gas phase, liquid phase and electrochemical systems[11-16]. There is a wide variety of preparation techniques for metal nanoparticles. A variety of means for metal deposition [11-20] on carbon substrates have been studied and characterized. PPF on Si offers an advantage for spontaneous metal deposition onto the PPF surface. This chapter's study takes advantage of this unique behavior to electrolessly deposit metal nanoparticles on uniform carbon films formed by pyrolysis of photoresists. Electroless metal deposition of platinum and palladium nanoparticles on pyrolytically formed carbon films on Si substrates are observed. It is observed that nanometer-sized metal particles of platinum and palladium can be spontaneously deposited on conductive carbon films by immersion in solutions of varying HF containing varying parts per million concentrations of metal ions Pt^{2+} or Pd^{2+}. Surface morphology and distribution of metal nanoparticles on the PPF surface based on metal ion and acid concentration and deposition time were examined using scanning electron microscopy and energy-dispersive x-ray analysis. X-ray diffraction spectroscopy was also used to observe metal particle composition. Electrochemical behavior of the metal-deposited carbon films were investigated in 0.1 M H_2SO_4, $Ru(NH_3)_6^{3+}$, dopamine, and formaldeyde electrolyte systems. The electron-transfer rates and characteristics of hydrogen evolution in acidic media exhibit positive catalytic effects when the platinum and palladium nanoparticles were deposited on the carbon films. Platinum and palladium nanoparticles also exhibit catalytic effects for the redox couples, $Ru(NH_3)_6$ and dopamine, as well as catalysis of formaldehyde. This Chapter's study demonstrates a novel method for the deposition of metal nanoparticles and its catalytic behavior in various electrochemical matrices.

4.2 Experimental

Substrates consisted of N-type Si(111) (1-10 Ω) (Polishing Corporation of America, 430 Martin Ave. Santa Clara, CA 95050. http://www.pcaSi.com/ - PCA#7493,) cut into 2 x 1 centimeter sizes. All Si substrates for this study were cleaned in hot solutions of SC1 (standard clean - 1; 1:1:5; H_2O_2:NH_4OH:H_2O) and SC2 (standard clean - 2; 1:1:5; H_2O_2:HCl:H_2O) for 10 minutes. Each hot cleaning step is followed by an etching step in 4.9% hydrofluoric acid (HF) and rinsed with UPW.

Ultrapure water (UPW) was supplied in-house via a Millipore Milli-Q® Elix5® ultrapure water (Millipore Corporation, Bedford, MA, http://www.millipore.com/) purification system (R>18.2 MΩ/cm) and used in rinsing of Si substrates as well as any dilution of chemicals. High purity electronic grade HF (Hashimoto, Osaka, Japan), H_2O_2, NH_4OH and HCl (the previous three chemicals are from Air Liquide, Dallas Chemical Center, 13456 N. Central Expwy., Dallas, Texas, 75243, http://airliquide.com/) were employed in the preparation of the Si substrates.

A Model PWM 32 Spinner (Headway Research, Inc., 3713 Forest Lane, Garland, Texas, 75042, http://www.headwayresearch.com/) is used for spinning photoresist onto the Si substrates. A small Teflon sample holder included with the spinner is used to hold the Si substrates in place during the spinnint process. After Si substrates are placed on the small holder, 1 mL of AZ® P4000 (Clariant Corporation, 70 Meister Avenue, Somerville, New Jersey, 00876, http://www.clariant.com/) photoresist is pipetted onto the substrate. The photoresist was then spun at a speed of 3000 revolutions per-minute (rpm) for a time duration of ten seconds. The coated substrates were then placed inside a quartz-tube which was in a Lindberg/Blue M Mini-Mite™ Model TF55035A tube furnace (Lindberg/Blue M, Asheville, NC, http://www.lindbergbluem.com/), fitted with a 16 set-point programmable temperature controller and an upper temperature limit of 1100°C. The substrates were heated in the tube furnace under a constant flow of forming gas (95% N_2/ 5% H_2) (Air Liquide, Dallas Chemical Center, 13456 N. Central Expwy., Dallas, Texas, 75243, http://airliquide.com/) at a ramping rate of 50°C per minute. The temperature was first ramped to 90°C and held there for 30 minutes, then increased to 300°C for 30 minutes and finally increased to 1000°C and held for one hour before it was allowed to cool back down to room temperature. This produced a front-side only pyrolyzed photoresist film (PPF) on the Si substrate.

Electroless deposition of Pt and Pd was done in perfluoro-alkoxy (PFA) labware. PFA labware was cleaned in multiple boilings of 10% HNO_3 and rinsed in UPW. Electroless deposition was accomplished by dipping substrates in various concentrations of HF (from 4.9% to 0.049%.) Palladium (Pd^{2+}) ICP/DCP standard solution stock (Aldrich Chemical Company, Sigma-Aldrich Corporation, St. Louis, MO http://www.sigmaaldrich.com/) and Platinum (Pt^{2+}) Spectrometric Standard Solutions (National Institute of Standards and Technology, Gaithersburg, MD http://www.nist.gov/) were used for making serial dilutions for the necessary amount of metal ion concentration. Electroless deposition of the metals were accomplished by dipping the PPF substrates in solution for varying times and varying concentrations of HF and metallic ion. Hexaammineruthenium(III)chloride (Aldrich Chemical Company, Sigma-Aldrich Corporation, St. Louis, MO http://www.sigmaaldrich.com/) and Mallinckrodt sulfuric acid (H_2SO_4) (Mallinckrodt Inc., Hazelwood, MO, http://www.mallinckrodt.com/) were used in preparation of a redox couple. Dopamine hydrochloride (Avacodo Research Chemicals Ltd, Shore Road, Lancashire, UK.) and potassium chloride (Alfa Aesar, 30 Bond Street,Ward Hill, MA 01835, http://www.alfa.com) were used to prepare another redox couple for electrochemical studies.

Electrochemistry was run on an EG&G Princeton Applied Research model 273A Potentiostat/Galvanostat (PerkinElmer, Inc., Wellesly, MA, http://www.perkinelmer.com/) with a standard three electrode setup with a platinum foil counter electrode, as well as a standard Model 90-02 Double Junction Ag/AgCl reference electrode (Orion Research Inc. Cummings Cente, Beverly, MA 01915, http://www.orionres.com/.) Before each experiment, the reference electrode was rinsed and the outer junction solution (10% KNO_3) was replenished.

Since this study involved only one side of the PPF substrate that was covered with the pyrolyzed carbon, some care was taken for the setup of the electrochemical cell to allow for solution contact only with the front side of the PPF.

X-ray Diffraction studies were conducted using a Siemens D500 diffractometer (Siemens AG, Munich Germany, http://www.siemens.com/). The tube source was operated using CuK_α radiation which emit x-rays with wavelengths of 1.54 Å at 40kV and 30 mA. Scans of two theta (2θ) were run at 0.05^o steps and a 1 second dwell time. Peak positions were confirmed against the PDF thumbnail database included in the XRD software. All scanning electron microscope (SEM) images were obtained with a JEOL JSM-T300 electron microscope (JEOL USA, Inc., Peabody, MA, http://www.jeol.com/) with an accelerating voltage of 15-25 kV and a working distance of 30-40 mm. Screen images were be photographed with Polaroid® instant photographic film (Polaroid Corporation, Waltham, MA, http://www.polaroid.com/) for permanent records. A Tracor Northern TN5500 series EDX instrument (Thermo Noran, Middleton, WI, (http://www.noran.com/) for elemental analysis, was coupled to the SEM. EDX analyses were done within the energy range of 0 – 10 keV, with a proprietary automatic peak identification software included. Pyrolyzed photoresist film (PPF) thicknesses were measured with an Alpha-Step® 500 Surface Profiler (KLA Tencor Corporation, San Jose, CA, http://www.kla-tencore.com/products/alpha-step_500/) and found to be 3-5 μm thick.

4.3 Results and Discussions

Electroless deposition of Cu, Ag, Pt, Pd and Au particles in HF solutions onto hydrogen terminated Si surfaces[5,21-23] and chemical vapor deposition (CVD) diamond films[24] has been previously demonstrated. For Si substrates, it is thought that the simultaneous etching and oxidation of the Si drives the electron transfer process for the deposition process. Previously reported atomic force microscopy (AFM) data[25,26] displaying extensive surface roughening due to oxidative etching support this displacement mechanism. Similar observations on CVD diamond films[24] are attributed to the rise in surface electron energy due to direct ohmic contact with the underlying Si substrate. The oxidative etching at the Si/HF interface creates excess electrons that migrate to the diamond surface in order for electroless deposition of metal particles. It is possible that a similar mechanism for electroless deposition of metal particles on PPF substrates also operates. Initial studies on highly oriented pyrolytic graphite (HOPG) indicate that this may be the case. HOPG alone does not show metal deposition when it is exposed to HF acid solutions with metallic ions. However, when the HOPG is in contact with a Si substrate, spontaneous metal deposition is seen to occur. Figure 4.2

shows the experimental apparatus and a representative SEM image of this phenomenon. 100 ppm Ag^+ in 0.49% HF was explored for a duration of 30 minutes. A plastic pipette tip was used to maintain HOPG contact with Si in solution so the HOPG sample would not float away.

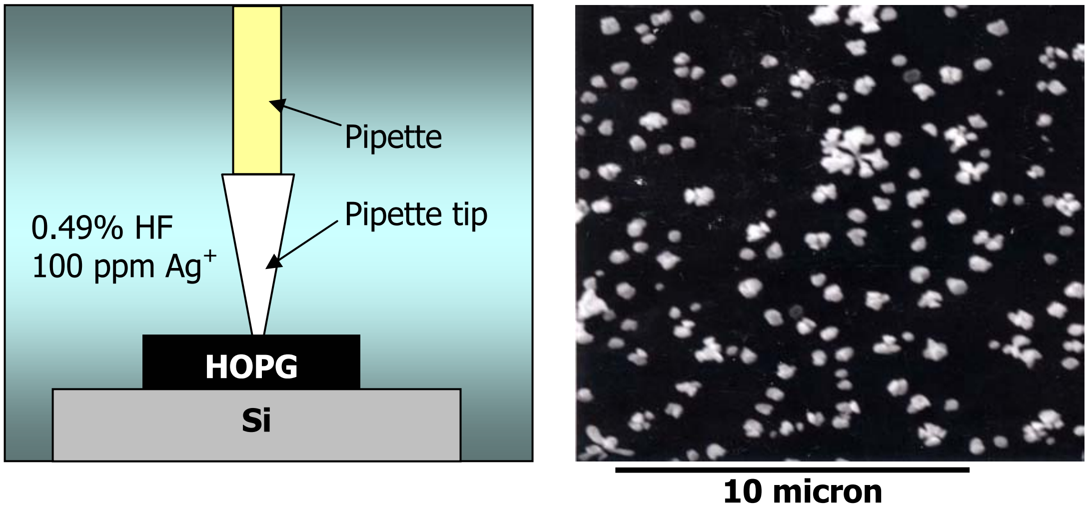

Figure 4.2 (A) Experimental Apparatus needed for spontaneous metal deposition on HOPG and (B) SEM image

Electroless deposition of Pd and Pt particles were carried under various time durations, metal ion content and HF acid concentrations. It is important to note that after HF acid concentration and time duration of exposure would eventually lead to a breakdown of the PPF. Figure 4.3 shows an SEM photograph of a film that has undergone processing in HF acid solutions for a duration of 30 minutes in 4.9% HF. Bubbling, buckling and delamination of the PPF on Si substrate is seen when HF exposure conditions are not ideal. The SEM picture shows a representative section of PPF film which has buckled and bubbled and eventually burst.

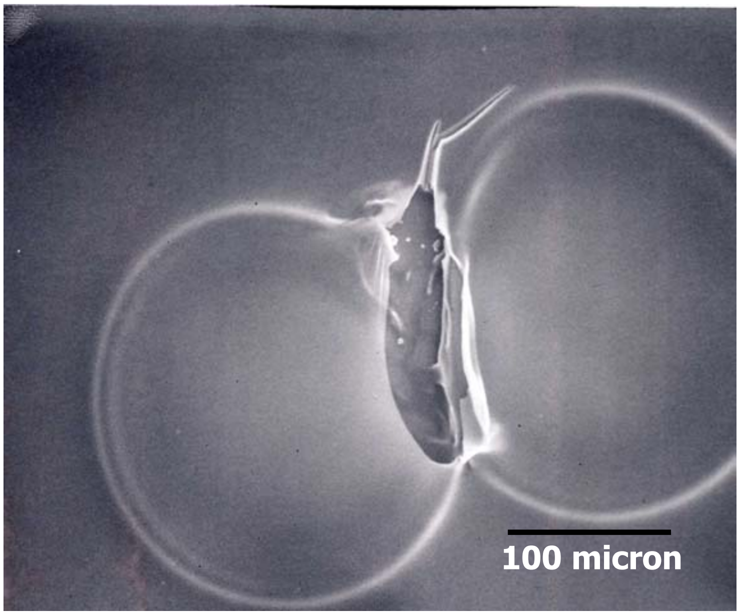

Figure 4.3 SEM photograph of PPF breakdown in 4.9% HF for 30 minutes.

A point of conjecture is that the PPF is in itself not sufficiently able to withstand HF chemical attack. It is possible that the PPF is slightly porous and there is a chance for undercutting in HF solutions, such that as the underlying substrate is changed underneath, even a minute change across the substrate is enough to overly stress the film.

The potential windows for electrochemical experiments on PPF were chosen due to adverse affects on the sample surfaces at high negative potentials. Scans run with a potential -700 mV and greater exhibited a sloughing off of the PPF from the Si substrate. This could be due to the effect of tension caused by hydrogen evolution at negative potentials on the PPF which would in turn cause there to be a rift between the PPF/Si interface. Lower concentration HF solutions were also found to have a detrimental effect on the electron transfer characteristics of the PPF substrates. After two hours of soaking in a 0.049% HF solution, it was found that although the PPF remains intact the electron transfer characteristics are diminished as seen later in this chapter.

SEM and EDX used in combination were able to characterize electrolessly deposited Pt and Pd on PPF. Initial investigations with the metal nanoparticles were undertaken at the 100 parts per million (ppm) and 500 ppm concentration of metal ion in 0.049% HF. At such a low concentration of HF solution, the PPF was able to withstand the acid media for duration of three hours and still maintain it resiliency. Figure 4.4 shows representative SEM images of electrolessly deposited 100 ppm Pt^{2+} and 500 ppm Pt^{2+} after deposition in 0.049% HF for 1 and 3 hours.

Deposition of 100 ppm Pt^{2+} shows both large and small clusters of the metal on the PPF surface, yet after three hours, it is seen that larger cluster have fallen away. It is presumed that the larger clusters have fallen away under their own weight as size of the cluster becomes too unwieldy to maintain on the PPF surface. 500 ppm Pt^{2+} show an increase in the amount of smaller clusters from one to three hours. It must also be noted that the metal nanoparticles deposited in 500 ppm Pt^{2+} deposition seems to be better defined than that of the 100 ppm Pt^{2+} deposition. It may be possible that as

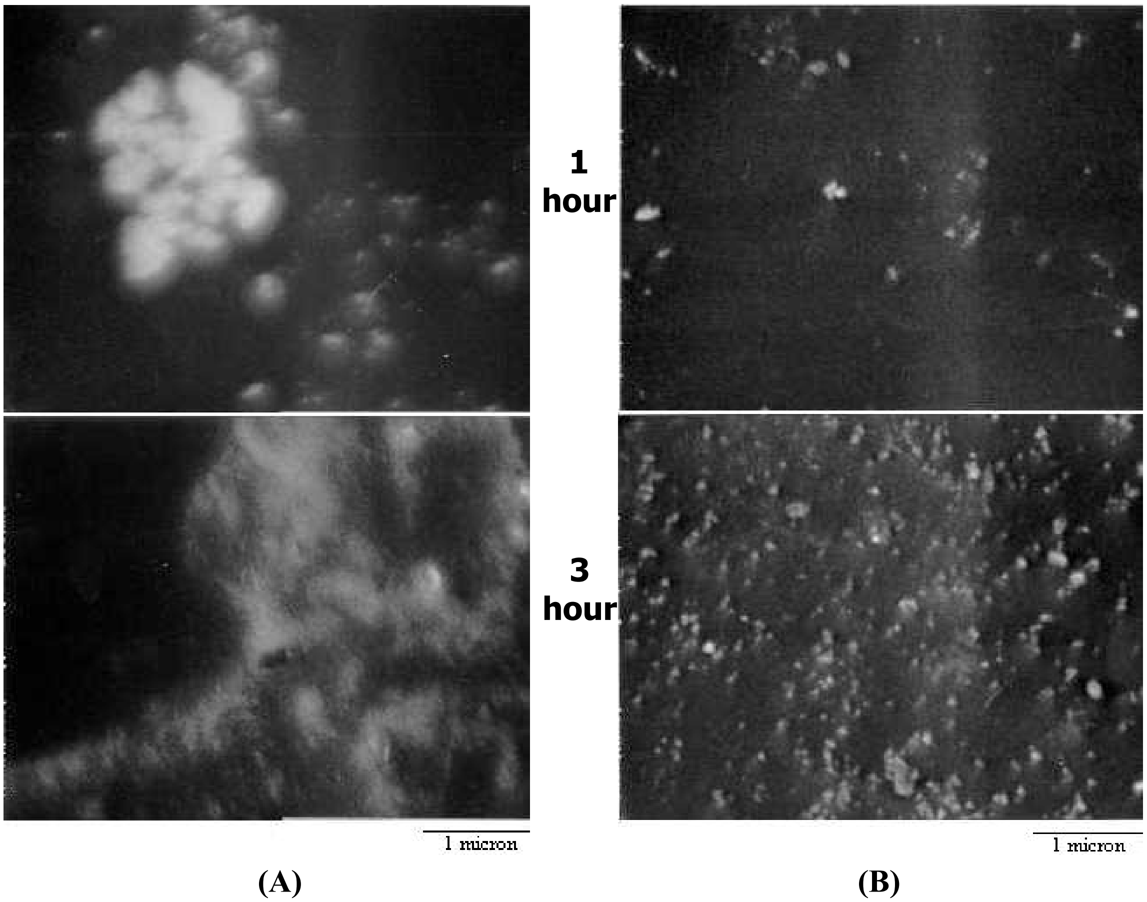

Figure 4.4 SEM photograph of (A) 100 ppm Pt^{2+} and (B) 500 ppm Pt^{2+} deposited on PPF/Si substrates in 0.049% HF after 1 and 3 hour deposition times.

nucleation begins in the 100 ppm Pt^{2+} that smaller concentration means that Pt will tend to aggregate toward already deposited particulates allowing for more growth. The 500 ppm Pt^{2+} nucleation may occur in such a way that the higher concentration allows for more nucleation at a greater number of active sites to take place. This would somewhat supplant the growth mechanism of particulates so that there would be more particulates with less growth seen. The deposition is seen to be more uniform across the PPF surface.

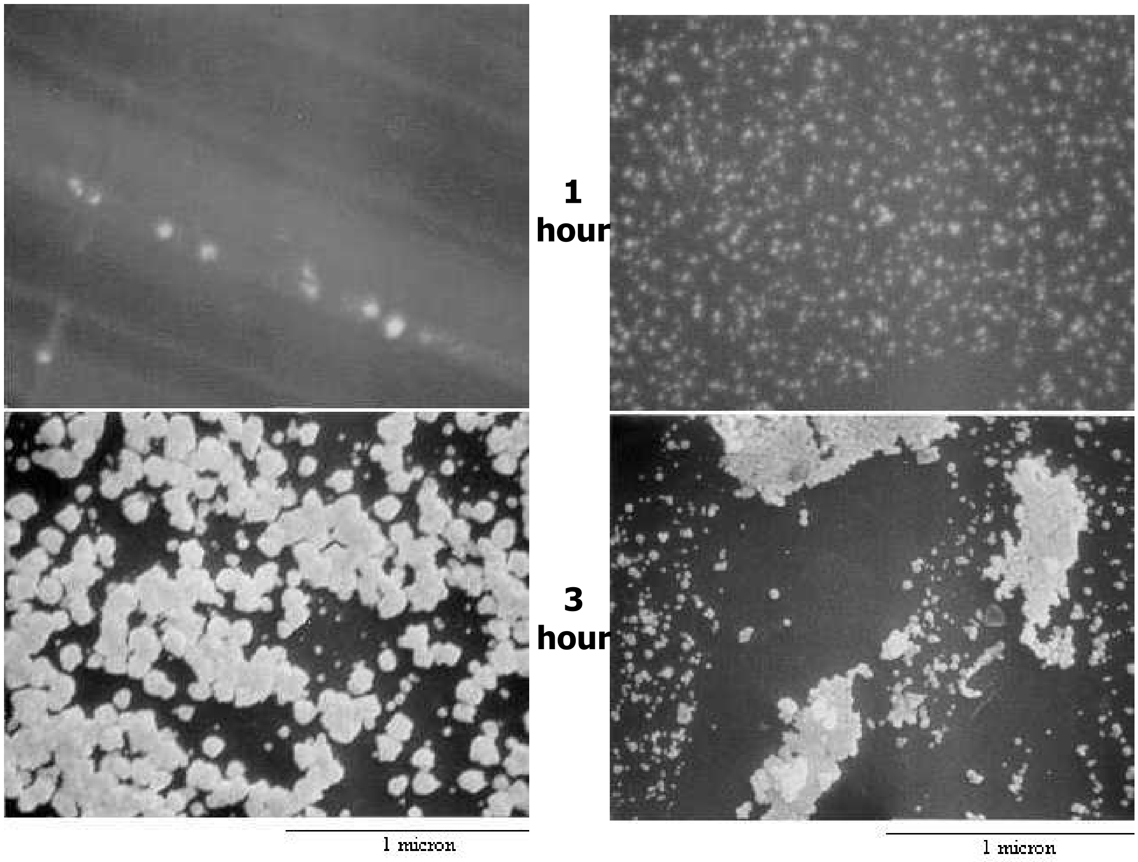

(A) **(B)**

Figure 4.5 SEM photograph of (A) 100 ppm Pd^{2+} and (B) 500 ppm Pd^{2+} deposited on PPF/Si substrates in 0.049% HF after 1 and 3 hour deposition times.

Figure 4.5 shows representative SEM photographs of electrolessly deposited Pd^{2+} at 100 ppm and 500 ppm concentrations after one and three hour deposition times in 0.049% HF. A 100 ppm Pd^{2+} deposition at one hour shows meager deposition. A three hour deposition time for 100 ppm Pd^{2+}, though, shows a much greater increase in both size and number of particles of Pd. 500 ppm Pd^{2+} deposition exhibits a greater number of particulates forming from one to three hours. Three hours of deposition show large gaps appearing from the groups of particulate. Growth may be occurring such that the groups of particulates are coming off the surface of the PPF under its own weight. SEM data corroborates with CV data for the evolution of hydrogen in sulfuric acid solutions.

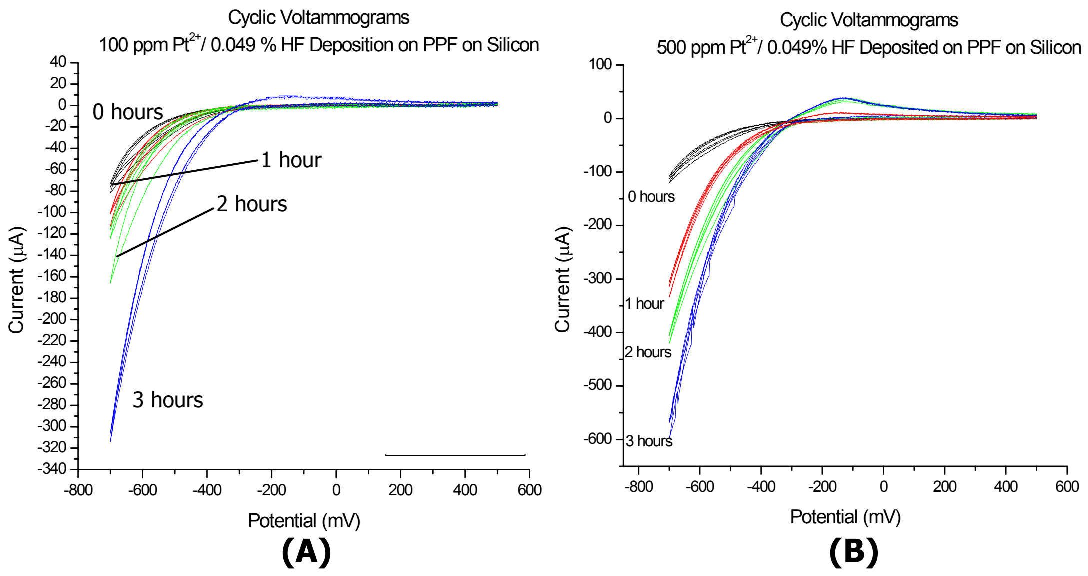

Figure 4.6 CV of (A) 100 ppm Pt^{2+} and (B) 500 ppm Pt^{2+} in 0.1 M H_2SO_4

Figure 4.6 shows a cyclic voltammogram (CV) in sulfuric acid solution of (A)100 ppm Pt^{2+} and (B) 500 pm Pt^{2+} deposited on PPF at various times. CV data exhibits general catalytic behavior for the evolution of hydrogen. The cathodic current of hydrogen evolution progressively increased as the time of deposition, and hence, the amount of metal particulates, increases. This signifies an increase in the electron transfer rate. This is also seen as the onset of hydrogen evolution meaning that less energy is needed to facilitate electron transfer for the evolution of hydrogen. SEM data corroborates with CV data for the evolution of hydrogen in sulfuric acid solutions.

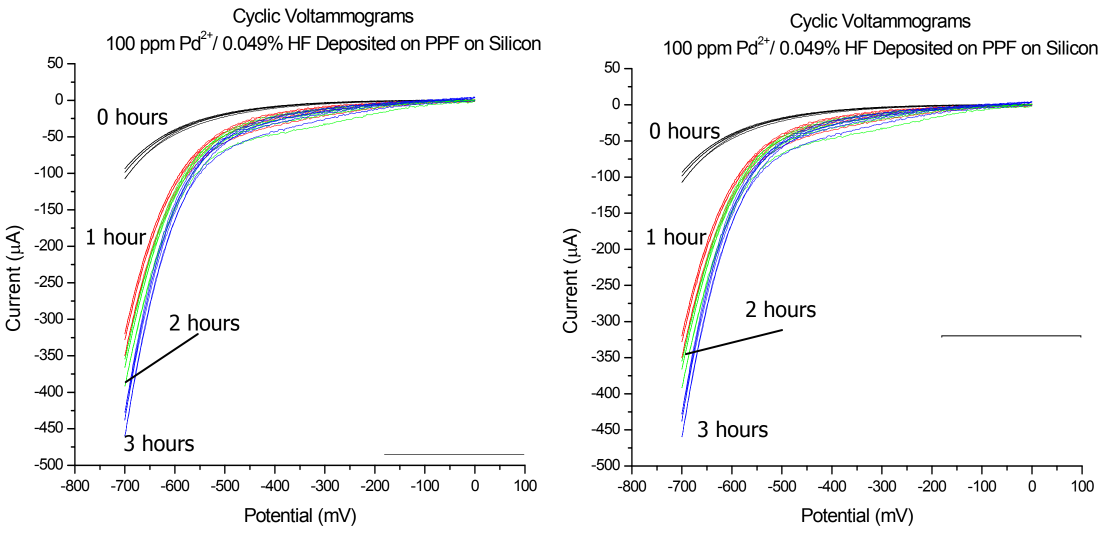

(A) **(B)**

Figure 4.7 CV of (A) 100 ppm Pd^{2+} and (B) 500 ppm Pd^{2+} in 0.1 M H_2SO_4

Figure 4.7 exhibits the electrochemical behavior of (A) 100 and (B) 500 ppm Pd^{2+} deposited on PPF. The 100 ppm concentration exhibits expected behavior showing an increase in the efficiency of hydrogen evolution. For the most part, the 500 ppm concentration also shows expected behavior up to the third hour of deposition, where the rate of hydrogen evolution is lower as measured by CV's in 0.1 M H_2SO_4. Palladium deposited PPF samples seem to show much closer values for onset and current at switching potentials after various deposition times. This would seem to be indicative of a corresponding maximum load of Pd with respect to hydrogen evolution.

It must be mentioned that the 500 ppm concentration of Pd shows an occasional lapse in the trend of lower current and potential onset of hydrogen evolution in 0.1 M H_2SO_4, albeit the values are close to the second hour of deposition. It would seem that the gaps created from an overabundance of Pd deposition may play a role in the decrease of hydrogen evolution such that the maximum load of Pd that occurs on the PPF surface occurs somewhere between hour 2 and 3.

Electrochemical investigations with metal deposited PPF substrates add further insight into their catalytic behavior. Initial experiments with redox couples seemed to indicate that the Pt and Pd particles were having no effect on the electron transfer kinetics. It was supposed that the detrimental effect of HF solutions after depositions were hampering the ability of the PPF and metal particles from being able to exhibit the proper catalytic behavior which is expected. Indeed, it was discovered that after deposition of ppm Pt or Pd deposition at 0.049% HF, the electron charge transfer kinetics did not improve. Therefore, a series of trials were conducted to ensure that the proper amount of metal was deposited on the surface of the PPF substrates. It was found that increasing the concentration of HF increased the rate of deposition of metal particles. Increasing HF concentration, though, brought about problems with PPF stability through delamination and buckling of the PPF. A concentration of 1000 ppm metal ion concentration in 0.49% HF solution was found to sufficiently deposit enough metal on the PPF substrates without overtly destroying or delaminating the PPF

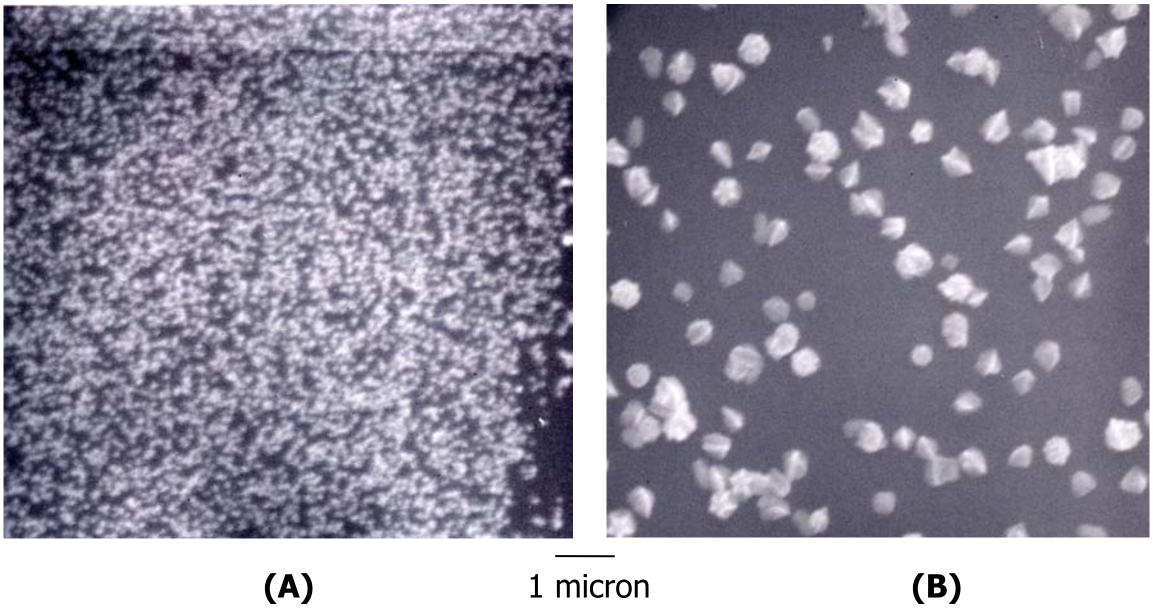

Figure 4.8 SEM of 0.49% HF deposited (A) 1000 ppm Pt 30 minutes and (B) 1000 ppm Pd 10 minutes

surface. Deposition of 1000 ppm Pt^{2+} for a duration of 30 minutes was found to show a large amount of small nuclei covering the surface. Conversely, 1000 ppm Pd deposition for 10 minutes in 0.49% HF shows more sparse coverage, but with particles ~50 times larger than that of the Pt deposits. Figure 4.8 shows SEM photographs of (A) Pt and (B) Pd metal particles deposited on PPF surfaces after exposure to 0.49% HF. Further exposure to 0.49% HF solutions proves to be detrimental to the state of the PPF surfaces with surface delamination visible under optical microscopy.

X-ray diffraction of these palladium and platinum deposited PPF substrates were run. Figure 4.9 show XRD graphs of (A) Pd and (B) Pt deposited PPF

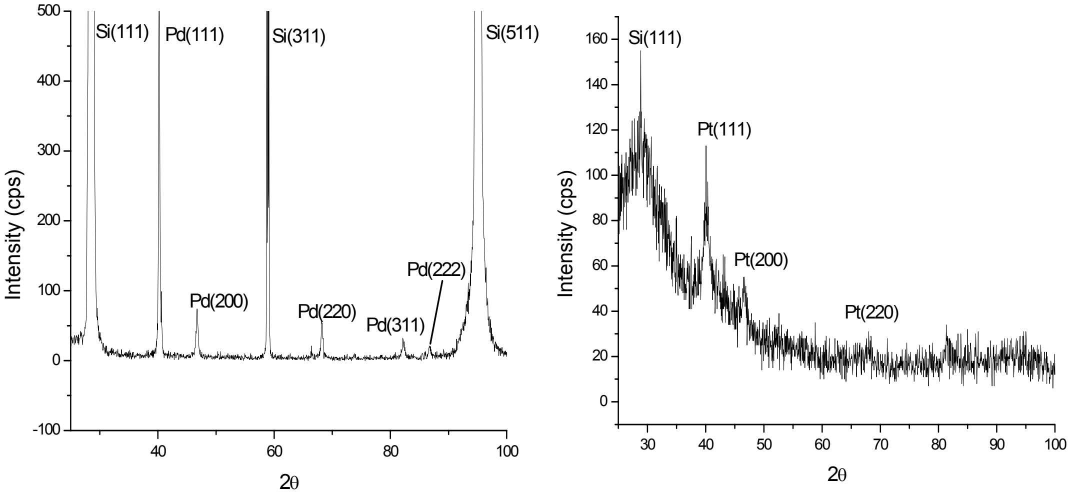

Figure 4.9 XRD of Pd and Pt deposited on PPF substrates

substrates that were deposited in 1000ppm in 0.49% HF. Both substrates are dominated by the Si(111) crystal peak. This is expected since the PPF was formed on single crystal Si(111) wafer. Both the palladium and platinum peaks show up in normal positions when referenced to the XRD database. Platinum peak intensities were roughly ¼ of those observed on palladium. This is indicative of smaller crystallite sizes of the Pt particles and is verified by SEM. Since there is no peak shifting seen, it can be assumed that the deposited platinum and palladium particles or not acted upon by any lattice strain. XRD is used to obtain information on the amount of lattice strain on a given sample phase. The data collected from metal deposited PPF samples contain an internal standard in the Si(111) single crystal wafers which were used as the underlying substrate. Corrected 2θ values (2θ(corr)) are obtained by subtracting the 2θ(corr) value obtained from the Si(111) substrate. From Bragg's Law we know that:

$$n\boldsymbol{\lambda} = 2d \sin \boldsymbol{\theta}$$

where θ is the diffraction angle, d is the interplanar distance, λ is the x-ray wavelength, and n is an integer. Rearrangement of Bragg's Law states:

$$d = \frac{n\boldsymbol{\lambda}}{2 \sin \boldsymbol{\theta}}$$

Thus the relationship of θ to d states that if a peak shift to higher θ values occurs, then d is seen to become smaller than the theoretical value and vice-versa. A decrease in d gives compressive stress along the given <hkl> phase while an increase in d shows tensile stress. By comparing theoretical and observed values, the following relationship can be seen:

$$d_n \sin \theta_{corr} = d_{theor} \sin \theta_{theor}$$

such that d_n can be calculated:

$$d_n = \frac{d_{theor} \sin \boldsymbol{\theta}_{theor}}{\sin \boldsymbol{\theta}_{corr}}$$

The value of ε is represents strain for a particular <hkl> phase and is calculated by:

$$\boldsymbol{\varepsilon} = \frac{d_n - d_{theor}}{d_{theor}}$$

and is further calculated as a value for residual stress (σ) using the constant of (Y/v) where Y is Young's modulus of force per cross sectional unit divided by strain and v is the Poisson's ratio for lateral contraction. This widely used standard is applied for the characterization of phases for bulk and film solids[27,28]. Table 4.1 shows the calculated values for the Pd (1000 ppm for 10 minute deposition) and Pt (1000 ppm for 30 minute deposition) particles deposited on PPF films in 0.49% HF solutions. The values for σ are consistently >1 indicative of no strain on the Pd and Pt phases.

SAMPLE	**PHASE**	**2 θ (exp)**	**2θ (corr)**	**2θ (theor)**	**d(A) (theor)**	**d(A)n (exp)**	**%ε**	**σ=-ε(Y/v)**
Si wafer	Si(111)	28.55	**0.11**	28.44	3.1355	NA		
For 1000ppm Pd(II) 0.49% HF	Pd(111)	40.2	40.09	40.118	2.2458	2.247	0.0669	**-0.2077**
	Pd(200)	46.7	46.59	46.658	1.9451	1.948	0.1378	**-0.4275**
	Pd(220)	68.15	68.04	68.119	1.3754	1.377	0.1021	**-0.3167**
	Pd(311)	82.15	82.04	82.098	1.173	1.174	0.0581	**-0.1804**
	Pd(222)	86.8	86.69	86.617	1.123	1.122	-0.0675	**0.20947**
Si wafer	Si(111)	28.85	**0.41**	28.44	3.1355	NA		
1000ppm Pt(II) in 0.49% HF	Pt(111)	40.05	39.64	39.763	2.265	2.272	0.2977	**-0.9238**
	Pt(200)	46.5	46.09	46.243	1.9616	1.968	0.3137	**-0.9735**
	Pt(220)	68	67.59	67.454	1.3873	1.385	-0.177	**0.55036**

Table 4.1 Calculated values for stress and strain of Pd and Pt particles on PPF.

Electron transfer kinetics of Ruthenium hexamine ($[Ru(NH_3)_6)]^{3+/2+}$) and Dopamine (DA) redox couples were investigated for the 0.49% HF/ 1000 ppm Pd and Pt deposited PPF substrates. The $[Ru(NH_3)_6)]^{3+/2+}$ redox couple is termed an outer-sphere activated complex[28] where the transfer of electrons takes place in bulk solution by an outer-sphere electron transfer. Outer-sphere electron transfer is a process where a minimal change occurs to the coordination sphere of the atoms undergoing the change in oxidation number[29]. In such electron transfers, coordination spheres remain intact with only a minimal change in metal-ligand distances. Electron transfer of this kind is relatively fast. Previous studies on glassy carbon and PPF surfaces[3,6,7,9,30,31] have used the $[Ru(NH_3)_6)]^{3+/2+}$ redox couple to illustrate that the carbon surfaces specifically are acting as an electron source through the chemical changes occurring on the surface.

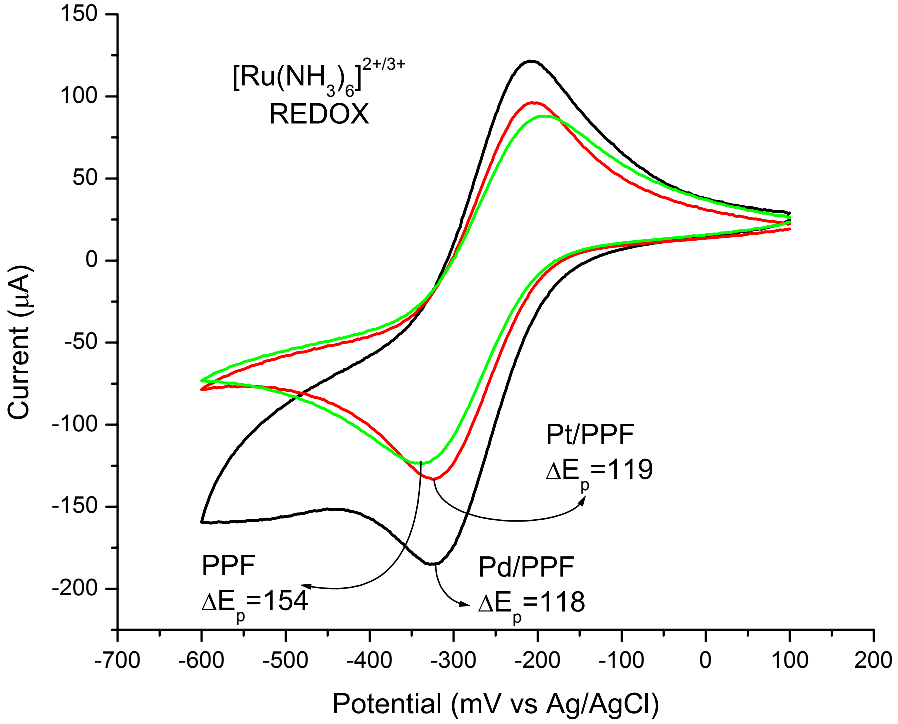

Figure 4.10 Representative CV's of Normal, Pd, and Pt deposited PPF substrates in $Ru(NH_3)_6^{2+/3+}$ redox couple

Figure 4.10 shows an overlay of non-deposited, Pt and Pd deposited PPF substrate CV's run at a scan rate of 200 mV/second. The concentration of 1 mM

$[Ru(NH_3)_6)]^{3+/2+}$ in 1 M KCl was used. The PPF only substrates show a well-defined symmetric voltammogram for the $[Ru(NH_3)_6)]^{3+/2+}$ redox couple. The Pt deposited PPF substrate also shows a well defined symmetric CV in the redox couple with a decrease in peak to peak separation (ΔE_p) by 35 mV. The CV of Pd deposited PPF substrates also show a decrease in of ΔE_p by 35 mV. The oxidative and reductive peak currents also consistently show a marked increase. The symmetry of the CV is marred by what could be seen as the beginnings of hydrogen evolution at -440 mV. Though not seen with Pt deposited PPF substrates, it may be surmised that the size of the Pd deposits on the PPF substrates plays a large role both the peak current intensities and the possibility for the beginnings of hydrogen evolution. The ΔE_p decrease after deposition of Pt and Pd particles is indicative of an increase in electron transfer rates meaning that less potential is needed for the electron transfer to take place for the reduction and oxidation of the $[Ru(NH_3)_6)]^{3+/2+}$ redox couple.

Metal deposited PPF substrates were also studied using dopamine (DA) redox couples. Dopamine, 3,4-dihidroxyphenylethylamine, is a neural transmitter found in the brain. Dopamine is also a well known 2 electron transfer redox couple for its sensitivity to surface conditions[2,3,6,7]. As a non-reversible redox couple, DA breaks down into quinone and easily poisons the surface of electrodes. Though this behavior has not been fully realized, it is hypothesized that ionic effects related to surface oxides, proton transfer from oxidation sites, or an electrocatalysis by adsorption play a role for its sensitivity. Previous studies have shown that DA kinetics vary greatly when comparing PPF and glassy carbon (GC) surfaces[7]. It was observed that the electron transfer rate on PPF was much slower on PPF than on GC due to the differences in surface composition. This pronounced sensitivity of DA kinetics makes DA an important redox couple for the testing of the stability and capability of PPF and metal deposited PPF surfaces.

Cyclic voltammograms were run in 1mM DA in 1M H_2SO_4 at a scan rate of 200 mV/second for normal PPF, Pd, and Pt deposited PPF substrates. Figure 4.11 shows an overlaid cyclic voltammogram of normal PPF, Pd and Pt deposited PPF substrates. Pd deposited substrates consistently show a marked decrease in ΔE_p of ~93eV. This is

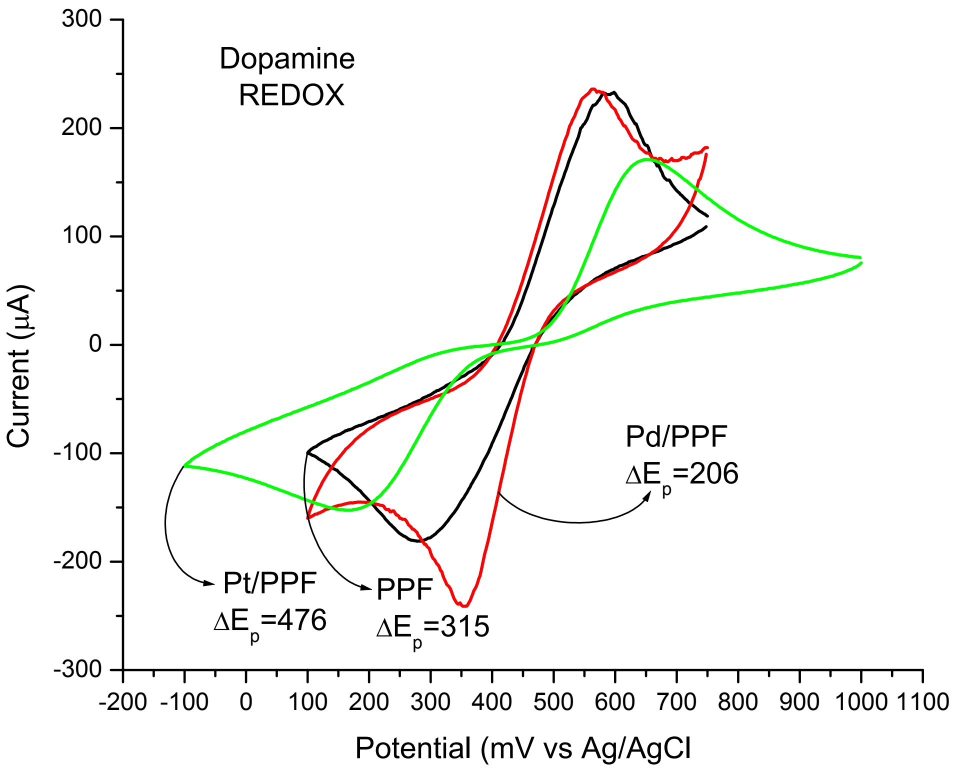

Figure 4.11 Representative CV's of Normal, Pd, and Pt deposited PPF substrates in Dopamine redox couple solutions.

indicative of an increase in rate of electron transfer for the DA redox couple. Conversely, the Pt deposited PPF substrate consistently shows a marked increase in ΔE_p (~193 eV) indicative of a decrease in electron transfer rates for the DA redox system. This conundrum of decreasing rates can be explained by the deposition time in HF of the Pt vs Pd particles on PPF. The Pt deposition time in 0.49% HF is 3x (30 minutes) that of the Pd deposition time (10 minutes.) With this increase in deposition time at 0.49% HF, it is plausible that the time and concentration of HF are playing a detrimental role to the PPF surface, effectively counteracting any positive catalytic effects which the deposited Pt particles may have. In order to test this hypothesis, data

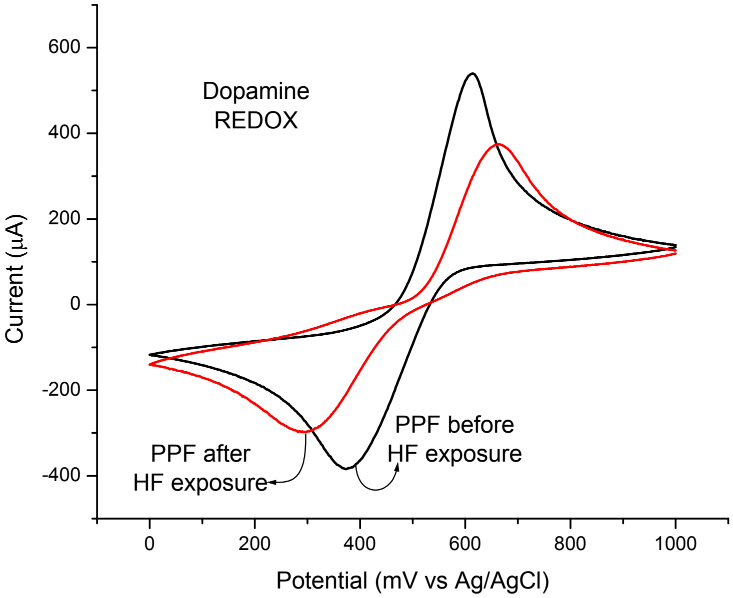

Figure 4.12 Cyclic Voltammograms of PPF substrates before and after HF exposure

for CVs of PPF in dopamine before and after exposure to 0.049% HF for two hours illustrates this point. The overlaid CVs seen in Figure 4.12 before 0.049% HF exposure shows a ΔE_p 120 mV less than that of the CV after exposure to 0.049% HF. This evidence of the decrease in efficiency of PPF after HF exposure and the physical evidence seen when exposure to HF causes the film to peel from the Si substrate (seen in Figure 4.3) seems to indicate that HF is deteriorating the surface of the PPF film.

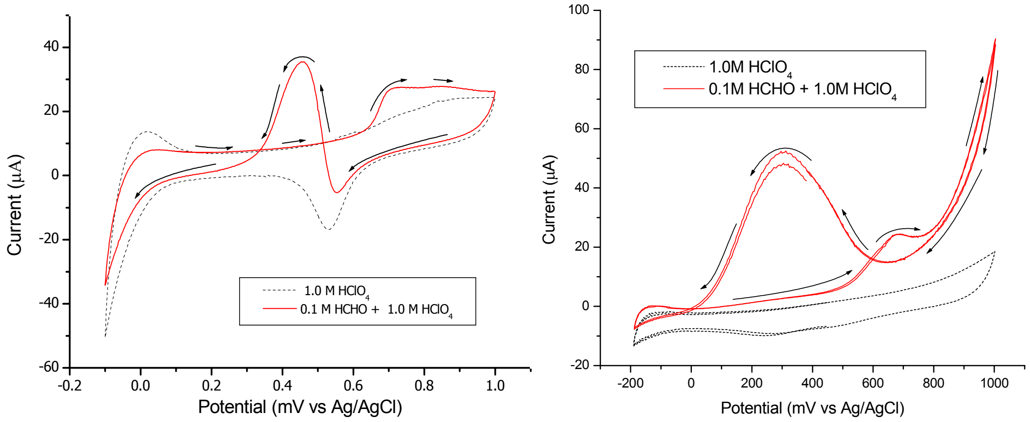

(A) **(B)**

Figure 4.13 CV's of(A) Pd and (B) Pt disk in 0.1M HCHO and 1M $HClO_4$

Initial studies were done to observe the effects of metal deposition on the catalysis of formaldehyde (HCHO) solutions. This is especially important for the development of fuel cells. The commonly accepted mechanism for electrocatalytic oxidation of formaldehyde is seen to be[32]:

$$HCHO \rightarrow CO(ads) + 2H^+ + 2e^-$$

$$CO(ads) + H_2O \rightarrow CO_2 + 2H^+ + 2e^-$$

where the decomposition of HCHO leads to adsorbed CO species on the electrode surface followed by the oxidation of adsorbed species to CO_2. This is seen on an anodic peak at circa + 700 mV on Pt and Pd disk electrodes in Figure 4.13. This mechanism is known as the indirect oxidation of HCHO through carbon monoxide adsorption. This indirect oxidation is thought to suppress any direct oxidation of the HCHO species until all adsorbed species have been oxidized leaving a clean electrode surface for direct oxidation. Direct oxidation of the HCHO species is seen:

$$HCHO+ H_2O \rightarrow H_2C(OH)_2$$

$$H_2C(OH)_2 \rightarrow CO_2 + 4H^+ + e^-.$$

The direct oxidation of HCHO is catalyzed by the CO free electrode surface at circa +300-450 mV on Pd and Pt disk electrodes as illustrated in Figure 4.13.

Cyclic volatmmograms of platinum and palladium deposited PPF substrates show mixed results as seen in Figure 4.14. Platinum deposited PPF substrates consistently gave electrocatalytic oxidation of formaldehyde in the + 300 mV region. Conversely, palladium deposited PPF substrates consistently showed no electrocatalytic oxidation of formaldehyde. Activation of the palladium deposited PPF substrates was also attempted by cycling the Pd/PPF in a 1.0 M NaOH / 0.1 M HCHO solution for up to 20 cycles at 100 mV/s scan rate, after which no catalysis of HCHO was observed. Previous studies conducted on Pd deposited diamond films show a discrepancy in the behavior of electrocatalysis for HCHO[33]. A reason for the non-catalytic behavior of Pd/PPF substrates is not known and any argument is pure speculation. Surface restructuring of Pd could be occurring during potential cycling causing distortion and strain leading to non-ideal behavior for Pd catalysis. There may also be negative effects which have occurred by means of strain or microscopic surface damage due to HF exposure of the PPF substrates.

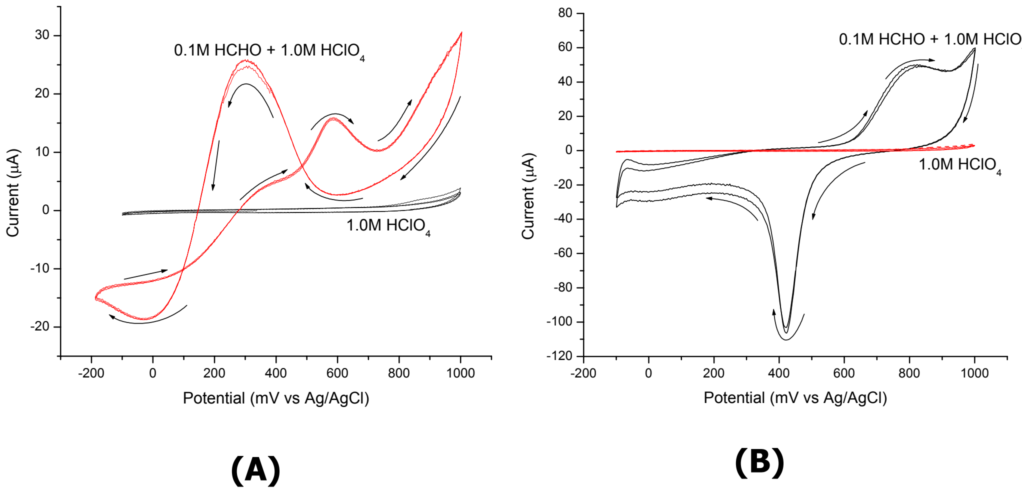

Figure 4.14 CV of (A) Pt/PPF substrate and (B) Pd/PPF substrate in 0.1M HCHO and 1M $HClO_4$

Unfortunately, there remains much to be explored and answered for the behavior of palladium and platinum deposited pyrolyzed photoresist film substrates. It would be interesting to observe Pd and Pt PPF substrates against whole gamut of redox couples. The caustic effects of hydrofluoric acid solutions on the PPF/Si interface must be addressed more thoroughly. The curious observation of non-catalysis in dopamine redox couples (for Pt/PPF substrates) and formaldehyde (for Pd/PPF substrates) also needs to be explored in a more complete manner. Although the results of this study are inconclusive, electrolessly deposited metal nanoparticles on PPF have the potential to be a boon as catalysts for future electrochemical and fuel cell systems.

4.4 References

(1) McFadden, C. F.; Russell, L. L.; Melaragano, P. R.; Davis, J. A. *Analytical Chemistry* **1990**, *62*, 742.

(2) Niwa, O.; Tabel, H. *Analytical Chemistry* **1994**, *66*, 285.

(3) Ranganathan, S.; McCreery, R. L. *Analytical Chemistry* **2001**, *73*, 893-900.

(4) Schlesinger, R.; Bruns, M.; Ache, H.-J. *Journal of the Electrochemical Society* **1997**, *144*, 6.

(5) Clark, J. K.; Schilling, W. A.; Wijayawardhana, C. A.; Melaragano, P. R. *Analytical Chemistry* **1994**, *66*, 3528.

(6) Kostecki, R.; Song, X.; Kinoshita, K. *Electrochemical and Solid-State Letters* **1999**, *2*, 465-467.

(7) Ranganathan, S.; McCreery, R. L.; Maiji, S. M.; Madou, M. *Journal of the Electrochemical Society* **2000**, *147*, 277-282.

(8) Jenkins, G.; Kawamura, K. *Polymeric Carbons-Carbon Fibre, Glass and Char*; Cambridge University Press: Cambridge, England, 1976.

(9) Kim, J.; Song, X.; Kinoshita, K.; Madou, M.; White, R. *Journal of the Electrochemical Society* **1998**, *145*, 2314-2319.

(10) Runyan, W. R.; Bean, K. E. *Semiconductor Integrated Circuit Processing Technology*; Addison-Wesley Publishing Company: Reading, 1990.

(11) Sherstyuk, O. V.; Pron'kin, S. N.; Chuvlin, A. L.; Salanoz, A. N.; Savinova, E. R.; Tsirlina, G. A.; Petrii, O. A. *Russian Journal of Electrochemistry* **2000**, *36*, 741-751.

(12) Cox, J. A.; Tess, M. E.; Cummings, T. E. *Reviews of Analiytical Chemistry* **1996**, *15*, 173-223.

(13) Lee, S.-B.; Pyun, S.-I. *Journal of Applied Electrochemistry* **2000**, *30*, 795-801.

(14) Gurrath, M.; Kuretzky, T.; Boehm, H. P.; Okhlopkova, L. B.; Lisitsyn, A. S.; Likholobov, V. A. *Carbon* **2000**, *38*, 1241-1255.

(15) Liu, S.; Tang, Z.; Wang, E.; Dong, S. *Electrchemistry Communications* **2000**, *2*, 800-804.

(16) Ozaki, J.; Ohizumi, W.; Oya, A.; Illan-Gomez, M. J.; Raman-Martinez, M. C.; Linares-Solano, A. *Carbon* **2000**, *38*, 775-785.

(17) Ahmadi, T. S.; Wang, X. L.; Henglein, A.; El-Sayed, M. A. *Chemistry of Materials* **1996**, *8*, 1161-1163.

(18) Makkee, M.; Wiresma, A.; can de Sandant, E. J. A. X.; van Bekkum, H.; Moulijn, J. A. *Catalysis Today* **2000**, *55*, 125-137.

(19) Xhie, J.; Sattler, K.; Muller, U.; Venkateswaran, N.; Raina, J. *Journal of Vaccuum Science and Technology, B* **1991**, *9*, 833.

(20) Gullon, J. S.-┬ . ; Montiel, V.; Aldaz, A.; Clavilier, J. *Electrochemistry Communications* **2002**, *4*, 716-721.

(21) Chyan, O.; Chen, J.-J.; Wu, J.; Chien, S.; Liu, M. In *Electrochemical Synthesis and Modification of Materials*; Andricaco, P. C., Corcoran, S. G., Delplancke, J.-L., Moffat, T. P., Searson, P. C., Eds.; Materials Research Society: Pittsburgh, 1997; Vol. 451, pp 267-273.

(22) Rotondaro, A. L. P.; Hurd, T. W.; Schmidt, H. F.; Teerlinck, I.; Heyns, M. M.; Claeys, C. In *Ultraclean Semiconductor Processing Technology and Surface Chemical Cleaning and Passivation*; Lieh, M., Heyns, M., Hirose, M., Parks, H., Eds.; Materials Research Society: Pittsburgh, 1995; Vol. 386, pp 183-188.

(23) Ohmi, T.; Imaoka, T.; Sugiyama, I.; Kesuka, T. *Journal of The Electrochemical Society* **1992**, *139*, 3317-3335.

(24) Gao, J.-S.; Arunagiri, T.; Chen, J.-J.; Goodwill, P.; Chyan, O. *Chemistry of Materials* **2000**, *12*, 3495-3500.

(25) Chyan, O. M. R.; Chen, J.-J.; Chien, H.-Y.; Wu, J. J.; Lie, M. *Journal of The Electrochemical Society* **1996**, *143*, L235-L237.

(26) Chyan, O. M. R.; Chen, J.-J.; Chien, H.-Y. *Journal of The Electrochemical Society* **1996**, *143*, 92-96.

(27) James, R. W. *X-RAY CRYSTALLOGRAPHY*; Fifth ed.; Butler and Tanner LTD.: London, 1962.

(28) Klug, H. P.; Alexander, L. E. *X-RAY DIFFRACTION PROCEDURES: For Polycrystalline and Amorphous Materials*; Second ed.; Wiler-Interscience: New York, 1974.

(29) Shriver, D. F.; Atkins, P. W. *Inorganic Chemistry*; third ed.; W.H.Freeman and Company: New York, 2000.

(30) Chen, P.; McCreery, R. L. *Analytical Chemistry* **1996**, *68*, 3958-3965.

(31) Kuo, T.-C.; McCreery, R. L. *Analytical Chemistry* **1999**, *71*, 1553-1560.

(32) Parsons, R.; VanderNoot, T. *Journal of Electroanalytical Chemistry* **1988**, *257*, 9-45.

(33) Arunagiri, T. *Interfacial Electrochemistry of Metal Nanoparticles on Diamond and Copper Electroplating on Ruthenium Surface - Dissertation*; University of North Texas: Denton, 2003.

CHAPTER 5

INVESTIGATION INTO THE VIABILITY OF Ir AS A COPPER DIFFUSION BARRIER FOR Cu INTERCONNECTS

5.1 Introduction

Iridium (Ir) is a hard, air stable transition metal element with a high melting point (2466 ^{o}C) and an unusually high corrosion-resistance, withstanding attack even by aqua regia. Presently, Ir is currently explored and used as electrode material for ferroelectric non-volatile random access memories (FRAMs) [1-4] and has been studied and used for field effect transistors [5,6]. FRAMS combine the benefits of small direct random access memory (DRAM) cell sizes, fast read and write behavior, low power needs, and nonvolatility to give small memory devices which are ideally suitable for mobile applications and ever popular personal digital assistants (PDAs.) A basic FRAM capacitor consists of some ferroelectric material, such as $Pb(Zr,Ti)O_3$ (PZT), sandwiched between two metal electrodes, which are in place on a Si substrate device. Ir has been seen as an ideal material for FRAMS because while being a good conductive electrode, it is thermally stable up to 700^{o}C and adheres well to Si substrates as well as being a good oxygen diffusion layer [7,8]. There is also the possibility that Ir may be an ideal candidate for as a copper diffusion barrier in the sub-0.13 μm generation intergrated circuit.

Ir has a face-centered cubic crystalline structure and a high electrical conductivity (4.7$\mu\Omega$ cm) and according to the copper (Cu)-Ir binary phase diagram[9], there is limited solid solubility of Ir with Cu at 700^{o} C. This feature is of paramount importance when investigating Ir as a contending diffusion barrier for Cu interconnects in the next generation integrated circuit (IC) devices. Currently tantalum (Ta) and tantalum nitride (TaN) are used as diffusion barriers to contain Cu interconnects from device contamination[10-15]. Current configurations of Cu-seed/Ta/TaN stacks require very fine control in order to avoid poor sidewall coverage and large overhangs surrounding the vias, leading to Cu electrofill close-off and the creation of unwanted void defects. There have been previous reports of direct Cu electroplating onto diffusion barrier films on Si substrates[16,17], but thin barriers of TaN are too resistive (>200 $\mu\Omega$ cm) for direct Cu electroplating[18].

This chapter will report the electrodeposition and characterization of Cu thin film onto Ir metal substrates. Cu/Ir samples were characterized with x-ray photoelectron spectroscopy, scanning electron microscopy, x-ray diffraction as well as current transient techniques by potential stepping for studying electrochemical nucleation and growth of Cu on Ir. Cu/Ir samples were analyzed before and after annealing up to 600 ^{o}C in N_2 atmosphere. The adhesion of Cu thin films were evaluated by scotch-tape peeling tests.

5.2 Experimental

Ir shots (Electronic Space Products International, Ashland, OR, http://www.espi-metals.com/) were made into disk electrodes with ohmic contact made by soldering copper cable to the backside of the shot. The electrode was then encased in Leco® metallographic resin and hardener epoxy respectively (Leco Corporation, St. Joseph, MI, http://www.leco.com/) mixture of 100:14 ratio by mass, in a plastic mold with a hole drilled for the wire. The bottom is covered with paraffin wax film to prevent epoxy resin from running out and left to set for a period of twenty-four hours. After setting, the mold was removed and the Ir surface was polished to a mirror finish using the following methods. Coarse and fine grinding of the substrate surface was achieved using silicon carbide (SiC) polishing pads (Allied High Tech Products, Inc., Rancho Dominguez, CA, http://www.alliedhightech.com/) with progressively decreasing grit sizes of 60 to 1200. Fine polishing was accomplished with polycrystalline diamond suspensions in various grain sizes from 0.6 µm to 0.1 µm, with a 0.05 µm deagglomerated Al_2O_3 suspension used for the final step. Prior to each experiment, the electrode surface was cleaned with aqua regia for a period of 2 minutes. Ir electrode preparation is illustrated in Figure 5.1. Final preparation of the Ir shot electrode leaves a smooth mirror finished surface which is checked under a Nikon® Eclipse® ME600 optical microscope (Nikon Instruments Inc., Melville, NY, http://www.nikonusa.com/.)

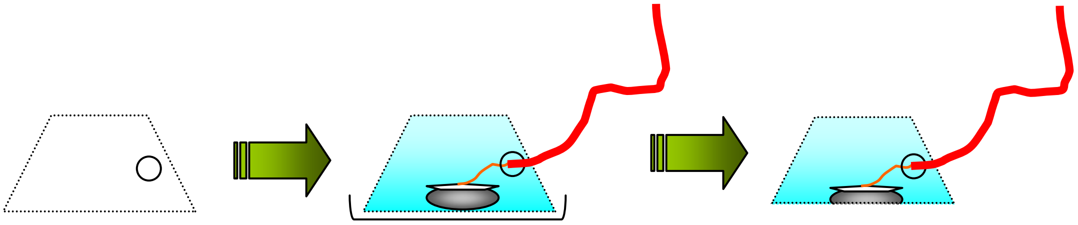

(I) (II) (III)

Figure 5.1 Preparation of Ir shot electrodes where (I)the plastic mold has hole drilled, (II) shot and wire are set in epoxy and covered, and (III) the whole electrode is polished so that Ir has a mirror finish.

Ultrapure water (UPW) was supplied in-house via a Millipore Milli-Q® Elix5® ultrapure water (Millipore Corporation, Bedford, MA, http://www.millipore.com/)

purification system (R>18.2 MΩ/cm) and used in rinsing substrates as well as any dilution of chemicals. High purity Copper Sulfate ($CuSO_4 \cdot 5H_2O$) (Aldrich Chemical Company, Sigma-Aldrich Corporation, St. Louis, MO http://www.sigmaaldrich.com/) and Mallinckrodt sulfuric acid (H_2SO_4) (Mallinckrodt Inc., Hazelwood, MO, http://www.mallinckrodt.com/) were used for plating solutions. For all experiments, solutions were filtered with 0.22 µm sterile micro-filters (Millipore Corporation, Bedford, MA, http://www.millipore.com/). An EG&G Princeton Applied Research model 273A Potentiostat/Galvanostat (PerkinElmer, Inc., Wellesly, MA, http://www.perkinelmer.com/) with a standard three electrode setup and a provisional measure-only mode for open circuit potential (OCP) measurements were used. A conventional three-electrode cell set-up was used containing a Ag/AgCl (3M KCl) reference electrode and a platinum sheet counter electrode. All electrochemistry was done in a Class 100 clean-room hood enclosure (Clean Rooms International, Inc., Grand Rapids, MI, http://www.cleanrooomsint.com/.) A platinum foil counter electrode as well as a standard Model 90-02 Double Junction Ag/AgCl reference electrode (Orion Research Inc. Cummings Cente, Beverly, MA 01915, http://www.orionres.com/) were used. Before each experiment, the reference electrode was rinsed and the outer junction solution (10% KNO_3) was replenished.

Lindberg/Blue M Mini-Mite^{TM} Model TF55035A tube furnace (Lindberg/Blue M, Asheville, NC, http://www.lindbergbluem.com/), fitted with a 16 set-point programmable temperature controller and an upper temperature limit of 1100^{o}C and fitted with a nitrogen purged quartz tube was used to anneal copper deposited Ir (Cu/Ir) samples. The annealed sample was allowed to cool to room temperature under the nitrogen stream while still in the quartz tube.

X-ray Diffraction studies were conducted using a Siemens D500 diffractometer (Siemens AG, Munich Germany, http://www.siemens.com/). The tube source was operated using CuK_α radiation which emit x-rays with wavelengths of 1.54 Å at 40kV and 30 mA. Scans of two theta (2θ) were run at 0.05^o steps and a 1 second dwell time. Peak positions were confirmed against the PDF thumbnail database included in the XRD software. All scanning electron microscope (SEM) images were obtained with a JEOL JSM-T300 electron microscope (JEOL USA, Inc., Peabody, MA, http://www.jeol.com/) with an accelerating voltage of 15-25 kV and a working distance of 30-40 mm. Screen images were photographed with Polaroid® instant photographic film (Polaroid Corporation, Waltham, MA, http://www.polaroid.com/) for permanent records. A Tracor Northern TN5500 series EDX instrument (Thermo Noran, Middleton, WI, (http://www.noran.com/) for elemental analysis, was coupled to the SEM. EDX analyses were done within the energy range of 0 – 10 keV, with a proprietary automatic peak identification software included.

X-ray photoelectron spectroscopy was accomplished using a ESCALAB MKII spectrometer system (Thermo VG Scientific, West Sussex, England, http://www.noran.com/) using a standard Al-K_α X-ray source at 280 watts and electrostatic analysis in constant pass energy mode of 200 eV for survey scans and 20 eV for regional scans.

5. 3 Results and Discussion

Surface studies of Cu/Ir interactions at the sub-monolayer level have been previously reported[19-23]. Metal deposition for these studies was achieved using electron beam evaporation, with all analysis done under UHV conditions. Rearrangement, intermixing and subsurface alloy formation has been observed in Ir/Cu systems of Ir ***on*** Cu[20,22,23]. Interestingly, observations of sub-monolayer deposition of Cu ***on*** Ir (100)-(5x1) have shown some rearrangement of Ir and Cu but with a strict phase separation between Cu and Ir, and no surface alloy formation is observed[19]. In our studies, Cu was electrochemically deposited on Ir polycrystalline electrodes from a 0.1 M sulfuric acid bath with 50 mM $CuSO_4$. A cyclic voltammogram (CV) of an Ir electrode in 0.1 M sulfuric acid bath with 50 mM $CuSO_4$ and a 0.1 M sulfuric acid only background are shown in Figure 5.2.

The open circuit potential (OCP) of a clean virgin Ir surface was measured to be +0.525 V, and was found to be indicative of a clean Ir electrode surface. CVs were run from a starting point at OCP and scanned to -0.6, +1.0 V and returned to OCP. The background CV of Ir in 0.1 M sulfuric acid is shown as the dashed line showing hydrogen evolution beginning circa -250 mV and a hydrogen desorption peak at -220mV on the return scan. The CV of Ir in a 0.1 M sulfuric acid bath with 50 mM

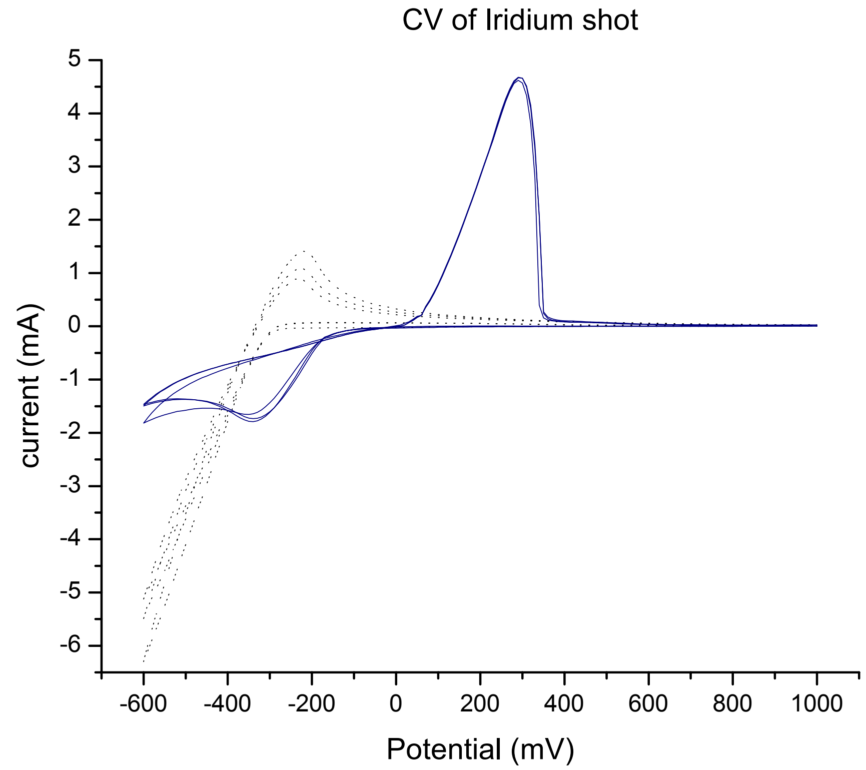

Figure 5.2 CV of Ir shot in 50 mM $CuSO_4$ and 0.1 M H_2SO_4

$CuSO_4$ is depicted as the solid line, where Cu deposition starts at -100 mV with a diffusion-limited Cu deposition peak at -340 mV and hydrogen evolution beginning at -500 mV. There is a Cu stripping peak at +290 mV on the anodic scan. It is of interest to note that the hydrogen evolution from 0.1 M sulfuric does not interfere with the mass transport limited Cu deposition. In order to investigate this phenomenon, linear scans were run in a 0.1 M sulfuric acid bath with 50 mM $CuSO_4$. The scan window started at +0.525 V and were scanned to -0.250 V. The value -0.250 V was chosen for

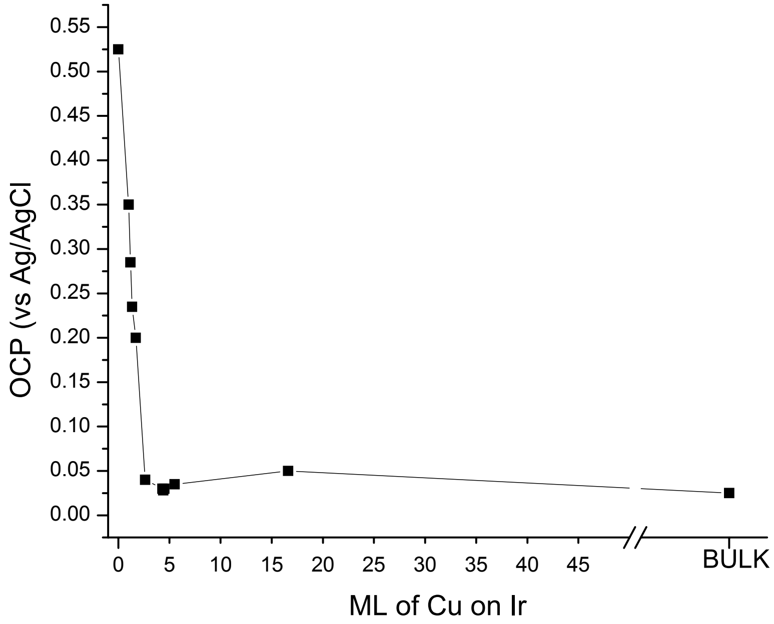

Figure 5.3 OCP vs. ML coverage

the reason that the background CV shows the onset of hydrogen evolution. OCP values graphed against Cu coverage on Ir and bulk Cu are shown in Figure 5.3. These values allow the conclusion to be drawn that the Cu formed at the surface at -250 mV is enough to change the electrochemical characteristics from a purely Ir substrate to a mixed Ir/Cu surface. Calculation of the integrated charge from the anodic stripping peak at +290 mV shows that the Ir surface was covered with approximately 103 MLs of Cu after the first scan. In order to obtain good Cu electrofill, a continuous Cu-seeding layer[24,25] (>7.5 nm) must be deposited over Ta/TaN by physical vapor deposition. New generation diffusion barriers in IC devices should have good adhesion to copper and interlayer dielectrics while providing an efficient, high-quality platform for Cu electroplating, such that good bottom-up electrofill of damascene features can be achieved.

Ir both as solid electrode and thinly deposited substrate on Si has shown itself to be an excellent substrate for Cu electroplating exhibiting strong adhesion of thin continuous Cu films to the Ir surface being able to withstand Scotch-tape peel testing. A sturdy Cu layer is important so that it may survive the harsh production treatment of chemical mechanical polishing (CMP) during the preparation of ICs. XPS analysis seen in Figure 5.4 indicates that Cu electrodeposited on Ir is mostly metallic Cu inline with expectations of plating characteristics in sulfuric acid baths. The separately scanned Cu 2p region in the inset shows the peaks for the $2p_{1/2}$ (952.7 eV) and $2p_{3/2}$ (933 eV) exhibiting normal metallic nature[26].

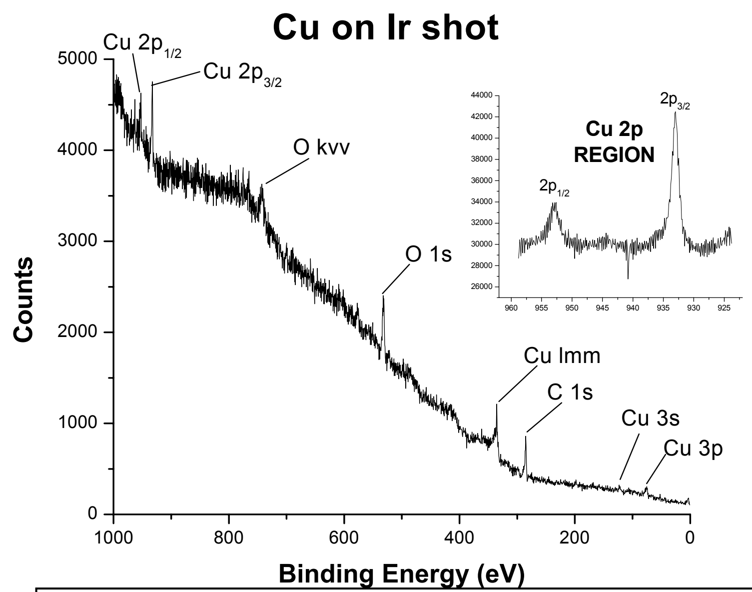

Figure 5.4 XPS of Ir shot electrode with electrodeposited Cu (-400 mV for 10 seconds.)

Cu was electrodeposited on Ir at -450 mV under various times, and surface coverage and anneal effects were obsereved. A 20 second electrodeposition time yielded circa 213 ML of Cu; a 22 second electrodeposition time yielded circa 230 ML

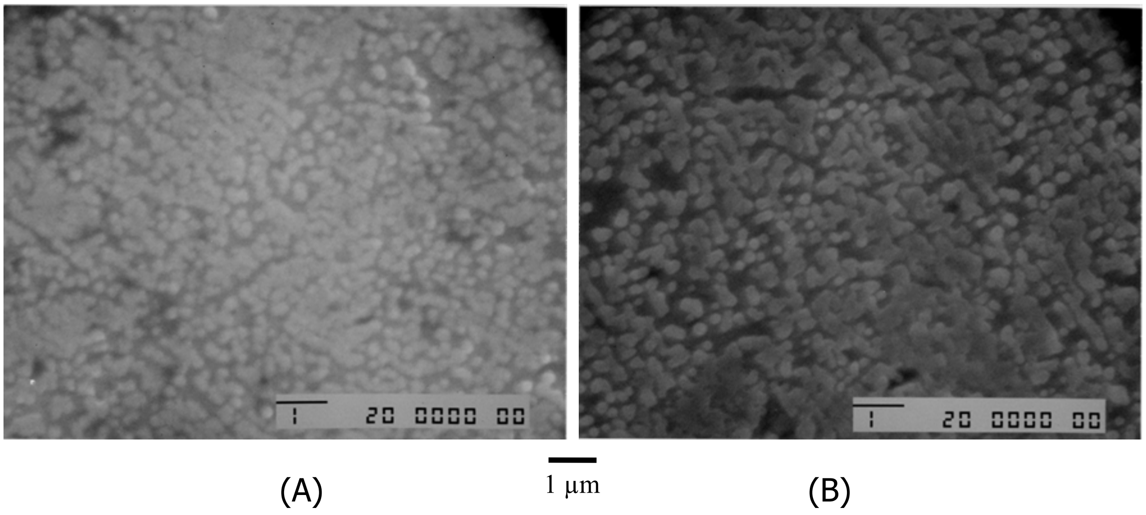

(A) (B)

Figure 5.5 SEM photographs of 20 second Cu deposition on Ir shot (A) not annealed and (B) annealed at 600°C

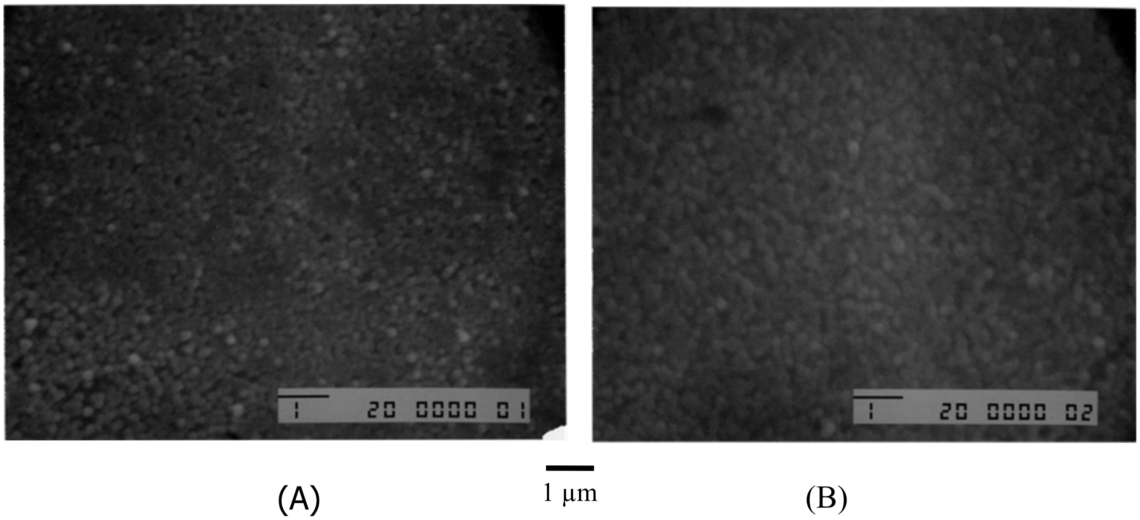

(A) (B)

Figure 5.6 SEM photographs of 22 second Cu deposition on Ir shot (A) not annealed and (B) annealed at 600°C coverage; while a 30 second electrodeposition time gave circa 315 ML coverage. Coverage was calculated from the stripping charge in separate stripping experiments. Cu structures in IC devices need to be stable at normal processing temperatures of 450 °C. SEM images of incomplete surface coverage of Cu on Ir surfaces (SEM Figure 5.5) with no anneal and annealed conditions at 450 ° C show no noticeable change in morphology nor do they show any signs of buckling or dewetting. SEM pictures of a completely covered Ir (SEM Figure 5.6) surface with no annealing show some Cu nuclei on top of a Cu surface. At 600 °C anneal, there is some coalescence of Cu nuclei. The nuclei coalesce and grow in size from an estimated 0.22 μm to 0.37 μm. A surface which has complete coverage (SEM Figure 5.7) with an excess of Cu growth, show a great number of Cu nuclei on a Cu surface. Coalescence of Cu nuclei from an estimated

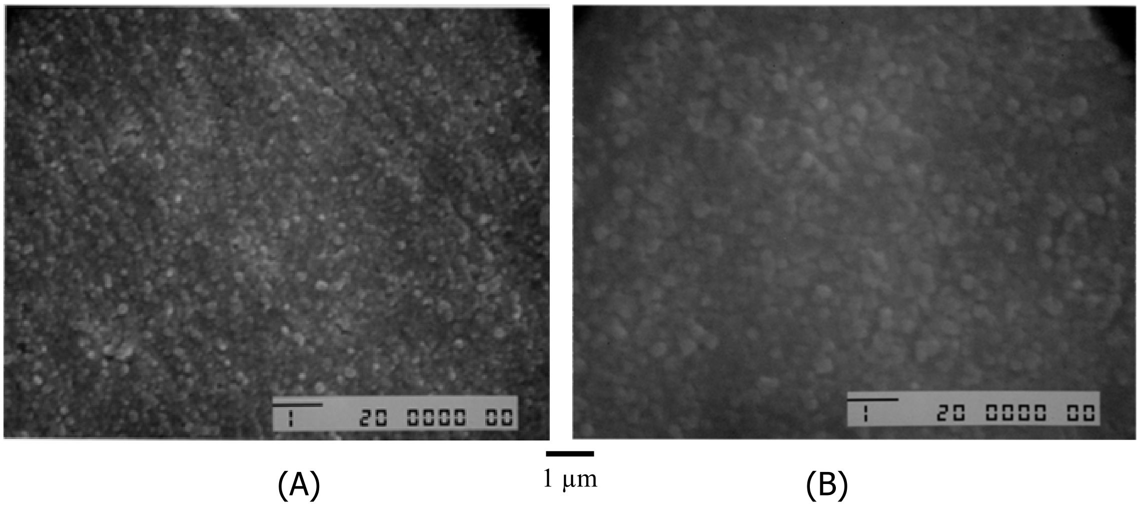

(A) (B)

Figure 5.7 SEM photographs of 30 second Cu deposition on Ir shot (A) not annealed and (B) annealed at 600°C

0.26μm to 0.44μm is shown to occur after anealing at 600^{o}C. These observations are in agreement with XRD observations that show an increase in peak height and sharpness, indicative of grain growth. Most importantly, there are no outward signs of dewetting after annealing and the Cu surface survives a scotch-tape peel test for each stage of coverage after annealing.

XRD characterization of the Cu/Ir samples before and after annealing at various temperatures up to 600 ^{o}C show that the electroplating of Cu on Ir give a preferred Cu(111) structure shown in Figure 5.8. Annealing yields an increase in both peak intensity and sharpness of the XRD peaks expected from the growth of Cu and Ir grains as induced by heating. In particular, the Cu(111) peak shows a sharpening and increase in peak height, indicating a more ordered (111) surface structure taking shape. It is known that a reduction in interfacial defects and improved electromigration reliability of Cu interconnects is available with a more Cu(111) ordered surface. Moreover, the XRD spectra yield **no** new phases or intermetallic compound formation between deposited Cu and the Ir substrate.

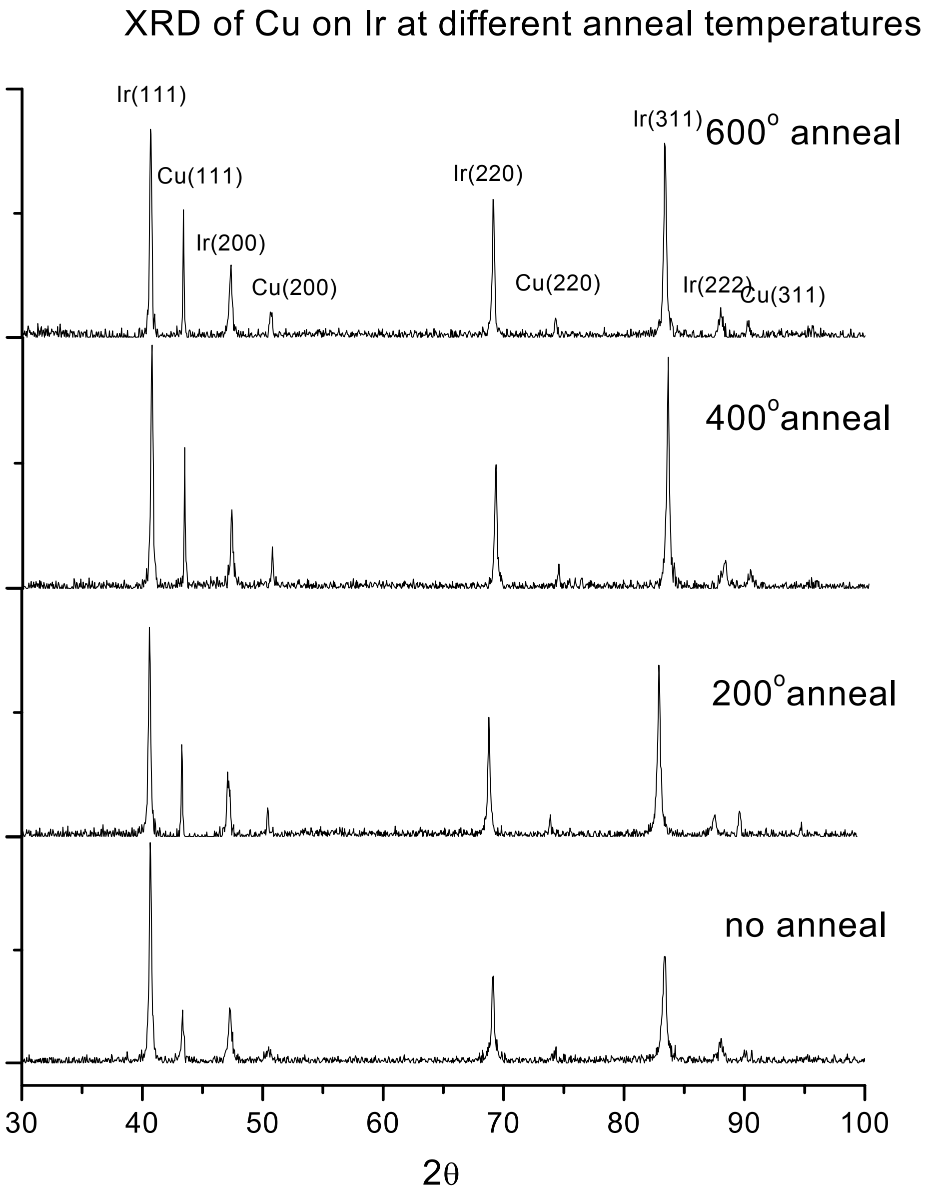

Figure 5.8 XRD data of Electrodeposited Cu on Ir shots.

Also, annealing of Ir shots coated with Cu up to 600 °C under nitrogen atmosphere do not show any signs of de-wetting and XPS analysis still indicates a metallic Cu surface after 600 °C anneal. This is in line with the binary phase diagram for Ir/Cu systems, where an extrapolated 600 °C temperature would show negligible solubility at the aforesaid temperature.

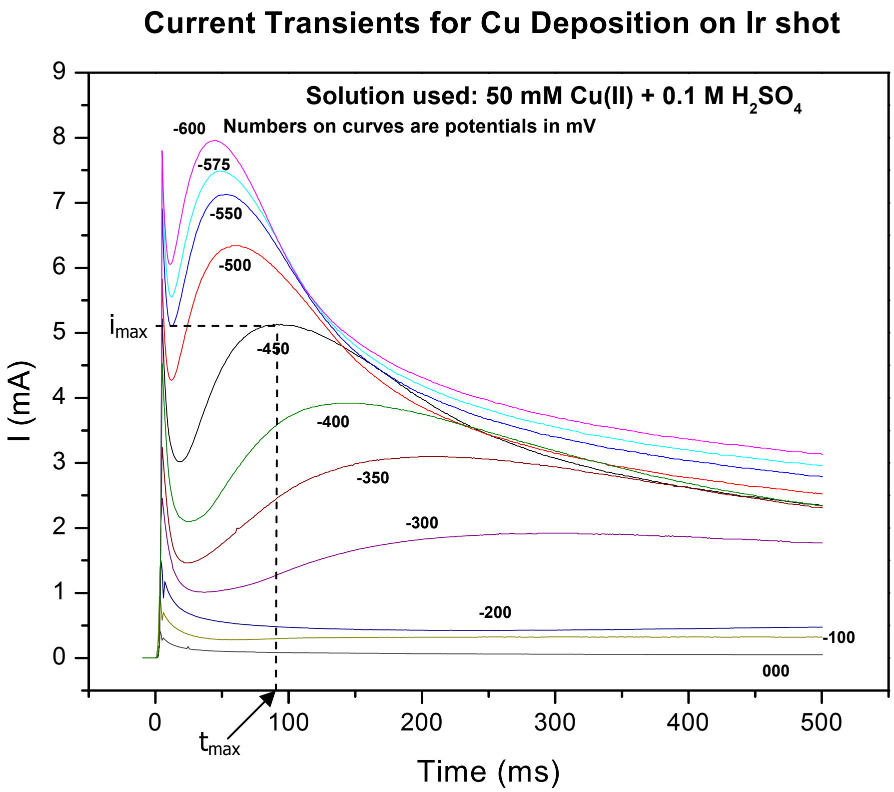

Figure 5.9 Current vs time transients

Chronoamperometry was used in the investigation of initial nucleation of Cu on Ir electrodes. Solutions of 50 mM $CuSO_4$ in 0.1M H_2SO_4 were used. The Ir electrode was held at OCP and stepped to various negative potentials from 0 to –600 mV, thus providing a range of potentials from which the process of nucleation and growth could be observed. Small time frames of less than 2 seconds were used in the study in order to investigate the early stage of electronucleation. Figure 5.9 is representative of a series of current-time transients for Ir electrodes in the Cu plating solution. A diffusion-limited nucleation and growth of metal deposition on a foreign substrate is exhibited by the series of current transients[27-30]. An initial spike due to double layer charging is seen. This is followed by a current rise due to the diffusion limited growth of Cu nuclei until a current maximum (i_{max}) is reached. Following i_{max} there is a decrease in current due to the opposing effect of diffusion zones overlapping near neighboring nuclei. The time (t_{max}) of reaching the current maximum is observed to decrease with the application of more overpotential to accelerate the Cu nucleation process.

Nucleation of metal nuclei on foreign substrates is thought to initiate from surface defect sites such as steps and kinks, where nucleation is thought to be more energetically favorable.

The equation[30]

$$N = N_o\,[1 - \exp(-At)]$$

describes the steady rate of nucleation, where N is the number of nuclei per unit surface, t is at a given time, and N_0 is the maximum number of nucelation sites possible. *A* is the steady state nucleation rate constant, dependant on electrode surface conditions, solution, and overpotential. Early stages of nucleation (where *t* is small) gives rise to two limiting cases for equation [1], instantaneous and progressive nucleation. Instantaneous nucleation occurs when the activation of nucleation sites occurs so quickly such that t=0. In this case *A* has a large value so that $dN/dt = 0$ and $N \cong N_0$. Conversely, progressive nucleation occurs with a considerably slower rate of nucleation, such that for small t values:

$$N \cong A\,N_o\,t$$

where the value for *A* is small, and nucleation is dependant on the nucleation rate constant.

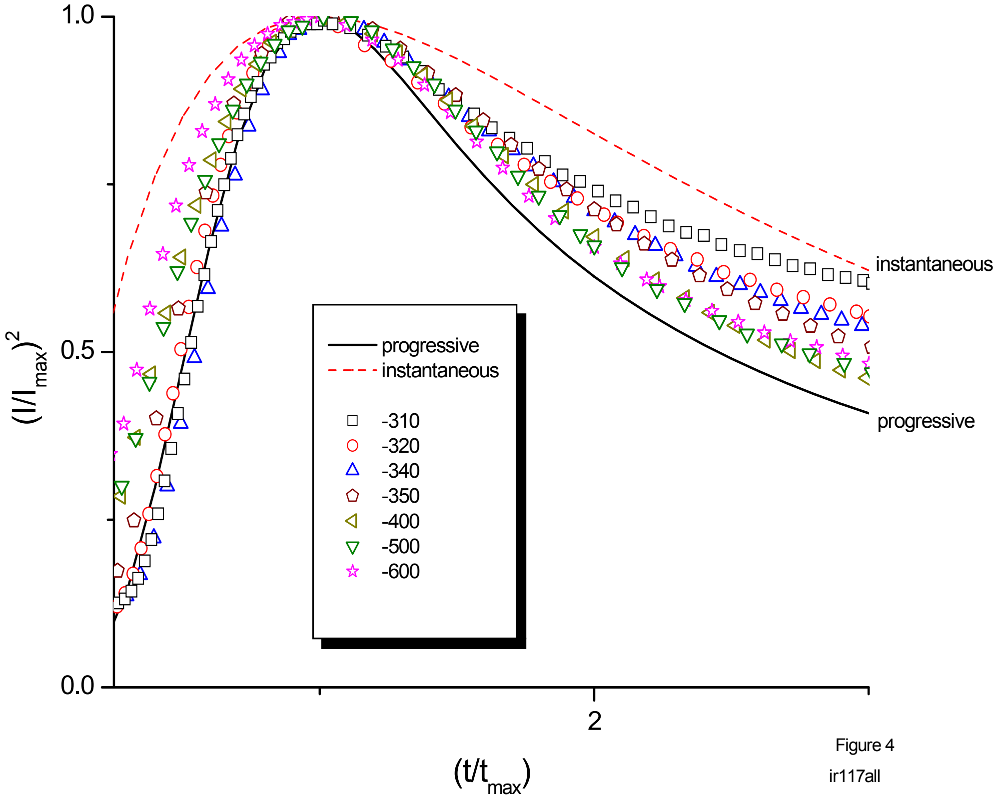

Figure 5.10 Cu nucleation on Ir shot compared to idealized Instaneous and Progressive modes.

Current transients for instantaneous and progressive models can be simulated and normalized as dimensionless time (t/t_{max}) versus current $(i/i_{max})^2$ graphs[28]. Experimental data can then be compared to the two idealized nucleation modes. As shown in Figure 5.10, our data shows that a mixed system of instanteous and progressive nucleation of Cu nuclei occurs on the Ir electrode surface under a negative potential step (-310 to –600 mV) in a 50 mM $CuSO_4$/0.1 M sulfuric acid bath. Some deviations from the theoretical simulation curves were observed from the two regions away from the current peak.

The normalized Ir current transients show a mixed behavior. While showing a tendency for progressive behavior a mixture of progressive/instantaneous behavior is observed. At lower overpotentials (–300 to –400 mV) we observe a progressive tendency at the onset of nucleation where Cu nuclei are being formed. This behavior is followed by a shift towards more instantaneous behavior after the maximum is reached during coalescence and overlapping of the corresponding Cu nuclei. For higher overpotentials (-400 to –600 mV) the converse behavior is observed, with the onset of Cu nucleation deviating much more from progressive nucleation followed by a shift towards a more progressive demeanor after the maximum is reached and coalescence and overlapping of the Cu nuclei occur.

Comparisons can be made to previous data [31] where Cu studies on a Ruthenium (Ru) substrate were conducted. CVs of Ru in sulfuric acid and Cu baths show that Cu electrodeposition onset occurs at -100 mV which is nearly 150 mV less potential than is required for Cu electrodeposition on Ir. Cu deposition and nucleation is not as efficient on Ir than on Ru. A possible explanation for this phenomenon could be the fact that Ru exists in a more efficient crystal structure of hexagonal close packed (hcp) whereas the Ir crystal structure is face centered cubic (fcc). It is possible then for the hcp system to allow for a greater number and more efficient electron transfer to take place across a substrate surface, consequently leading to a more efficient means of eletrodeposition. This discrepancy between Ir and Ru substrates, though, has

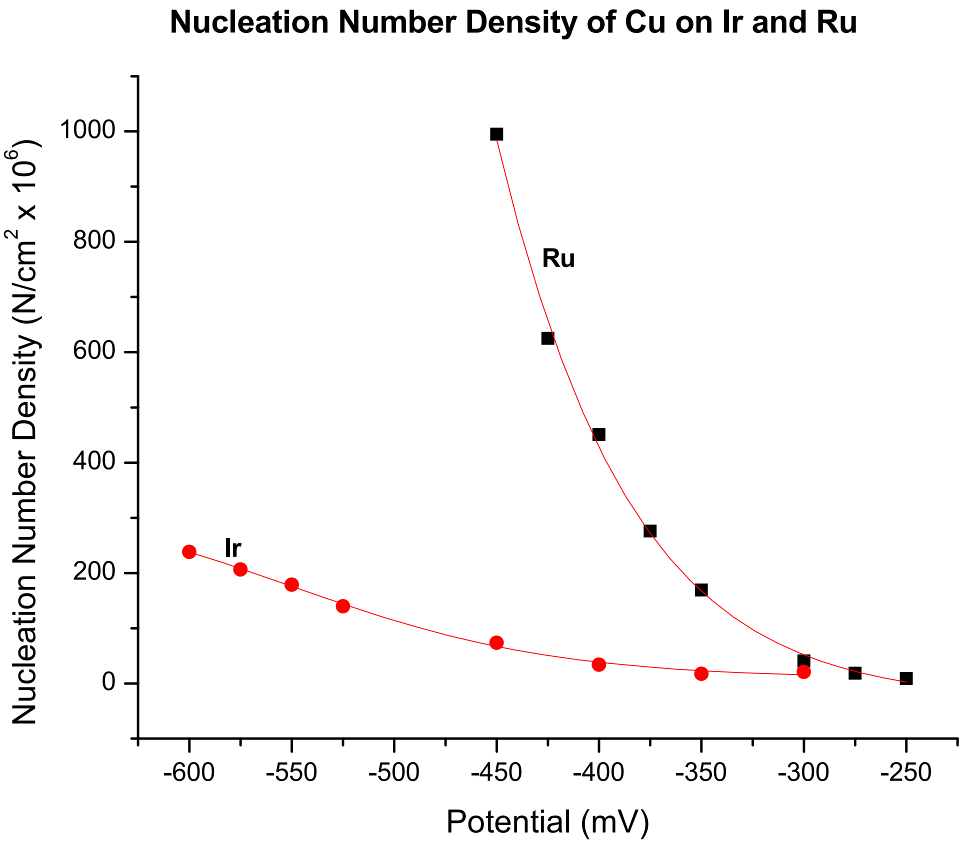

Figure 5.11 Comparison of Nucleation Number Density of Cu electrodeposition on Ir vs Ru

yet to be investigated. Cu nucleation on Ru substrates exhibit a mainly progressive nucleation, as opposed to the mixed nucleation and growth of Cu on Ir substrates. Using a progressive nucleation model, nucleation density of Cu on Ir and from Cu on ruthenium (Ru) data were compared in Figure 5.11. In both cases, there is an increase as the potential is stepped more negative for both Ir and Ru electrodes. Nevertheless, the nucleation number density of Cu on Ir is much less for more negative overpotentials when compared to the Ru electrode. This would be indicative that nucleation rate constant *A* is smaller for Ir than for Ru, where Ru exhibits nearly an order of magnitude more nucleation number density at -450 mV. This comparison is further backed by SEM comparisons of Cu/Ru systems with Cu/Ir systems. Cu deposition in a 50 mM Cu bath on Ru at a 5 second deposition time already show a fully formed continuous film. An Ir electrode with 20 second deposition time in a 50 mM Cu bath still shows a Cu nuclei size of 0.22 μm. Cu deposition on Ru at a 0.5 second deposition time in a bulk Cu plating solution (0.6 M $CuSO_4$) already shows Cu nuclei with an average size of 0.15 μm. The observations indicate that very fast nucleation and growth of Cu on Ru surfaces occurs, while a slower method of nucleation and growth is seen on the Ir/Cu system. Anneal studies with SEM for the Cu/Ru system show that there is no great change in morphology while XRD data merely shows a growth and sharpening of peak intensities, indicative to Cu grain growth, and NO new peak growth is seen. The Ir/Cu system, as shown, does have some coalescence of Cu nuclei, but shows no signs of dewetting and survives a scotch-tape peel test.

5.4 Conclusion

This laboratory is currently in the process of achieving I-V and C-V testing data for more direct and sensitive testing of Cu diffusion barrier performers. Although lacking analysis of current leakage (I-V) and flat-band shifts (C-V) from a metal-oxide-Si test structure, the data thus far substantiates Ir as a likely candidate for future use as a new Cu diffusion barrier. Ir is amenable to direct Cu electroplating with no seed layer needed and allows for precise potential control, important for efficient bottom-up Cu electrofill of dual-damascene features when processing IC devices. XRD data displays a favorable Cu(111) consistency to the electroplated Cu. Furthermore, Cu shows a strong adhesion to Ir surfaces when annealed to 600 ^{o}C. This is an enormous boon if a fabricated Cu interconnect is to have the needed mechanical strength to endure the harsh chemical-mechanical planarization process steps. Overall stability of the Cu/Ir interface at elevated temperatures accentuates the prospect of Ir as an effective Cu diffusion barrier for next generation IC devices.

5.5 References

(1) Takasa, H. *Microelectronic Engineering* **2001**, *59*, 237.

(2) Mikolajick, T.; Dehm, C.; Hartner, W.; Kasko, I.; Kastner, M. J.; Nagel, N.; Moert, M.; Mazure, C. *Microelectronics Reliability* **2001**, *41*, 947.

(3) Minamikawa, T.; Yonezawa, Y.; Heya, A.; Fujimori, Y.; Nakamura, T.; Masuda, A.; Matsumura, H. *Thin Solid Films* **2001**, *395*, 284.

(4) Lee, K. B.; Desu, S. B. *Current Applied Physics* **2001**, *1*, 379.

(5) Lundstrom, I.; Spetz, A.; Winquist, F.; Ackelid, U.; Sundgren, H. *Sensors and Actuators* **1990**, *B1*, 15.

(6) Lalinsky, T.; Breza, J.; Vogrincic, P.; Osvald, J.; Mozolova, Z.; Sisolak, J. *Solid State Electronics* **1998**, *42*, 205.

(7) Nakamura, T.; Nakao, Y.; Kamisawa, A.; Takasu, H. *Japanese Journal of Applied Physics* **1994**, *33*, 5207.

(8) Jeon, Y.; Seon, J.; Joo, J.; Oh, K.; Roh, J.; Kim, D. *Applied Physics Letters* **1997**, *71*, 469.

(9) *Binary Alloy Phase Diagrams*; Second ed.; Materials Information Society:, 1990; Vol. 2.

(10) Hall, R. N.; Racette, J. H. *Journal of Applied Physics* **1964**, *35*, 379.

(11) Sparks, D. R.; Dayananda, M. A. *"The behavior of transition metals in silicon during annealing transients" Defect and Diffusion Forum* **1988**, *39*, 77.

(12) Wu, P. K.; Yang, G. R.; Lu, T. M. *Appl. Phys. Lett.* **1994**, *65*, 508.

(13) Pallean, J.; Oberline, J. C.; Braud, F.; Torres, J.; Mermet, J. L.; Mouche, M.; Ermolieff, A. *J. Mat. Res. Soc. Proc.* **1994**, *337*, 225.

(14) Stavrevm, J. M.; Fischer, D. C. W.; Drescher, K. M., N. *Thin Solid Films* **1997**, *307*, 79.

(15) Kaloyeros, A. E.; Chen, X.; Stark, T.; Kumar, K.; Seo, S. C.; Peterson, G. G.; Frisch, H. L.; Arkles, B.; Sullivan, J. *Journal of The Electrochemical Society* **1999**, *146*, 170.

(16) Radisic, A.; Long, J. G.; Hoffmann, P. M.; Searson, P. C. *Journal of The Electrochemical Society* **2001**, *148*, C41.

(17) Oskam, G.; Vereecken, P. M.; Searson, P. C. *Journal of The Electrochemical Society* **1999**, *146*, 1436.

(18) Takahashi, K. M. *Journal of the Electrochemical Society* **2000**, *147*, 1414.

(19) Gilarowski, G.; Mendez, J.; Niehus, H. *Surface Science* **2000**, *448*, 290.

(20) Gilarowski, G.; Niehus, H. *Surface Science* **1999**, *436*, 107.

(21) Cho, L. H.; Lee, J. I. *Journal of Korean Physical Society* **1999**, *35*, L299.

(22) Gilarowski, G.; Niehus, H. *physica status solidi (a)* **1999**, *173*, 159.

(23) Heinze, S.; Bihlmayer, G.; Blugel, S. *physica status solidi (a)* **2001**, *187*, 215.

CHAPTER 6

CONCLUSION

This chapter will serve to highlight conclusions and observations from the previous chapters as well as present some initial observations for ongoing work in which this researcher has had the honor to participate.

6.1 Conclusions from Chapters

6.1.1 Si(111) FTIR-ATR studies

Chapter 2 showed studies of passivated Si(111) in UPW by multiple internal reflection infrared spectroscopy. Microscopically rough and monohydride terminated Si(111) surfaces are studied in various UPW. It is found that the dihydride site of the Si(111) surface is the most susceptible to chemical attack, with monohydride and trihydride showing reasonable stability over 120 minutes. Metal contamination is seen to increase the rate of loss for hydrogen passivation on a Si surface, by allowing a more effective rate of electron transfer from the bulk Si to the surface, eventually leading to oxidation of the Si substrate. Dissolved oxygen in ultra-pure water is seen to play a role on the etching and subsequent oxidation of microscopically rough and monohydride terminated Si surface: i) by allowing for a more amenable arrangement for the etching of the hydride surface by water, and ii) by being present in the insertion of backbonded surface oxides. Bubbled nitrogen seems to play a physical role by perturbation of the water molecules such that preferential etching of dihydride sites is prevented.

6.1.2 Si Based Potentiometric Sensor in UPW

Chapter 3 served to illustrate the use of a Si based potentiometric sensor for the detection of ultra-trace metal ion contaminants of Ag and Cu in UPW. The shift from using HF acidic media to sensing directly in UPW is a boon since this eliminates the need for contact with dangerous materials. Using open circuit potential measurements, a parts-per trillion level of detection is able to be established. This could serve industrial purposes where maintaining an ultra-pure water supply is critical (i.e. pharmaceutical and microelectronics industries.)

6.1.3 Electroless Pd and Pt on PPF

Chapter 4 dealt with the production of electrolessly deposited Pd and Pt nanoparticles of thin film carbon in the form of pyrolyzed photoresist films. The deposition time, HF strength and metal ion concentration were investigated to provide a more stable metal/PPF substrate. The metal deposited PPF substrates exhibit catalytic properties for hydrogen evolution, and $[Ru(NH_3)_6)]^{3+/2+}$ Redox electrochemistry using dopamine and Formaldehyde catalysis showed mixed results. Further studies on the conditions of metal deposition & concentration, HF strength, and depositions times as well as a gamut of redox couples could provide a stronger picture into the workings of this system. It would also be of interest to study mixed deposition of Pd/Pt particles on PPF substrates.

6.1.4 Ir as a Cu Diffusion Barrier

Cu electrodeposition and thin film characterization on Ir was explored. Annealing of the Cu/Ir samples was also accomplished up to 600 ^{o}C in a N_2 atmosphere. It is observed that Cu can electroplate directly onto Ir and shows good adhesion. A preferred (11) phase is seen with XRD and no intermixing is observed. These characteristics make Ir a likely candidate for further investigation as a likely Cu diffusion barrier. Further studies with XPS and TOF-SIMS investigation would greatly enhance the picture.

6.2 Continuing Endeavors

6.2.1 Ru/RuOx

Initial studies into the characterization of Ru and RuO_2 have been conducted. The importance of Ru and RuO_2 lies in the hope that it is seen to be a very good potential candidate for next generation Cu interconnect diffusion barrier technology.

Various Ru and RuO_2 substrates have been explored. All X-ray photoelectron spectroscopy analysis was accomplished using the ESCALAB MKII spectrometer system (Thermo VG Scientific, West Sussex, England, http://www.noran.com/) using a standard Al-K_α X-ray source at 280 watts and electrostatic analysis in constant pass energy mode of 200 eV for survey scans and 20 eV for regional scans. Figure 6.1 shows the survey scan for a Ru film on Si. Ruthenium on Si samples were graciously donated by Texas Instruments, Inc.

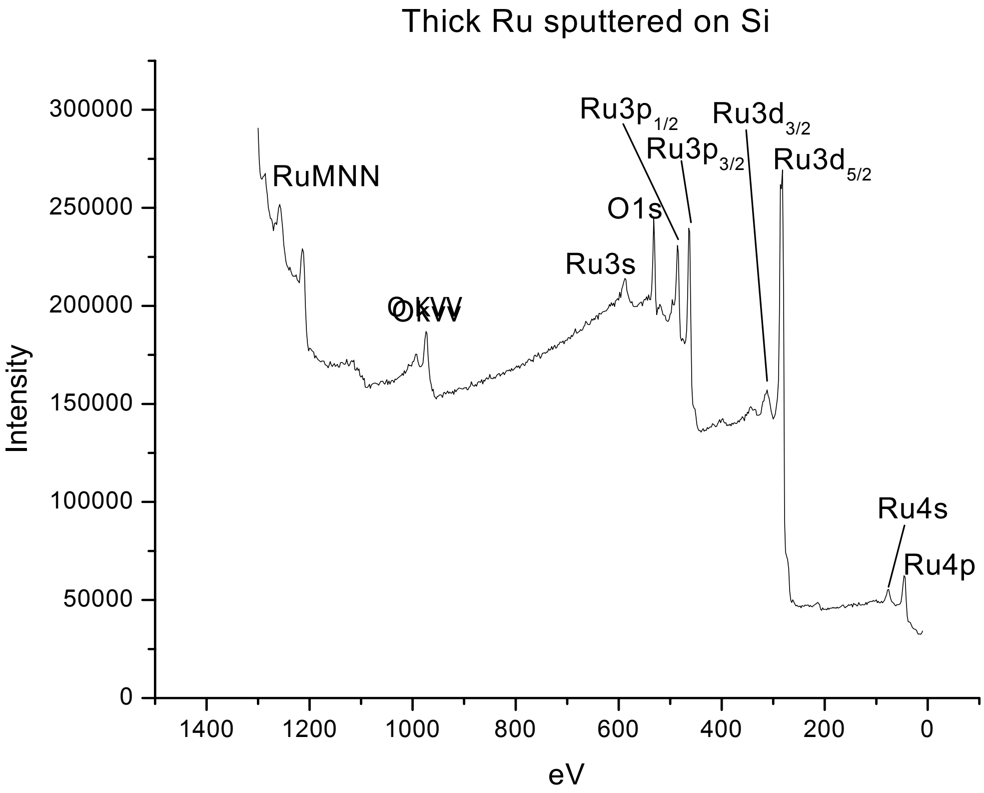

Figure 6.1 XPS survey scan of a Ru sputtered Si substrate.

The survey scan shows that the Ru substrate has a thickness that obscures the Si signal. In this case, the absence of the Si signal is a moot point since at this juncture we are mainly interested in Ru characterization.

Ru substrates were subjected to various conditions to observe its oxidation state. The conditions include:

- Argon ion sputtering was run inside the analytical chamber of the XPS analyzer in an attempt to obtain a ‘cleaner’ surface,
- Thermal heating at 300°C in both oxygen and hydrogen were accomplished,

- Electrochemical oxidation by holding at +1.1 V and +1.3 V for 3 minutes.

A ruthenium oxide pellet disk was also formed by hydraulic compression of powdered RuO_2.

Figure 6.2 shows the Ru 3d region for treated Ru surfaces. Table 6.1 shows the value of peak positions for the different peaks taken from regional scans on the Ru surfaces. It is most interesting to note that electrochemical and thermal attempts to oxidize the surface all show an expected shift toward higher binding energy levels. There is no great change in the shape of the Ru 3d peaks when comparing treatments. Figure 6.3 shows the O 1s region for treated Ru surfaces. The position of the O 1s binding energy peak shifts from what may be considered physisorbed oxygen species on the surface of Ru to lower binding energy values of RuO_2 species. The shape of the O 1s peak also changes from a somewhat symmetrical curve to a shifted curve with a shoulder occurring at circa 532 eV.

Sample	Ru3d3/2	Ru3d5/2	O1s
RuO2 Pellet	285	280.9	529.6
+1.1V Oxidation	284.6	280.7	530.4
+1.3 V Oxidation	284.6	280.7	530.5
Ru O2 heated 350C 1 hour	284.4	280.3	529.6
Ru/Ar sputtered	284.1	279.9	N/A
Ru no treatment	284.3	280.1	530.9
Ru H2 heating 350C 30 min	284.3	280	530.2
+1.3 V Oxidation / H2 heating	284.2	280.1	530.3

Table 6.1 Binding Energy Peak Positions for Regional Scans

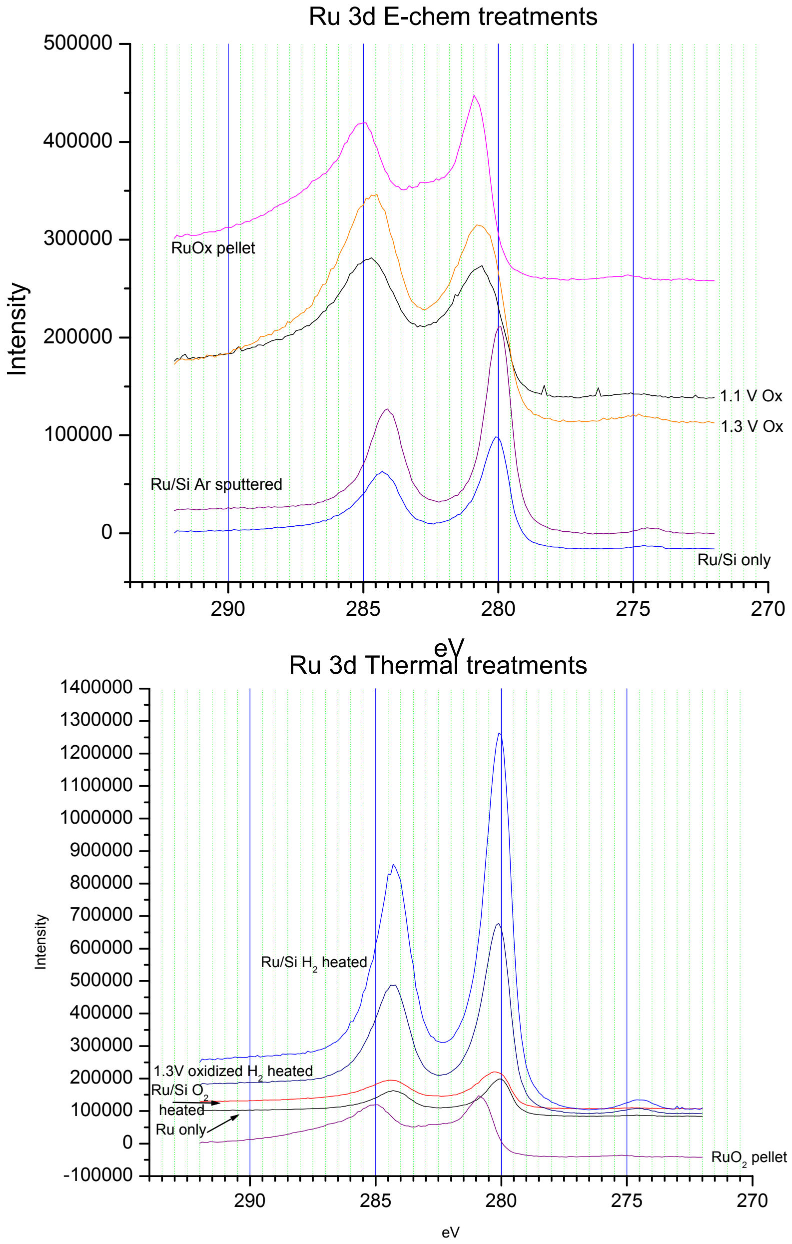

Figure 6.2 XPS regional scans of Ru3d regions

Consequently, as the can be seen by the XPS data on the table and figures, it may be surmised that the change in peak shape and shift of O 1s to lower binding energies can be used as a good indicator for the determination oxidation of Ru surfaces.

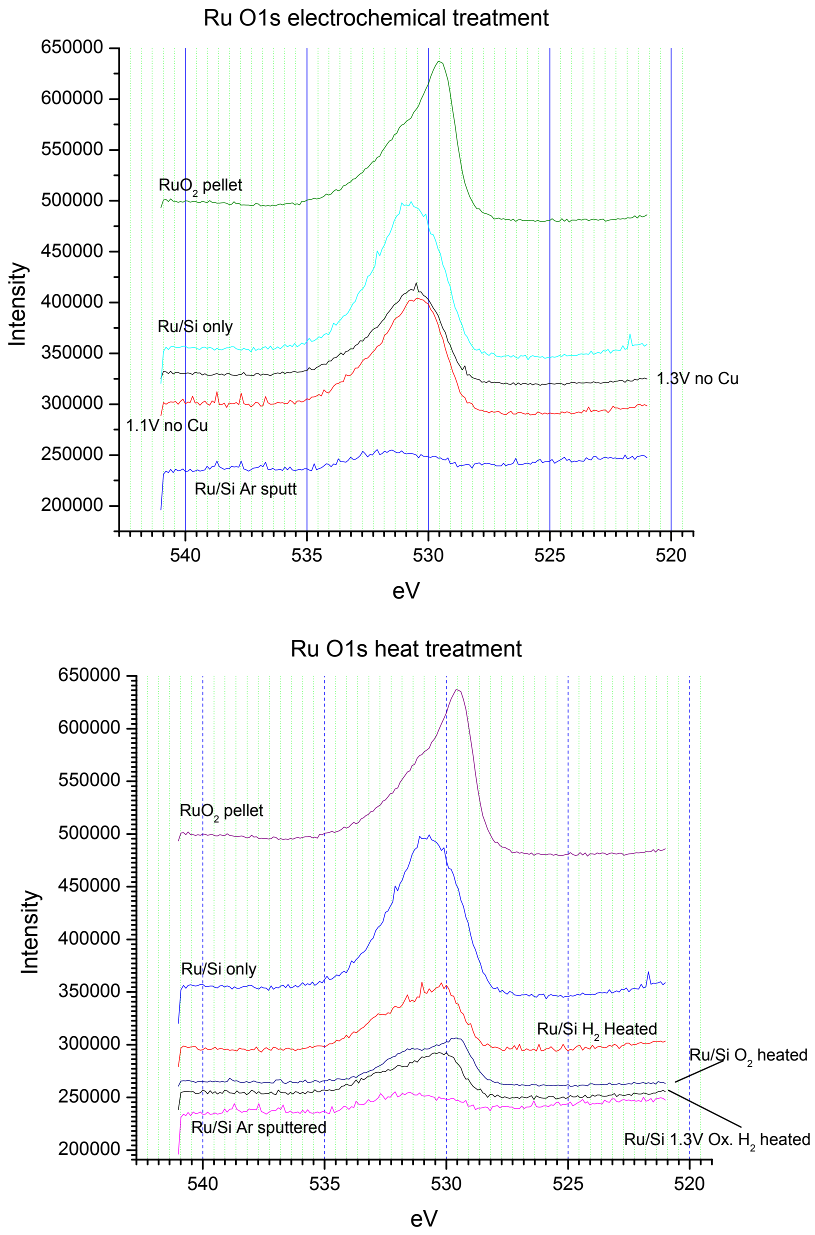

Figure 6.3 XPS regional scans of O1s regions

This set of data is in agreement with previously conducted studies[1-4] and provides a suitable foundation from which research may be done to explore the oxidation of Ru. This is especially important for the exploration for new generation Cu diffusion barriers. In order for a suitable barrier to be explored, there must be some foundation laid out by which research may proceed.

6.2.2 Direct Cu electroplating on Ru

Direct electroplating of Cu on Ru thin films has also been investigated and initial findings have been reported[5]. Copper was directly electroplated onto a thinly sputtered Ru thin film (~20 nm – verified by tunneling electron microscopy, courtesy of Dr. Moon Kim, University of North Texas, Materials Science Department) on Si substrates. Characterization of the substrates system reveals that Cu can be directly plated onto a Ru thin film and, as shown in Figure 6.4, survives a scribe-peel test for adhesion.

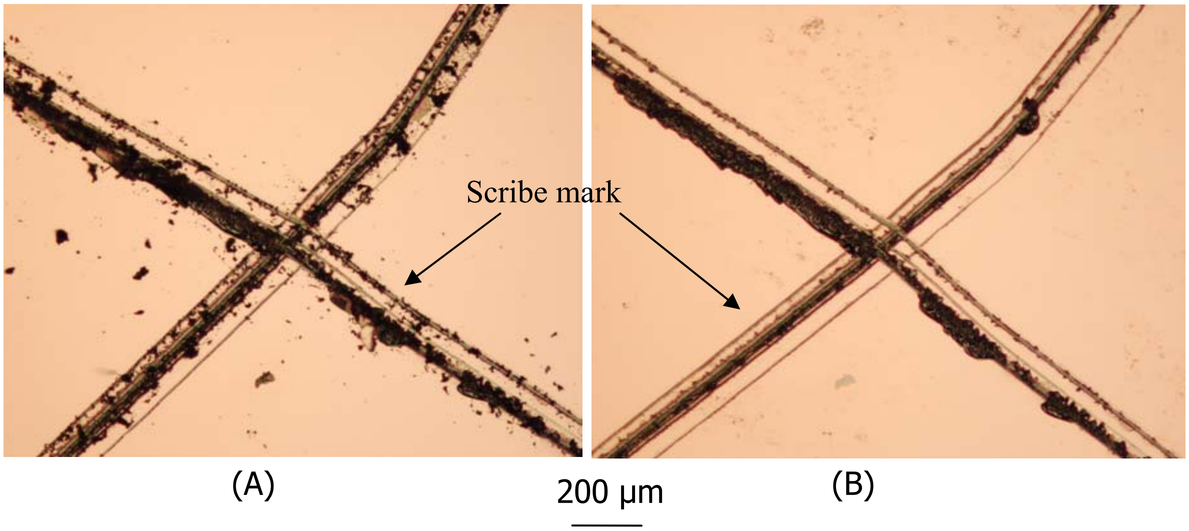

Figure 6.4 Optical microscopy photograph of Cu on Ru/Si substrate scribed with diamond tipped scriber - before and after tape peel test for adhesion.

Most importantly, backside SIMS depth profiling (performed by Charles Evans and Associates, Surface and Micro Analysis,) has also shown the interfacial stability between Cu/Ru(20nm)/Si after annealing at 450 °C. The interfacial structure shows a sharp, defined interface before and after 450°C anneal. Breakdown of the barrier is seen to occur after 550°C anneal.

6.3 Conclusion

It is hoped that the reading of this dissertation will have piqued the curiosity of the reader and illustrated the breadth and scope of the work contained herein. It is due in no small part to the kindness and patience of others that this work has been accomplished. The work of discovery comes not only from within, but also comes from healthy discourse and relationships with others.

6.4 References

(1) Hrbek, J. *Journal of Vacuum Science and Technology (A)*, *13*, 1409.

(2) Kim, K. S.; Baitinger, W. E.; Amy, J. W.; Winograd, N. *Journal of Electron Spectroscopy and Related Phenomena* **1974**, *5*, 351.

(3) Lewerenz, H. J.; Stucki, S.; Kotz, R. *Surface Science* **1983**, *126*, 463.

(4) Chan, H. Y. H.; Takoudis, C. G.; Weaver, M. J. *Journal of Catalysis* **1997**, *172*, 336.

(5) Chan, R.; Arunagiri, T. N.; Zhang, Y. B.; Chyan, O. M. R.; Wallace, R. M.; Kim, M. J.; Hurd, T. Q. *accepted for publication in: Electrochemical and Solid State Letters* **2003**.

COMPLETE REFERENCE LIST

(In Alphabetical Order)

Binary Alloy Phase Diagrams; Second ed.; Materials Information Society:, 1990; Vol. 2.

In *Filtration Industry Analyst*, 2003; Vol. 2003, p 14.

Ahmadi, T. S.;X. L. Wang;A. Henglein;M. A. El-Sayed *Chemistry of Materials* 1996, *8*, 1161.

Anjo, D. M.;M. Karh;M. M. Khodabaksh;S. Nowinski;M. Wanger *Analytical Chemistry* 1989, *61*, 2603.

Arunagiri, T. *Interfacial Electrochemistry of Metal Nanoparticles on Diamond and Copper Electroplating on Ruthenium Surface - Dissertation*; University of North Texas: Denton, 2003.

Boonekamp, E. P.;J. J. Kelly *Journal of Applied Physics* 1994, *75*, 8121.

Cabanis, G. E.;A. A. Diamantis;W. R. Murphy Jr.;R. W. Linton;T. J. Meyer *Journal of the American Chemical Society* 1985, *107*, 1845.

Chan, H. Y. H.;C. G. Takoudis;M. J. Weaver *Journal of Catalysis* 1997, *172*, 336.

Chan, R.;T. N. Arunagiri;Y. B. Zhang;O. M. R. Chyan;R. M. Wallace;M. J. Kim;T. Q. Hurd *accepted for publication in: Electrochemical and Solid State Letters* 2003.

Chang, R. *Chemistry*; Fourth ed.; McGraw-Hill: New York, 1991.

Chen, P.;R. L. McCreery *Analytical Chemistry* 1996, *68*, 3958.

Cho, L. H.;J. I. Lee *Journal of Korean Physical Society* 1999, *35*, L299.

Chyan;J.-J. Chen;F. Xu;J. A. Sees;L. H. Hall *The Analyst* 2000, *125*, 175.

Chyan, O.;J.-J. Chen;J. Wu;S. Chien;M. Liu In *Electrochemical Synthesis and Modification of Materials*; P. C. Andricaco, S. G. Corcoran, J.-L. Delplancke, T. P. Moffat,P. C. Searson, Eds.; Materials Research Society: Pittsburgh, 1997; Vol. 451, pp 267.

Chyan, O. M. R.;J.-J. Chen;L. Chen;F. Xu *Journal of The Electrochemical Society* 1997, *144*, L17.

Chyan, O. M. R.;J.-J. Chen;H.-Y. Chien *Journal of The Electrochemical Society* 1996, *143*, 92.

Chyan, O. M. R.;J.-J. Chen;H.-Y. Chien;J. J. Wu;M. Lie *Journal of The Electrochemical Society* 1996, *143*, L235.

Clark, J. K.;W. A. Schilling;C. A. Wijayawardhana;P. R. Melaragano *Analytical Chemistry* 1994, *66*, 3528.

Cotton, F. A.;C. Murillo *Advanced Inorganic Chemistry*; John Wiley & Sons: New York, 1999.

Cox, J. A.;M. E. Tess;T. E. Cummings *Reviews of Analiytical Chemistry* 1996, *15*, 173.

Gao, J.-S.;T. Arunagiri;J.-J. Chen;P. Goodwill;O. Chyan *Chemistry of Materials* 2000, *12*, 3495.

Gilarowski, G.;J. Mendez;H. Niehus *Surface Science* 2000, *448*, 290.

Gilarowski, G.;H. Niehus *Surface Science* 1999, *436*, 107.

Gilarowski, G.;H. Niehus *physica status solidi (a)* 1999, *173*, 159.

Goldstein, J. I.;D. E. Newbury;P. Echlin;D. C. Joy;A. D. Romig;C. E. Lyman;C. Fiori;E. Lifshin *Scanning Electron Microscopy and x-ray microanalysis: a text for biologists, materials scientists, and geologists*; Second Edition ed.; Plenum Press: New York, 1992.

Gräf, D.;M. Grundner;R. Schulz *Journal of Vacuum Science and Technology A* 1989, *7*, 808.

Gullon, J. S.-┬ . ;V. Montiel;A. Aldaz;J. Clavilier *Electrochemistry Communications* 2002, *4*, 716.

Gurrath, M.;T. Kuretzky;H. P. Boehm;L. B. Okhlopkova;A. S. Lisitsyn;V. A. Likholobov *Carbon* 2000, *38*, 1241.

Hall, R. N.;J. H. Racette *Journal of Applied Physics* 1964, *35*, 379.

Harrick, N. J. *Internal Reflection Spectroscopy*; John Wiley & Sons, Inc.: New York, 1967.

Heinze, S.;G. Bihlmayer;S. Blugel *physica status solidi (a)* 2001, *187*, 215.

Heyns, M. M.;R. J. Nemanich In *Properties of Crystalline Silicon*; 1 ed.; R. Hull, Ed.; INSPE, The Institution of Electrical Engineers: London, 1998; Vol. 20, p 219.

Higashi, G. S.;Y. J. Chabal;G. W. Trucks;K. Raghavachari *Applied Physics Letters* 1990, *56*, 656.

Homma, T.;C. P. Wade;C. E. D. Chidsey *The Journal of Physical Chemistry B* 1998, *102*, 7919.

Hrbek, J. *Journal of Vacuum Science and Technology (A)* van Campen, D.G.

Malik, I.J., *13*, 1409.

James, R. W. *X-RAY CRYSTALLOGRAPHY*; Fifth ed.; Butler and Tanner LTD.: London, 1962.

Jenkins, G.;K. Kawamura *Polymeric Carbons-Carbon Fibre, Glass and Char*; Cambridge University Press: Cambridge, England, 1976.

Jenkins, G. M.;K. Kawamura *Polymeric carbons - carbon fibre, glass and char*; Cambridge University Press: Cambridge, 1976.

Jeon, Y.;J. Seon;J. Joo;K. Oh;J. Roh;D. Kim *Applied Physics Letters* 1997, *71*, 469.

Kaloyeros, A. E.;X. Chen;T. Stark;K. Kumar;S. C. Seo;G. G. Peterson;H. L. Frisch;B. Arkles;J. Sullivan *Journal of The Electrochemical Society* 1999, *146*, 170.

Kasap, S. O. *Principles of electronic Materials and Devices*; McGraw Hill: New York, 2002.

Kim, J.;X. Song;K. Kinoshita;M. Madou;R. White *Journal of the Electrochemical Society* 1998, *145*, 2314.

Kim, K. S.;W. E. Baitinger;J. W. Amy;N. Winograd *Journal of Electron Spectroscopy and Related Phenomena* 1974, *5*, 351.

Kinoshita, K. *Carbon: electrochemical and physiochemical properties*; Wiley Interscience: New York, 1988.

Klug, H. P.;L. E. Alexander *X-RAY DIFFRACTION PROCEDURES: For Polycrystalline and Amorphous Materials*; Second ed.; Wiler-Interscience: New York, 1974.

Kniffin, M. L.;T. E. Beerling;C. R. Helms *Journal of The Electrochemical Society* 1992, *139*, 1195.

Kostecki, R.;X. Song;K. Kinoshita *Electrochemical and Solid-State Letters* 1999, *2*, 465.

Kuo, T.-C.;R. L. McCreery *Analytical Chemistry* 1999, *71*, 1553.

Lalinsky, T.;J. Breza;P. Vogrincic;J. Osvald;Z. Mozolova;J. Sisolak *Solid State Electronics* 1998, *42*, 205.

Lee, K. B.;S. B. Desu *Current Applied Physics* 2001, *1*, 379.

Lee, S.-B.;S.-I. Pyun *Journal of Applied Electrochemistry* 2000, *30*, 795.

Lewerenz, H. J.;S. Stucki;R. Kotz *Surface Science* 1983, *126*, 463.

Lim, S. W.;R. T. Mo;P. A. Pianetta;C. E. D. Chidsey *Journal of The Electrochemical Society* 2001, *148*, C16.

Liu, S.;Z. Tang;E. Wang;S. Dong *Electrchemistry Communications* 2000, *2*, 800.

Lundstrom, I.;A. Spetz;F. Winquist;U. Ackelid;H. Sundgren *Sensors and Actuators* 1990, *B1*, 15.

Makkee, M.;A. Wiresma;E. J. A. X. can de Sandant;H. van Bekkum;J. A. Moulijn *Catalysis Today* 2000, *55*, 125.

Mikolajick, T.;C. Dehm;W. Hartner;I. Kasko;M. J. Kastner;N. Nagel;M. Moert;C. Mazure *Microelectronics Reliability* 2001, *41*, 947.

Minamikawa, T.;Y. Yonezawa;A. Heya;Y. Fujimori;T. Nakamura;A. Masuda;H. Matsumura *Thin Solid Films* 2001, *395*, 284.

Morita, M.;T. Ohmi;E. Hasegawa;M. Kawakami;K. Suma *Applied Physics Letters* 1989, *56*, 562.

Morrison, S. R. *Journal of Applied Physics* 1982, *53*, 1233.

Nakamura, T.;Y. Nakao;A. Kamisawa;H. Takasu *Japanese Journal of Applied Physics* 1994, *33*, 5207.

Niwa, O.;H. Tabel *Analytical Chemistry* 1994, *66*, 285.

Niwano, M.;M. Terashi;M. Shinohara;D. Shoji;N. Miayamoto *Surface Science* 1998, *401*, 364.

Ohmi, T.;T. Imaoka;I. Sugiyama;T. Kesuka *Journal of The Electrochemical Society* 1992, *139*, 3317.

Oskam, G.;P. M. Vereecken;P. C. Searson *Journal of The Electrochemical Society* 1999, *146*, 1436.

Ozaki, J.;W. Ohizumi;A. Oya;M. J. Illan-Gomez;M. C. Raman-Martinez;A. Linares-Solano *Carbon* 2000, *38*, 775.

Pallean, J.;J. C. Oberline;F. Braud;J. Torres;J. L. Mermet;M. Mouche;A. Ermolieff *J. Mat. Res. Soc. Proc.* 1994, *337*, 225.

Parsons, R.;T. VanderNoot *Journal of Electroanalytical Chemistry* 1988, *257*, 9.

Peitch, G. J.;U. Köhler;M. Henzler *Chemical Physics Letters* 1992, *197*, 346.

Ponnuswamy, T.;J.-J. Chen;X. Fei;O. Chyan *Analyst* 2001, *126*, 877.

Radisic, A.;J. G. Long;P. M. Hoffmann;P. C. Searson *Journal of The Electrochemical Society* 2001, *148*, C41.

Ranganathan, S.;R. L. McCreery *Analytical Chemistry* 2001, *73*, 893.

Ranganathan, S.;R. L. McCreery;S. M. Maiji;M. Madou *Journal of the Electrochemical Society* 2000, *147*, 277.

Ray, K.;R. L. McCreery *Analytical Chemistry* 1997, *69*, 4680.

Rotondaro, A. L. P.;T. W. Hurd;H. F. Schmidt;I. Teerlinck;M. M. Heyns;C. Claeys In *Ultraclean Semiconductor Processing Technology*

and Surface Chemical Cleaning and Passivation; M. Lieh, M. Heyns, M. Hirose,H. Parks, Eds.; Materials Research Society: Pittsburgh, 1995; Vol. 386, p 183.

Rotondaro, A. L. P.;T. W. Hurd;H. F. Schmidt;I. Teerlinck;M. M. Heyns;C. Claeys In *Ultraclean Semiconductor Processing Technology*

and Surface Chemical Cleaning and Passivation; M. Lieh, M. Heyns, M. Hirose,H. Parks, Eds.; Materials Research Society: Pittsburgh, 1995; Vol. 386, pp 183.

Runyan, W. R.;K. E. Bean *Semiconductor Integrated Circuit Processing Technology*; Addison-Wesley Publishing Company: Reading, 1990.

Sands, D. E. *Introduction to Crystallography* New York, 1969.

Sasaki, Y. C.;M. Mitsuya *Langmuir* 1995, *11*, 3446.

Serway, R. A. *Physics for Scientists & Engineers with Modern Physcs*; Third ed.; Saunders College Publishing: Philadelphia, 1990.

Sherstyuk, O. V.;S. N. Pron'kin;A. L. Chuvlin;A. N. Salanoz;E. R. Savinova;G. A. Tsirlina;O. A. Petrii *Russian Journal of Electrochemistry* 2000, *36*, 741.

Shriver, D. F.;P. W. Atkins *Inorganic Chemistry*; third ed.; W.H.Freeman and Company: New York, 2000.

Smith, B. C. *Fundamentals of Fourier transform infrared spectroscopy*; CRC Press: New York, 1996.

Sparks, D. R.;M. A. Dayananda *"The behavior of transition metals in silicon during annealing transients" Defect and Diffusion Forum* 1988, *39*, 77.

Stavrevm, J. M.;D. C. W. Fischer;K. M. Drescher, N. *Thin Solid Films* 1997, *307*, 79.

Sze, S. M., Ed. *VLSI Technology*; McGraw Hill: New York, 1988.

Takahashi, K. M. *Journal of the Electrochemical Society* 2000, *147*, 1414.

Takasa, H. *Microelectronic Engineering* 2001, *59*, 237.

Usuda, K.;K. Yamada *Applied Surface Science* 1999, *143*, 16.

Venables, J. A.;D. J. Smith;J. M. Cowley *Surface Science* 1987, *181*, 235.

Verhaverbeke, S.;R. Messoussi;H. Morinaga;T. Ohmi In *Ultraclean Semiconductor Processing Technology and Surface Chemical Cleaning and Passivation*; M. Liehr,

M. Heyns, M. Hirose,H. Parks, Eds.; Materials Research Society: Pittsburgh, 1995; Vol. 386, p 3.

Verhaverbeke, S.;R. Messoussi;H. Morinaga;T. Ohmi (1995). Recent Advances in Wet Processing Technology and Science. Materials Research Society: Symposium Proceedings, Materials Research Society.

Vickerman, J. C., Ed. *Surface Analysis - The Principal Techniques*; John Wiley & Sons: New York, 1997.

Wagner, C. D.;W. M. Riggs;L. E. Davis;J. F. Moulder *Handbook of X-ray Photoelectron Spectroscopy*; Physical Electronics: Eden Prarie, MN, 1995.

Watanabe, S.;M. Shigeno;N. Noriaki;T. Ito *Japanese Journal of Applied Physics* 1991, *30*, 3575.

Watanabe, S.;Y. Sugita *Surface Science* 1995, *327*, 1.

Wu, P. K.;G. R. Yang;T. M. Lu *Appl. Phys. Lett.* 1994, *65*, 508.

Xhie, J.;K. Sattler;U. Muller;N. Venkateswaran;J. Raina *Journal of Vaccuum Science and Technology, B* 1991, *9*, 833.

Xu, J.;W. Huang;R. L. McCreery *Journal of Electroanalytical Chemistry* 1996, *410*, 235.

Yang, S.-K.;S. Peter;C. G. Takoudis *Journal of Applied Physics* 1994, *76*, 4107.